ANALYSIS AND DESIGN OF ANTENNA AND PASSIVE MICROWAVE CIRCUIT ELEMENTS ON FLEXIBLE SUBSTRATE

ESNEK ALTTAŞ ÜZERİNE ANTEN VE PASİF MİKRODALGA DEVRE ELEMANLARI ANALİZİ VE TASARIMI

NOAMAN NASEER

PROF. DR BiRSEN SAKA

Supervisor

Submitted to

Graduate School of Science and Engineering of Hacettepe University

as a Partial Fulfillment to the Requirements

for the Award of the Degree of Doctor of Philosophy

in Electrical and Electronics Engineering

2022

ABSTRACT

ANALYSIS AND DESIGN OF ANTENNA AND PASSIVE MICROWAVE CIRCUIT ELEMENT ON FLEXIBLE SUBSTRATE

Noaman NASEER

This dissertation is about the design and analysis of passive microwave circuits on flexible substrates. The work is divided into three parts material characterization, design, and fabrication. Two types of textile samples cotton, jeans, and two types of synthesized mold silicone PDMS, and AK-Sil1310T are selected for analysis. The dielectric properties of cotton, jeans, PDMS, and AK-Sil1310T are determined using a waveguide and modified ring resonator for a 1-12 GHz frequency band. The waveguide setup consists of X-band (8.2-12.5 GHz) rectangular waveguides, a vector network analyzer, the coaxial cables, and the N-type coaxial to waveguide converters. The scattering parameters of test materials are measured through a waveguide setup whereas the Nicolson-Ross-Wier algorithm is used to extract the dielectric properties from measured scattering parameters. To determine material properties using the resonant method two microwave structures microstrip transmission line a and microstrip ring resonator are

realized. The dielectric properties obtained through both methods are significantly matched.

The different conductive materials such as conductive ink, conductive textile, and conductive yarn are investigated to compare their performance when used in the fabrication of circuit elements on textiles. The fabrication techniques including screen printing, Physical Vapor deposition, sticking, and stitching are also examined.

In the design phase, an X-band reflectarray with a rectangular patch element is simulated using Ansys HFSS electromagnetic simulation software. The phase range corresponding to patch dimension for single-layer and 2-layer unit cells is obtained. The single-layer unit cell has a phase range of around 330º but has steeper phase variation whereas the 2-layer unit cell has more the 300º has gradual phase variation Based on fabrication error tolerance and bandwidth criteria 2-layer unit cell is used to design complete reflectarray. The simulations of reflectarray for center feed configuration having 15x15 elements and offset feed configuration having 17x17 elements are carried out by using the ANSYS HFSS simulation tool. The radiation patterns, gains, and efficiencies are calculated for both antennas. The gain for center feed configuration is around 21 dB and the estimated efficiency is around 43%, similarly the gain for offset feed configuration is around 23 dB while the estimated efficiency is around 45%.

Both designs are fabricated through computerized embroidery technique using silver-coated conductive thread while the ground plane is made using conductive textile. The fabricated design was tested with the help of a wooden structure built in the lab and compared with simulations.

Keywords: Flexible substrate, Textile substrate, Dielectric characterization, Waveguide method, Modified ring resonator, Reflectarray, Computerized Embroidery

ÖZET

ESNEK ALTTAŞ ÜZERİNE ANTEN VE PASİF MİKRODALGA DEVRE ELEMANLARI ANALİZİ VE TASARIMI

Noaman NASEER

Bu tez, esnek alt taşlar üzerine pasif mikrodalga devrelerinin tasarımı ve analizi ile ilgilidir. Tezin içeriği, malzeme karakterizasyonu, tasarım ve üretim olmak üzere üç bölüme ayrılmıştır. Analiz için iki tekstil örneği (pamuk ve kot kumaşı) ile iki farklı kalıp silikon (PDMS ve AK-Sil1310T) seçilmiştir. Pamuk, kot kumaşı, PDMS ve AK-Sil1310T'nin dielektrik özellikleri, 1-12 GHz frekans bandında dalga kılavuzu ve halka rezonatörü kullanılarak belirlenmiştir. Dalga kılavuzu ölçme düzeneği, X-bandı (8.2-12.5 GHz) dikdörtgen dalga kılavuzları, vektör ağ analizörü, eş eksenli kablolar ve N-tipi eş eksenli konnektörden dalga kılavuzuna dönüştürücülerden oluşur. Ölçülecek malzemelerinin saçılma parametreleri, dalga kılavuzu düzeneği ile ölçülmüş, Nicolson-Ross-Wier algoritması kullanılarak ölçülen saçılma parametrelerinden dielektrik özellikleri hesaplanmıştır. Rezonans yöntemini kullanarak malzeme özelliklerini belirlemek için ise mikroşerit iletim hattı ve mikroşerit halka rezonatörü üretilmiştir. Her iki yöntemle elde edilen dielektrik özellikler önemli ölçüde uyumludur.

İletken mürekkep, iletken tekstil ve iletken iplik gibi farklı iletken malzemeler, tekstil üzerine devre elemanı üretiminde kullanıldıklarındaki performanslarını karşılaştırmak için incelendi. Ayrıca serigrafi, nano biriktirme, yapıştırma ve dikiş gibi üretim teknikleri de incelendi.

Tasarım aşamasında, Ansys HFSS elektromanyetik benzetim yazılımı kullanılmış ve X-bandında yansıtıcı dizi anten tasarımı için dikdörtgen yama birim elemanı analiz edilmiştir. Bu amaçla, tek ve iki katmanlı birim hücreler için yama boyutuna karşılık gelen faz eğrileri elde edilmiştir. Tek katmanlı birim hücre ile 330° civarında, iki katmanlı birim hücre için ise 300° faz değişimi elde edilmiştir. Üretim hata toleransı daha iyi olduğu için, daha az faz değişimi elde edilmesine rağmen iki katmanlı birim hücre komple tasarım için kullanılmıştır. 15x15 elemanlı odaktan beslemeli ve 17x17 elemanlı kayık beslemeli yansıtıcı anten tasarımları ANSYS HFSS benzetim programı aracıyla gerçekleştirilmiştir. Antenlerin, ışıma örüntüsü, kazanç ve verimleri hesaplanmıştır. Odaktan besleme için kazanç yaklaşık 21 dB'dir ve tahmini verimlilik yaklaşık %43'dir, benzer şekilde kayık besleme konfigürasyonu kazancı 23 dB civarındadır, tahmin edilen verimlilik ise yaklaşık %45'tir.

Her iki tasarım da gümüş kaplı iletken iplik kullanılarak bilgisayarlı nakış tekniği ile üretilmiş, toprak düzlemi iletken tekstil kullanılarak yapılmıştır. Üretilen tasarım, geçici bir kurulum yardımıyla test edildi ve simülasyonlarla karşılaştırılmıştır.

Anahtar Kelimeler: Esnek alttaş, Tekstil alttaş, Dielektrik karakterizasyon, Dalga kılavuzu yöntemi, Halka rezonatörü, Yansıtıcı dizi, Bilgisayarlı nakış

ACKNOWLEDGMENT

NOAMAN NASEER

May 2022, Ankara

TABLE OF CONTENTS

LIST OF FIGURES

LIST OF TABLES

SYMBOLS AND ABBREVIATION

SYMBOLS

D	Electric Displacement Vector.
B	Magnetic Flux Density.
H	Magnetic Field Intensity.
E	Electric Field Intensity.
J	Current Density.
ρ	Charge Density.
σ	Conductivity
ε	Complex Permittivity
μ	Complex Permeability
η	Characteristic Impedance
γ	Propagation Constant
$p_{i,N}$	Schneider Filling Factor
q_i	Wheeler Filling Factor
Γ	Reflection Coefficient
T	Transmission Coefficient
φ_{dl}	Delay Line Phase Shift
ϕ_{spd}	Spatial Phase Shift
ϕ_{pp}	Progressive Phase shift
η_a	Aperture Efficiency
η_i	Illumination Efficiency
η_s	Spillover Efficiency
F	Vertical distance of feed antenna from the array

D	Far Field Distance

ABBREVIATION

RF	Radio Frequency
INDI	Integrated Nano System development Institute
NIAC	NASA Innovative Advance Concept
RFID	Radio Frequency Identification
WSN	Wireless Sensor Network
OLED	Organic Light Emitting Diode
IoT	Internet of Things
TE	Transverse Electric
TM	Transverse Magnetic
TEM	Transverse Electromagnetic
OSLT	Open Short Load Through
TRL	Through Reflect Line
SOO	Short Offset Offset
NRW	Nicolson Ross Weir
VNA	Vector Network Analyzer
MUT	Material Under Test
BW	Bandwidth
FSS	Frequency Selective Surface
PVD	Physical Vapor Deposition
PEC	Perfect Electric Conductor
SPD	Spatial Phase Distribution
PP	Progressive Phase

1. INTRODUCTION

1.1 Problem statement

The continuous evolution in flexible materials research and integration of passive Radio Frequency (RF) and microwave components on these materials using printing technologies have opened lots of novel applications in the biomedical, automotive industry, and human-machine interfaces. The designing of passive RF components such as antennas, filters, splitter, etc. and their fabrication, on flexible substrates is a complex process. This dissertation aims to focus on the development and optimization of microwave passive circuits on flexible substrates that can offer added advantages such as low cost, high conformability, and high scalability in addition to seamless heterogeneous integration. Designing Microwave/ RF circuits on flexible substrates is a complex task and need extensive research and deep knowledge of material characterization and electromagnetic simulation of microwave circuits as well as the fabrication technologies.

The continuous demands for lightweight, portable and wearable electronic devices encourage researchers to explore flexible RF components. Due to being an integral part of wireless devices, flexible antennas and RF circuit components are much more attractive than ever. According to GlobeNewswire, the market share of flexible electronics is expected to reach $61 billion by 2030 which is shown through the bar chart in Figure 1.1 [1].

This bar chart shows the estimated market revenue of flexible electronics, the majority of which is consisting of OLED (Organic Light Emitting Diode) display but other components also show great growth potential. Due to the recent advancement in technology such as the internet of things (IoT) and the smart city concept, the demand for flexible electronics increases almost in every field like consumable electronics including, healthcare and monitoring, space and satellite communication, defense, and sportswear.
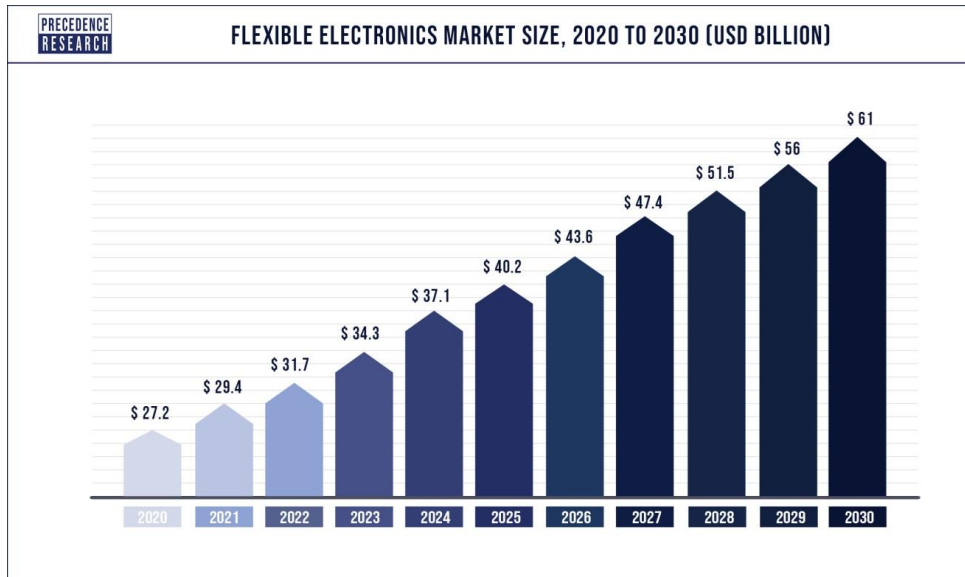
Figure 1.1. Flexible electronics market share forecast credited GlobeNewswire [1].

1.2 Literature review

Limited research has been done on flexible electronics and flexible antennas however, this research trend is exponentially growing owing to novel simulation tools and advanced fabrication techniques. The choice of substrate is critically important, many researchers explore different substrates in their research work, which include textile [2], paper [3-4], fluid based [5], and synthesized materials [6-9]. Graphene based passive components for low cost wearable electronics are discussed in [6]. The author investigated Graphene based conducting ink to design a feeding transmission line for antenna arrays [10]. The paper based passive components for RFID and WSN applications are explored in [3], while inkjet printed microwave circuit on flexible substrates using heterophane graphene-based ink is described in [7]. Zhenqiang Ma et al presented a review on flexible active and passive microwave components. They discussed different flexible substrates such as silicon, compound semiconductors, and 2D materials like $MoS2$ and Graphene in their paper [11]. Similarly, Weinan Zhu and his colleagues gave a review about advancements in 2D flexible substrates. In that research, they explored 2D atomic crystal-based substrate for microwave application and suggested that 2D atomic Van der Waals crystals could be a potential candidate for such applications [12]. Kapton, which has very high-temperature stability (400°), and very good soldering tolerance is another very promising option to use as a substrate to design flexible microwave circuits [8]. In [13] authors develop a conformal compact medical antenna and present a very interesting application of

ingestible medical wireless capsule. Researchers at Integrated Nano systems Development Institute (INDI) developed a flexible antenna prototype for skin contact based applications. The designed antenna was tested for microwave breast imaging to detect breast cancer [14]. Besides these, a very innovative idea of printable spacecraft is discussed in the report about early stage innovation published by NASA Innovative Advanced Concepts (NIAC) research team [15].

Printing technology also plays a vital role in flexible electronics. In [16] and [17] researchers discuss different fabrication techniques for flexible microwave electronics. Screen Printing is the simplest and most cost-effective technique. In this technique, the pattern is printed on the substrate by squeezing the blade with force and ejecting ink on the exposed area of substrate by force as a result the desired pattern is formed on the substrate [18]. Different RFIDs and flexible antennas are successfully realized by using this technique [19, 20].

Photolithography and chemical etching are widely used fabrication techniques for PCB designing but due to its low throughput and treatments of the substrate with hazardous chemicals, this technique is less attractive for flexible electronics however, the photo imageable inks still offer one of the finest design resolutions. The most common technique, which provides excellent throughput and acceptable resolution, is Inkjet printing. Many researchers use this fabrication technique in their research work [3,7, 21]. A pattern switchable antenna using inkjet printing for sensing application and 2D phase array antenna are discussed by the author in [21] and [22] respectively.

The fabrication of microwave passive components on flexible material and integration with other components needs extensive research and exploration. In this study the two-textile materials cotton and jeans while two mold silicone materials PDMS and AK-Sil T1310 are investigated for electromagnetic properties. Due to a lack of fabrication resources for mold silicone materials, only textile material is shortlisted for fabrication. Different fabrication techniques which include screen printing, Physical Vapor Deposition, stitching/sewing, and sticking are investigated. In the literature review, it has been observed that quite a significate work is available on wearable microstrip patch antenna however very few researches are present on other applications. In this thesis, we study the reflectarray antenna design using a textile substrate. In general, designing a reflectarray is a complicated task, and designing on a textile substrate increases its

3

complexity further. This thesis work explains the design of reflectarray antenna on jeans textile

1.3   Thesis Structure

Designing a typical microwave or RF circuit on a flexible substrate includes various design steps like material selection and characterization, designing and fabrication of components, and in the end conducting test measurements, these steps are shown in Figure 1.3 to elaborate the design cycle.
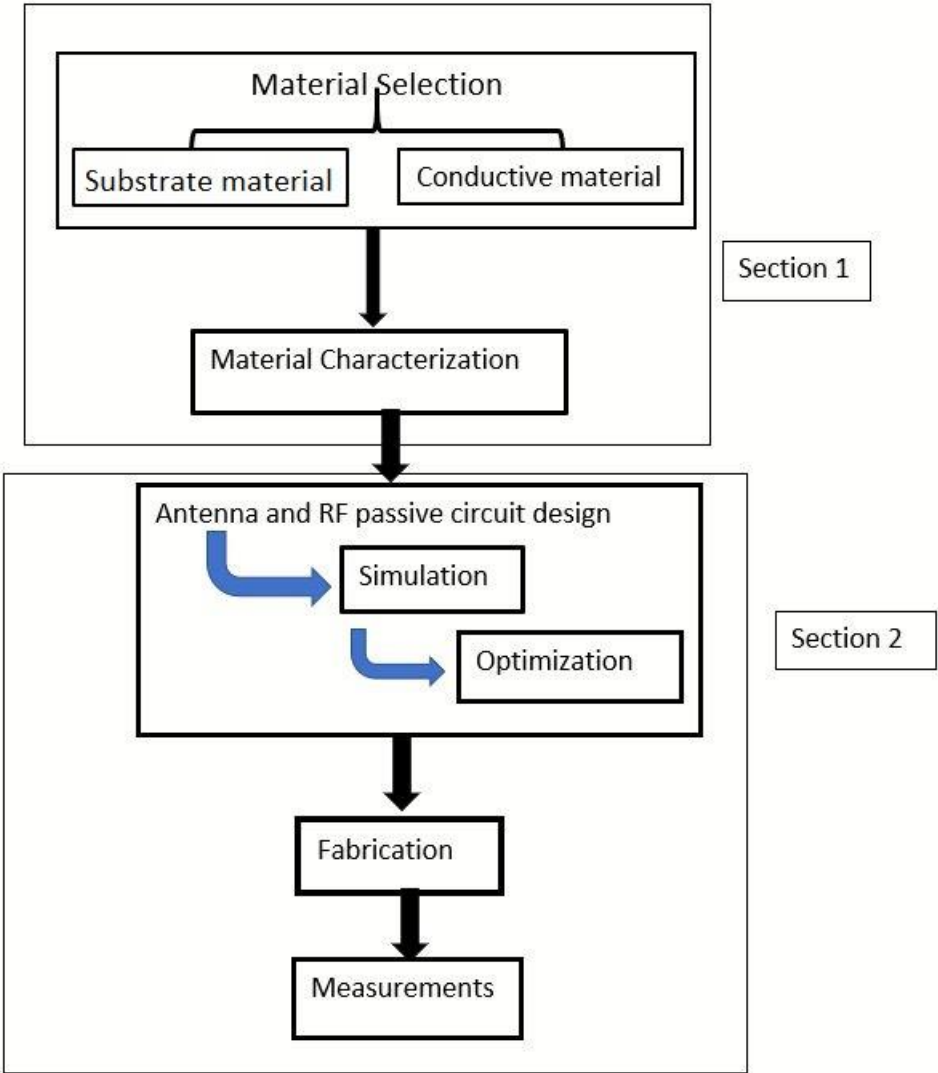
Figure 1.2. General design procedure [23].

This thesis work comprehensively explains all the designing steps shown in Figure 1.3 and is divided into two sections. The first section includes chapters 2, and 3 which are about the material selection and characterization. Chapter 2 describes different types of

materials based on micro and macroscopic properties. The different electromagnetic characterization techniques are also presented. In chapter 3, methods implemented for electromagnetic characterization of textile/mold silicone and measured results are presented. Moreover, different viable fabrication techniques for the textile substrate are also investigated. The second section includes chapters 4 to chapter 7 and is related to design simulation, fabrication, and testing of the antenna and passive circuit element. In chapter 4 a brief literature review on the reflectarray antenna is presented. Chapter 5 detailed the element and system level design simulations, chapter 6 is about fabrication and measurements while the last chapter presents a comprehensive conclusion on the complete research.

2. Electromagnetic Material Characterization

2.1. Material Types

The materials and their properties are the topics of research for decades. The interaction of electromagnetic waves with the materials leads to the significance of investigating the electromagnetic properties of materials. Both microscopic and macroscopic properties of materials can be determined through electromagnetic or microwave measurement techniques. These techniques are applicable in RF and microwave circuit designing as well as many other fields. The processing speed of computational devices is increasing continuously. These electronic devices require a clock operating at the gigahertz frequency range. The use of microwave frequencies for communication purposes and other civil and military applications are also increased many times. Design of these devices requires accurate information about the electromagnetic properties of materials. Moreover, the development of new electromagnetic material emphasizes the importance of electromagnetic characterization.

The microscopic molecules are combined to form a material. On the microscopic level, two critical phenomena are observed in the material. The one is the energy bandgap. Based on this phenomenon, materials are categorized into conductors, semiconductors, and insulators. The other is the spinning of the electron around the nucleus. The spin produces a magnetic momentum in the material. Based on this magnetic momentum, the materials are classified into diamagnetic, paramagnetic, and ferromagnetic materials.

Conductors

The materials which conduct electricity are termed, conductors. Generally, their conductivity is in the order of 10^4 to $10^8 (\Omega m)^{-1}$. The conductors are further classified into perfect conductors and superconductors. The perfect conductors are supposed to have infinite conductivity for all frequencies, whereas superconductors have infinite conductivity for the Dc electric field while having complex conductivity for higher frequencies.

Insulators

The materials which are non-conducting, or have very high electric resistance are considered as an insulator. They have very low conductivity usually ranging from 10^{-12} to $10^{-20} (\Omega m)^{-1}$.

Semiconductors

The material that has conductivity value between conductors and insulators is termed as a semiconductor. Their conductivity ranges from 10^{-7} to 10^4 $(\Omega m)^{-1}$.

Magnetic Materials

The material that responds to external magnetic fields is considered as magnetic material. Magnetic materials based on their permeability values are divided into four groups. The materials having permeability $\mu < \mu_0$ are considered as diamagnetic. Material having $\mu \geq \mu_0$ is paramagnetic, whereas ferromagnetic and ferrimagnetic materials have very high permeability values.

Dielectric Materials

The dielectric material is a type of insulator, which is polarized under the effect of the external field. In insulators, the electrons are tightly bounded, when these materials are exposed to an external electric field the bounded electron slightly shifts themselves from their equilibrium position resulting in dielectric polarization. When this external field is removed the shifted electrons go back to an equilibrium position after some time known as relaxation time. The physical phenomena that affect the material's permittivity along the frequency are conduction, dipole relaxation, electronic and atomic polarization. Figure 2.1 gives an overview of the variation of permittivity as a function of frequency for a theoretical dielectric material.
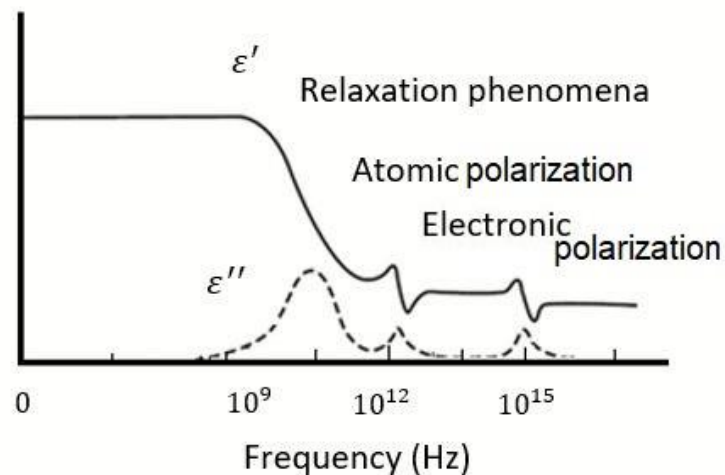
Figure 2.1. Variation of permittivity of a hypothetical dielectric material vs frequency [24].

It can be observed from Figure 2.1 that the dielectric constant remains unchanged up to 10 GHz. Then from 10 GHz to 10 THz, it starts decreasing. This variation at microwave frequencies is due to dipole relaxation. Some sharp peaks are also observed in the infrared and visible region due to atomic and electronic polarization.

2.2. Electromagnetic Wave Interaction with Materials

Every material has a unique response towards external electromagnetic waves. This electromagnetic interaction with material is fully described by Maxwell's equations [25 45]. Assuming an $e^{j\omega t}$ time dependence and for linear media (permittivity and permeability are not depending on electric field intensity and magnetic field intensity), the Maxwell's equations can be written in phasor form as

$$\nabla \cdot \boldsymbol{D} = \rho \tag{2.1}$$

$$\nabla \cdot \boldsymbol{B} = 0 \tag{2.2}$$

$$\nabla \times \boldsymbol{H} = j\omega\varepsilon\boldsymbol{E} + \boldsymbol{J} \tag{2.3}$$

$$\nabla \times \boldsymbol{E} = -j\omega\mu\boldsymbol{H} \tag{2.4}$$

The constitutive equations are

$$\boldsymbol{D} = \varepsilon\boldsymbol{E} \tag{2.5}$$

$$\boldsymbol{B} = \mu\boldsymbol{H} \tag{2.6}$$

where

$\boldsymbol{D}$ is the electric displacement vector.

$\boldsymbol{B}$ is the magnetic flux density vector.

$\boldsymbol{H}$ is the magnetic field intensity vector.

$\boldsymbol{E}$ is the electric field intensity vector.

$\boldsymbol{J} = \sigma\boldsymbol{E}$ is the current density vector and σ is the conductivity of the medium.

ε is the permittivity of the medium.

μ is the permeability of medium.

ρ is the charge density.

In a linear medium, the permittivity and permeability of medium can be written as

$$\varepsilon = \varepsilon' - j\varepsilon'' \qquad\qquad (2.7)$$

$$\mu = \mu' - j\mu'' \qquad\qquad (2.8)$$

The real part of permittivity ε' represent stored electric energy, the imaginary part ε'' indicates dissipated electric energy while the real part μ' and imaginary part μ'' of permeability indicates stored and dissipated magnetic energy respectively. The material dielectric properties usually expressed in terms of relative permittivity ε_r and permeability μ_r.

$$\varepsilon_r = \frac{\varepsilon'}{\varepsilon_o} - j\frac{\varepsilon''}{\varepsilon_0} \qquad\qquad (2.9)$$

$$\mu_r = \frac{\mu'}{\mu_o} - j\frac{\mu''}{\mu_0} \qquad\qquad (2.10)$$

2.3. Material Characterization Techniques

The performance of RF or microwave circuits is mainly subjected to the dielectric properties of the substrate. For an efficient design, it is necessary to determine these properties very accurately. There are many methods available to determine the dielectric properties of materials. The main factors affecting the choice of an implemented technique are the frequency range, measurement accuracy, temperature, form, and size of the sample. Two critical electromagnetic phenomena occur when an electromagnetic wave interacts with a material, namely resonance, and propagation. Based on these phenomena the electromagnetic characterization techniques are categorized into resonant and non-resonant techniques. The resonant method provides information about the dielectric properties of the material for a single frequency or the discrete points on a range of frequencies. In contrast, the non-resonant method helps to determine dielectric properties over a wideband frequency. Different techniques are compared in [26] and [27] to highlight their advantages and disadvantages. The author presented a comprehensive review of the transition from low-frequency dielectric characterization techniques to broadband spectroscopy and high-frequency imaging [28].

2.3.1. Non-resonant Method

The electromagnetic properties of test material estimated through the non-resonant method are mainly calculated from the change in wave impedance and propagation velocity of a wave propagating from one medium to another. When an electromagnetic

wave incident on the interface of two different materials, some incident waves are reflected back to the first medium while some propagate through the second medium. This partial reflection and transmission are then used to determine the dielectric properties of the material. The figure given below shows the transmission and reflection from the interface between two materials.
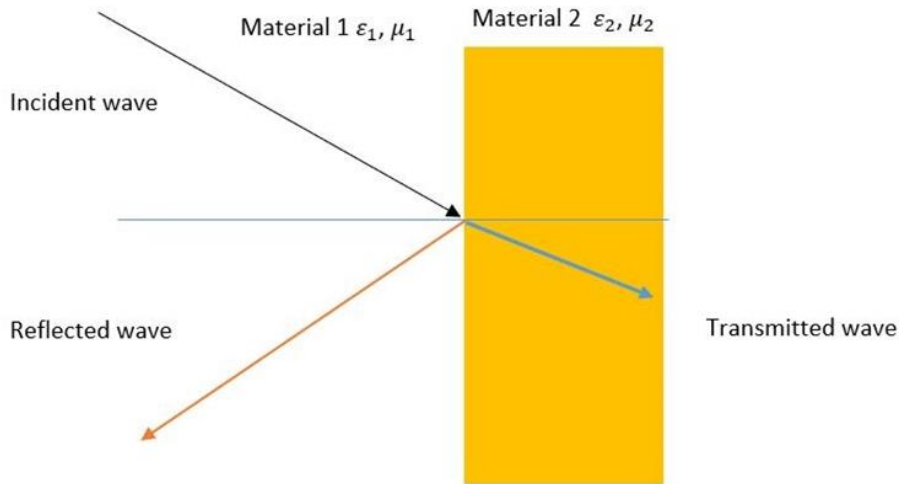
Figure 2.2. Transmission and reflection of electromagnetic waves from the interface of two materials having different dielectric properties.

The non-resonant method is based on the transmission and reflection of electromagnetic waves from the material under investigation and can be classified into the reflection-only and the transmission/reflection method. In the reflection-only method, the dielectric properties of the material are determined only from reflected waves [29-31]. On the other hand, the transmission/reflection method utilizes both the transmitted and reflected wave [32-33]. Based on the measuring setup, the non-resonant method can be further classified into the free space method and transmission line method [24], [32-33].

All types of transmission lines, such as coaxial, metallic waveguides, dielectric waveguides, and planar transmission lines, can be used in the non-resonant method.

Free Space Method

In this method, the electromagnetic wave emitting from radiating structures like antenna traveling through air (free space) incidents on test materials, then the dielectric properties are obtained from the transmitted and reflected waves. The measurement setup is shown in the figure below.
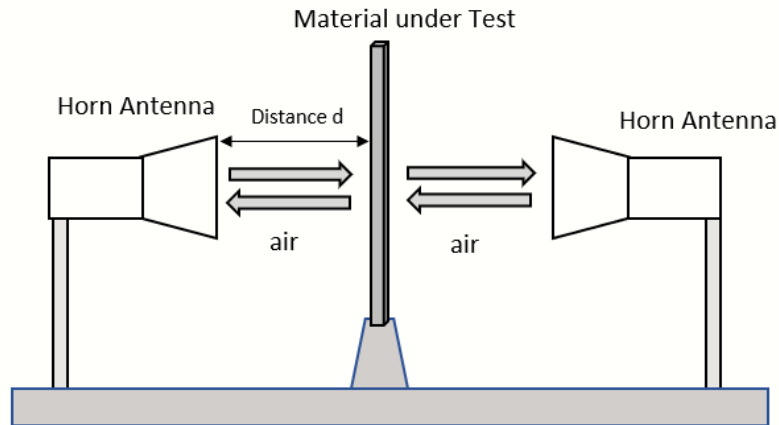
Figure 2.3. Free space method.

For accurate dielectric characterization of material with this method requires to fulfill some setup requirements. The prime conditions are far-field distance, sample size, and measurement environment.

Far-field Distance Requirement

In the free space method, the incident electromagnetic wave must be a plane wave. The generation of plane wave requires that the distance d between transmitting antenna and test sample must be equal to or higher than the far-field distance criterion.

$$d = \frac{2D^2}{\lambda} \qquad (2.11)$$

where D is the largest dimension of the antenna aperture, whereas λ is the operating frequency wavelength.

Sample Size

Sample size plays a vital role in measurement. If the sample size is smaller than the wavelength of the incident wave at the operating frequency then it will be considered as a particle that results in inaccurate measurements. Moreover, scattering from the edge or boundary is also a vital source of error in the free space method. For precise and correct measurements, the sample size must be twice larger than the wavelength of the incident wave.

Measurement Environment

In the free space method, the measurement environment is essential for an accurate result. Different environmental conditions can drastically change the outcome. For error free

measurements, the free space method must be conducted in an anechoic chamber. Alternatively, time-domain gating is also a way to mitigate environment reflection and multireflection.

Transmission Line Method

The transmission line method is based on the measurement of transmission and reflection from the material placed inside a transmission line.

In principle, two transmission lines structures are used frequently; one consists of a single hollow conductor, for example, a rectangular, circular, and ridged waveguide. These transmission lines support TE and TM propagation modes only.
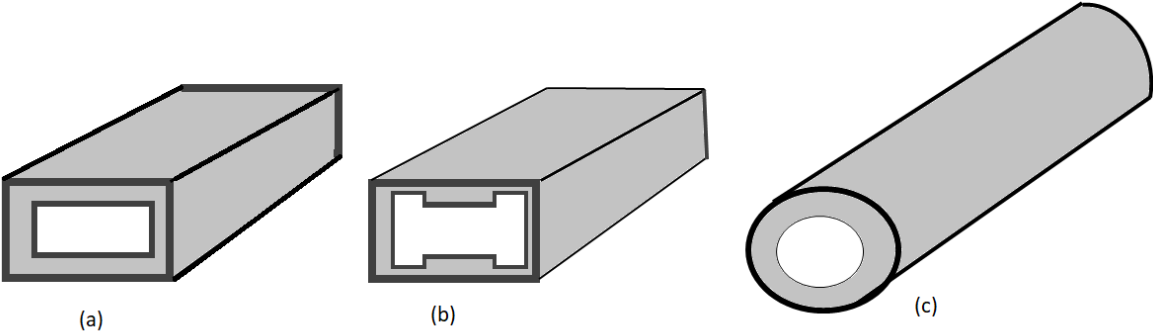
Figure 2.4. Hollow transmission lines. (a) Rectangular waveguide, (b) circular waveguide, (c) ridged waveguide.

The other structure is a transmission line with more than one conductor; common examples are parallel lines, parallel plates, and coaxial transmission line. The propagation mode in these transmission lines is TEM mode.
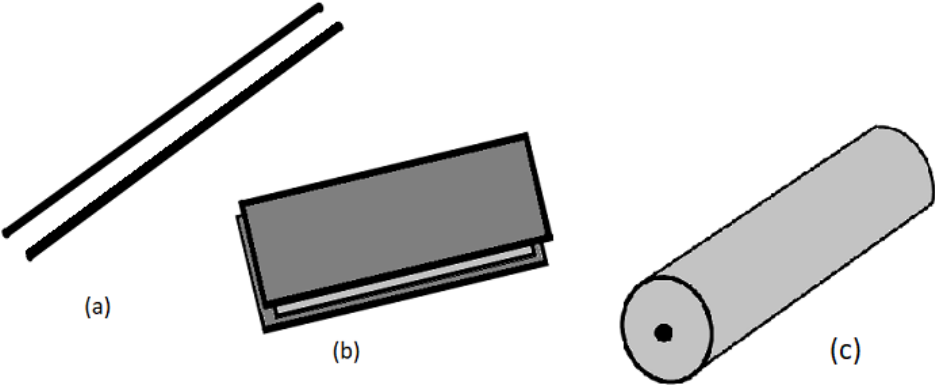
Figure 2.5. A transmission line with more than one conductor. (a) Parallel line, (b) parallel plate (c) coaxial transmission line.

2.3.2. Reflection only Method

In the reflection-only method, the electromagnetic properties are deduced only from the reflection coefficient. Mainly two types of standards, open, and short circuit reflection are used.

Open Circuit

In open circuit reflection, the sample under test is not backed with other conducting, dielectric, or absorbing material except air. Better measurement with this method required a much thicker sample so that the reflected wave should reflect with a proper reflection phase.
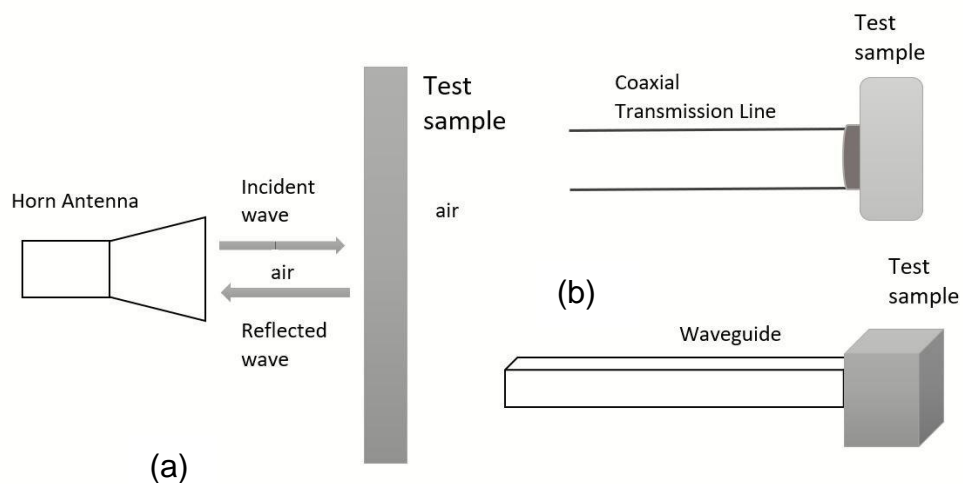
Figure 2.6. (a) Free Space open circuit reflection-only method. (b) Transmission line open circuit reflection-only method.

Short Circuit

In this method, the sample under test is backed with a perfect electric conductor for short-circuiting. Mostly this method is suitable to measure the dielectric properties of thin materials and thin films.
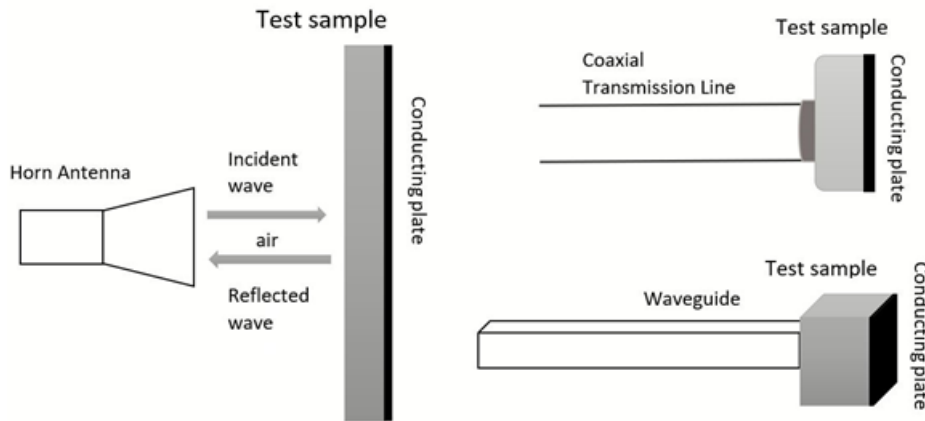
Figure 2.7. Free Space Short circuit reflection only method.

2.3.3. Transmission and Reflection Method

The transmission and reflection method consists of two antennas/ transmission lines. The dielectric properties are determined by using both transmission and reflection coefficients. In this technique, the sample size needs proper consideration to avoid edge reflections. Figure 2.8 shows the two most used setup configurations for the free-space method, while Figure 2.9 represents two transmission line setups.
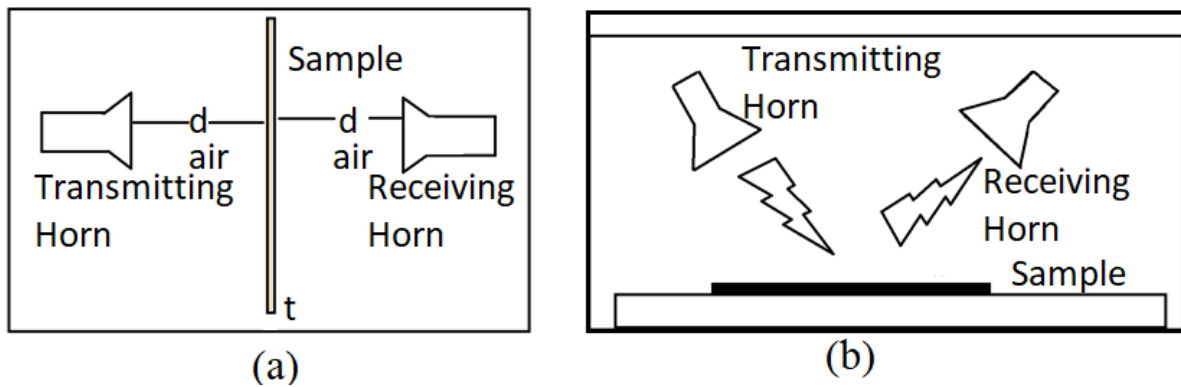
Figure 2.8. Free space standard transmission and reflection method (a) normal incidence (b) oblique incidence.
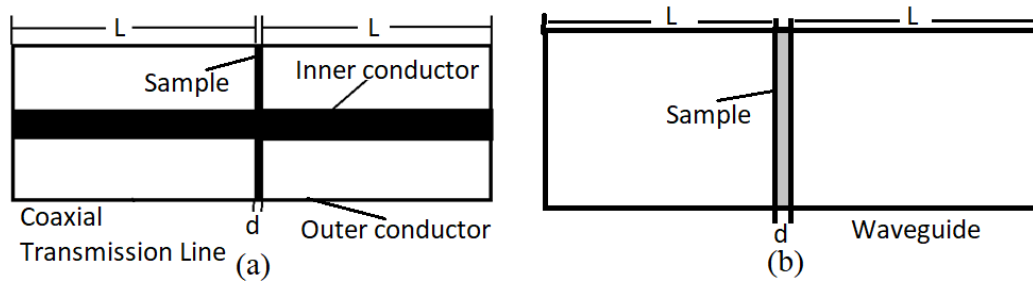
Figure 2.9. Transmission line, transmission, and reflection method (a) coaxial transmission line (b) Waveguide transmission line.

2.4. Resonant method

The method discussed above was non-resonant. In which the dielectric properties of a material are determined by using reflection and transmission of the electromagnetic wave at the interface of two different mediums. The non-resonant method is more suitable for analyzing dielectric properties on a wide frequency band. In comparison, the resonant method is more convenient when accurate information about electromagnetic properties is required on a specific frequency. Accuracy is the main advantage of this technique.

In the resonant method, the dielectric properties of the materials are determined in the resonance and quality factor of a resonator for specific dimensions. The material under test behaves as a resonant circuit or part of the resonant circuit. A resonator has certain electromagnetic boundary conditions when the test material is introduced to it, its boundary conditions are changed which ultimately results in a change of the resonance frequency and quality factor. From the change in resonance frequency and quality factor, the permittivity and permeability of a material are determined. The cavity resonator, dielectric resonator, and microstrip resonator are the most used techniques for this method. The cavity resonator is the most accurate method but it characterizes material only on a single frequency. The cavity of the resonator is filled by material and then a shift in resonance frequency with and without material is used to measure dielectric properties [34]. Simple, cost-effective, and easily implemented techniques based on different types of microstrip open resonator structures, namely patch antenna, transmission line, and available ring resonator, are presented in [35], [36], and [37].

2.4.1. Dielectric Resonator

The simplest resonator setup for electromagnetic characterization is formed by placing cylindrical-shaped dielectric material between two conductive plates. The dielectric

properties are determined through resonance frequency and Q-factor. The measurement setup is shown in the figure given below. This method is most suitable to characterize material having a high dielectric constant [38-39] or an anisotropic material [40].
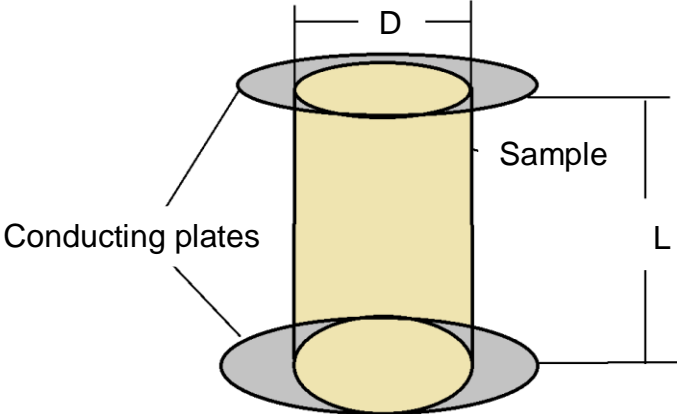
Figure 2.10. Dielectric cylinder resonator.

2.4.2. Cavity Resonator

The enclosed metallic cavities loaded with a dielectric material is one of the most accurate dielectric characterization techniques. Every cavity has a particular resonance frequency based on its dimensions. When the cavity is loaded with dielectric material its resonance frequency and quality factor got changed. The dielectric properties are then determined numerically from the shift in resonance and quality factor due to material.
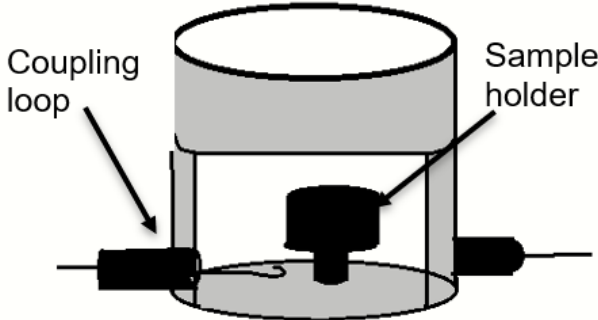
Figure 2.11. 3D view of the cavity resonator.

2.4.3. Split-Resonator method

The split resonator method consists of a cylindrical resonator split into two halves. The test sample is placed in a gap between two halves having a maximum electric field. This method is mainly used to measure the dielectric properties of sheet and planer dielectric

materials. The dielectric properties are determined from the shift in resonance frequency of empty fixtures due to material. The experimental setup is given below.
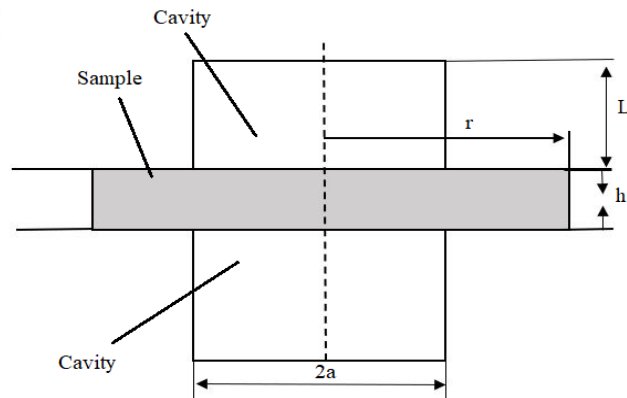
Figure 2.12. Split resonator method.

2.4.4. Open Resonator

At high frequencies, the size of the cavity resonator becomes small, leading to difficulties in preparing the sample for testing. The cavity size and sample size are directly proportional, making cavity resonators almost impossible to use at ultrahigh frequencies. Moreover, the resonator's quality factor also decreases with a wavelength, which leads to inaccurate loss tangent measurement. These difficulties are solved by using an open resonator [41]. The measurement setup shown in the figure below consists of a spherical conductor having an opening, and a planer conductor. A Gaussian beam is used for excitation of the cavity. The dielectric properties are determined by the shift in resonance frequency and Q-factor of the loaded and unloaded cavity.
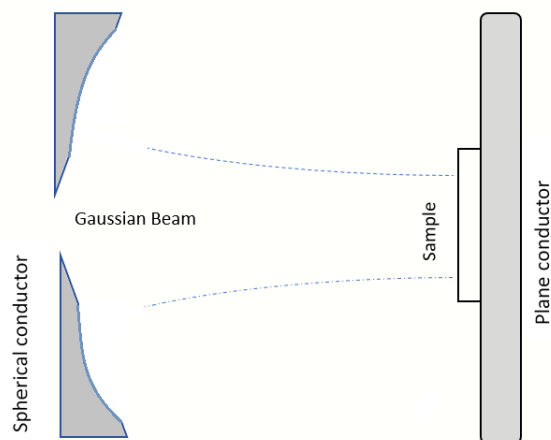
Figure 2.13. Open resonator.

17

2.4.5. Planar circuit method

In the planar method, the material under test is used as a substrate to design planar resonant circuits. The dielectric properties are determined to form resonance frequency and quality factor. The planar circuit could be a microstrip line, stripline, and microstrip patch antenna.
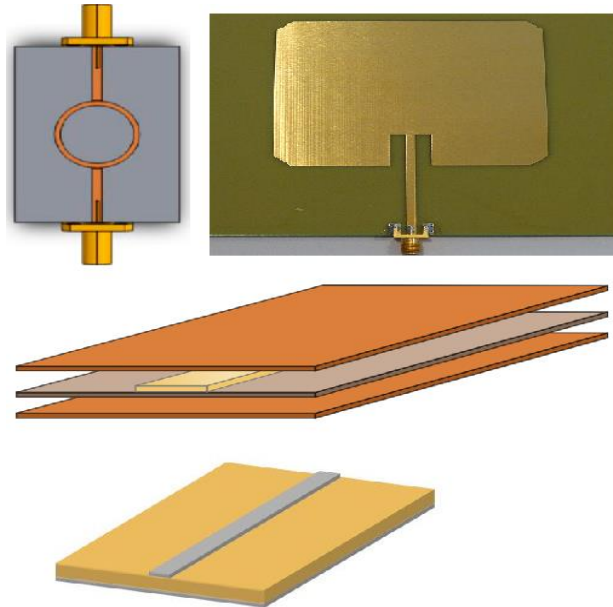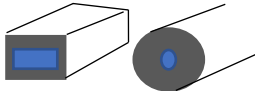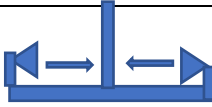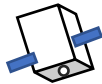
Figure 2.14. Planar resonators.

An overview of different techniques is given in Table 2.1.

Table 2.1. Different techniques for electromagnetic characterization [42]

Coaxial probe ε_r		Broadband, convenient, non-destructive, best for lossy MUTs, Liquids, or semi-solids
Transmission line ε_r and μ_r		Broadband, best for lossy MUTs, machinable solids
Free space ε_r and μ_r		Non-contacting Best for high temperature; large, flat sample
Resonant cavity ε_r and μ_r		Accurate Best for low loss MUTs, small samples
Parallel plate ε_r		Accurate Best for low frequencies; thin flat sheets

In this thesis, both the resonant and non-resonant techniques are used to investigate the dielectric properties of the flexible materials under test. In the resonant technique, the microstrip modified ring resonator and microstrip line are explored, while in the non-resonant technique, the waveguide method is implemented. The detail discussion about these methods is presented in the next chapter.

3. DIELECTRIC CHARACTERIZATION OF FLEXIBLE MATERIALS

3.1. Waveguide Method

A typical waveguide measurement system consists of a vector network analyzer, coaxial cable, coaxial to waveguide adapter, and waveguide shown in the figure given below [32], [43].
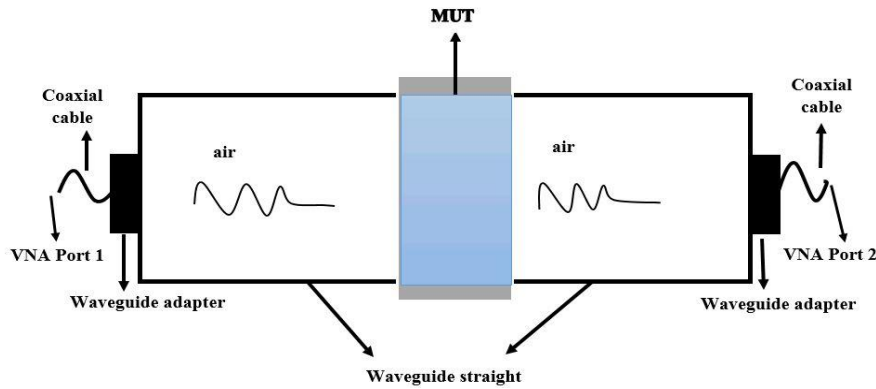
Figure 3.1. Waveguide setup.

The material whose dielectric properties need to be determined must place in between waveguides. The dielectric and magnetic properties ε_r and μ_r are deduced from the S_{11} and S_{21} parameters measured at the network analyzer's port connected to waveguide straights through coaxial cables. The dominant mode in coaxial cable is TEM, while waveguide structures can only support TE or TM modes. Moreover, waveguide structures usually have high characteristic impedance, whereas coaxial cables typically have 50 Ω. Due to this reason, impedance matching is required between coaxial cable and waveguide for the proper transition of electromagnetic signal. Coaxial to waveguide adapter/converter is used to generate the required propagation mode in a waveguide.

The TE_{10} incident wave traveling along the waveguide strikes on the material having thickness t, relative permittivity ε_r, relative permeability μ_r, with a wave impedance η_1 placed in between that waveguides. Some of the incident waves reflect back to port 1 whereas some wave transmits through the material and reaches port 2. The whole scenario is shown in the figure given below.
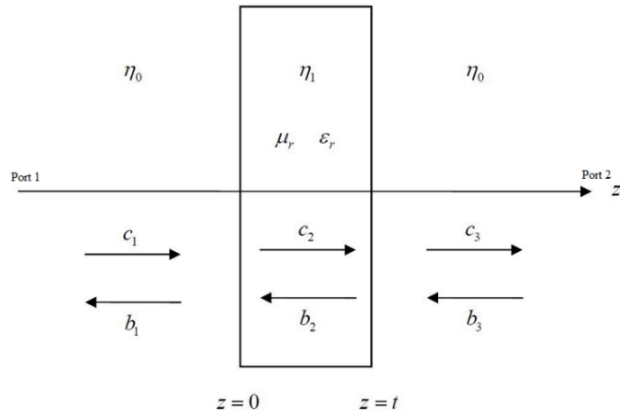
Figure 3.2. Reflection and transmission of electromagnetic waves from the material.

The dielectric properties of the material are determined from the transmitted and reflected waves detected on the network Analyzer's ports. The network analyzer must be calibrated to minimize errors before taking measurements. The Agilent 85052D calibration kit is used to calibrate Agilent E5071C VNA in our measurements

3.1.1. Network Analyzer

The Network analyzer is one of the most critical tools to analyze microwave circuits. All the material characterization techniques presented here are based on measurement through a network analyzer. The main building block of a network analyzer includes a source, signal separator, and detectors. A two-port network determines four scattering parameters S_{11}, S_{21}, S_{12} and S_{22}, from four different waves. Two of these four waves are forward traveling waves, while two of them are reverse traveling waves. Four separate detectors labeled as a_1, a_2, b_1, and b_2 are used to detect these four waves. The purpose of the signal separator is to keep these four waves separate and ensure their independent measurement by the corresponding detectors [44]. A basic network analyzer diagram is shown in Figure 3.3.
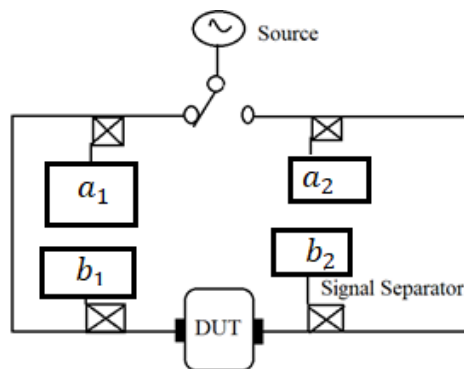
Figure 3.3. Basic network analyzer block diagram.

The relation between forwarding going $[a]$ and backward going waves $[b]$ can be described by using scattering parameters $[S]$.

$$[b] = [S][a] \qquad (3.1)$$

where

$$[a] = \begin{bmatrix} a_1 \\ a_2 \end{bmatrix} \qquad (3.2)$$

$$[b] = \begin{bmatrix} b_1 \\ b_2 \end{bmatrix} \qquad (3.3)$$

$$[S] = \begin{bmatrix} S_{11} & S_{12} \\ S_{21} & S_{22} \end{bmatrix} \qquad (3.4)$$

The scattering parameter can be determined as

$$S_{jj} = \frac{b_j}{a_j}\big|_{a_i=0} \ (i \neq j) \qquad (3.5)$$

$$S_{ij} = \frac{b_i}{a_j}\big|_{a_i=0} \ (i \neq j) \qquad (3.6)$$

The S_{jj} indicates the reflection coefficient whereas S_{ij} depicts the transmission coefficient.

The measurements through the network analyzer are also drastically affected by measurement errors, including systematic, random, and drift errors.

Systematic Errors

Systematic errors arise due to shortcomings in measuring devices. Multiple reflections from material under test (MUT), signal leakage, crosstalk, and frequency response contribute to this error. These errors are the main reasons for limiting the dynamic range of the network analyzer. Sometimes multiple reflections from test devices are not detected by a sensor, or sometimes leakage signals which are not reflected by the test device are received at reflected wave detectors. Similarly, crosstalk results due to the coupling of signals from two different ports due to poor isolation. The frequency response error is mainly caused due to path loss, and phase delay. The most systematic error doesn't vary with time and can be removed through calibration and mathematical correction.

Random Errors

Random errors are unpredictable and caused due to instrument noise, connectors, and switch repeatability. These errors can be removed by taking measurements many times and averaging the results.

Drift errors

The test environment is the main reason for drift errors. The difference between environmental conditions such as the temperature difference during system calibration and test measurements can cause errors. These errors can be removed by keeping the environmental conditions for system calibration and measurements the same.

3.1.2. Network Analyzer calibration

To remove the systematic error requires system calibration. In network analyzer calibration, known reference standards of transmission, reflection, and matched load are used to model the scattering parameters for systematic errors. Three terms of systematic errors i.e. directivity E_D, source match E_s, and reflection tracking E_{TR} are determined and represented as an error adapter. Once they are obtained, they are subsequently corrected mathematically from measured scattering parameters of the device under test.

Primarily, one-port and two-port calibration techniques are used in microwave and RF measurements.

One-port Calibration

As discussed above, the reflection-only method utilizes only one port, and the only reflection parameter is a matter of interest. The measurement methods with one port require one-port calibration. One-port calibration can significantly remove the errors due to multiple reflections, and leakage. The ideal case scenario and an error adapter are shown in Figure 3.4.
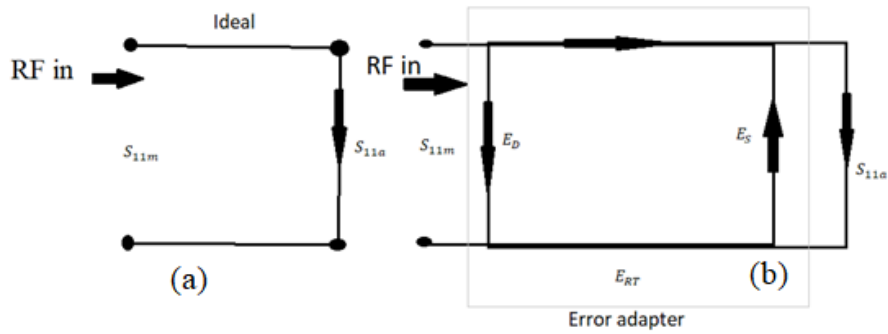
Figure 3.4. One-port calibration model. (a) Ideal case, (b) with error adapter [44].

Two-port Calibration Method

The microwave devices which utilize both ports of the network analyzer require two-port calibration. Two-port calibration removes errors from both transmission and reflection parameters measured with a network analyzer. It includes full two-port calibration, short-open-load-through calibration (SOLT), and reflect line (TRL) calibration. Both SOLT and TRL have a similar mathematical model. With two-port calibration, all the systematic errors can be removed. The full two-port calibration model has 12 terms 6 for forward and 6 for backward going waves, known as 12-term error corrections. The forward and reverse models with corresponding error terms are shown in Figure 3.5. In two port error adapter model, two more terms the transmission tracking E_{TT}, and isolation E_X, are also included.
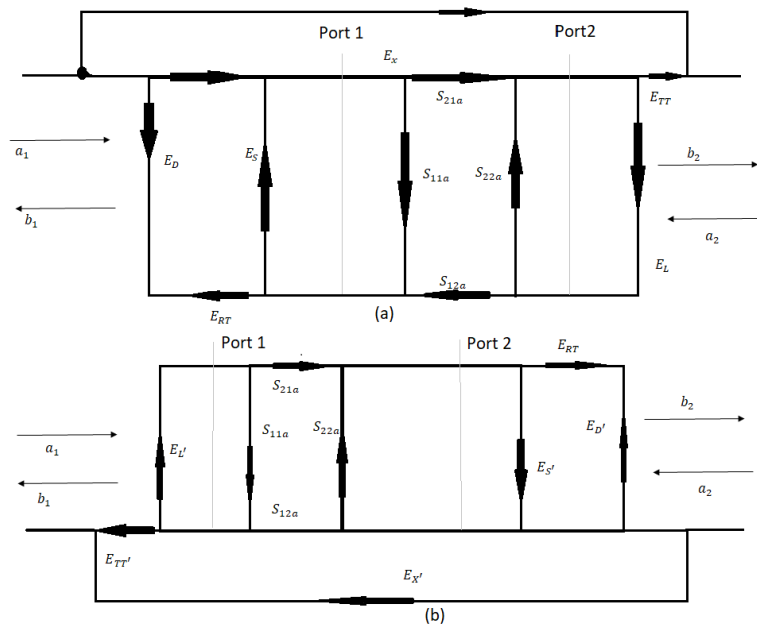
Figure 3.5. Systematic errors of network analyzer (a) Forward Model (b) Reverse model [44].

24

In this research, the SOLT standard is used to calibrate the network analyzer. This calibration shifts the reference plane to the end of the coaxial cable. As it is visible from Figure 3.1 that two waveguide straights are attached to the coaxial cable. For accurate measurement of transmission and reflection from the material, the reference plane must be on the material surface, which requires extra waveguide calibration.

3.1.3. Waveguide Calibration

The mathematical model for waveguide calibration is shown in Figure 3.6 given below. The most widely used calibration techniques for waveguides are Open-Short–Load (OSL), Short-Offset-Offset (SOO), and Through-Reflect-Line (TRL) calibrations [45].
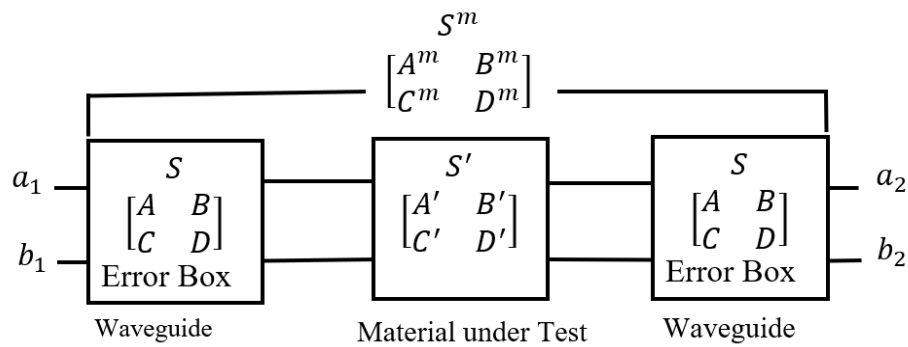
Figure 3.6. Mathematical model of the waveguide calibration [25].

The $\begin{bmatrix} A^m & B^m \\ C^m & D^m \end{bmatrix}$ or S^m are the scattering parameters of the cascaded system consist of coaxial to waveguide adapters, waveguide straights, and material under test. The $\begin{bmatrix} A & B \\ C & D \end{bmatrix}$ or S denoted as S-parameter of Error Box indicates combined scattering parameters of coaxial to waveguide adapter and waveguide straights. Whereas $\begin{bmatrix} A' & B' \\ C' & D' \end{bmatrix}$ or S' represent material under test.

In this study, we used the TRL calibration. Most of the network analyzer calibration techniques use known load standards like short, open, and matched. The imperfection in these standards can lead to errors in measurements. On the other hand, the TRL calibration techniques use simple connections to characterize error boxes. The through connection *Thru* represents the direct connection of waveguide ports. The block diagram and signal flow graph of the *Thru* link are shown in Figure 3.7. Scattering parameters obtained by using *Thru* are as

$$T_{11} = \frac{b_1}{a_1}|_{a_2=0} \quad = \quad S_{11} + \frac{S_{22}S_{12}^2}{1-S_{22}^2} \tag{3.7}$$

$$T_{12} = \frac{b_1}{a_2}\Big|_{a_1=0} \quad = \quad \frac{S_{12}^2}{1-S_{22}^2} \tag{3.8}$$

The symmetric and reciprocal design implies that $T_{11} = T_{22}$ and $T_{12} = T_{21}$ respectively.

The block diagram and signal flow graph of reflection connection are shown in Figure. 3.8. A good conducting plate is used as a reflector. The transmission coefficients are $R_{12} = R_{21} = 0$, while reflection coefficients can be calculated as

$$R_{11} = R_{22} = \frac{b_1}{a_1}\Big|_{a_2=0} \quad = S_{11} + \frac{S_{12}^2 \Gamma}{1-S_{22}\Gamma} \tag{3.9}$$
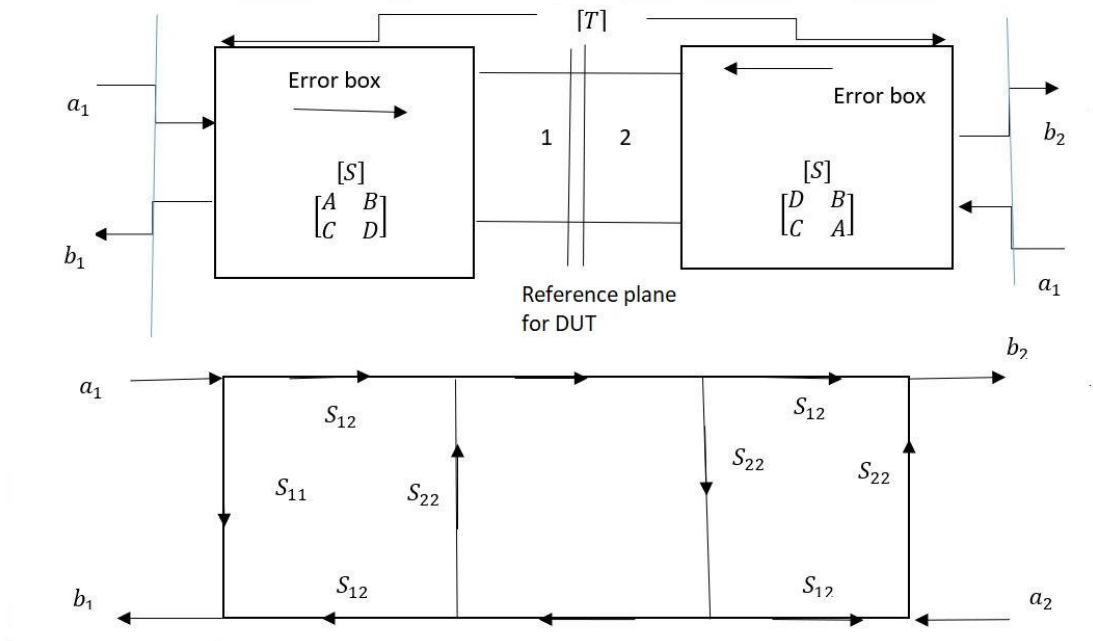
Figure 3.7. Block diagram and signal flow graph of *Thru* connection [25].

In line connection, a waveguide with arbitrary length is inserted between two waveguide straights. The block diagram and signal flow graph are shown in Figure 3.9. The transmission and reflection coefficients for line connections are calculated as given below. *L11* is the reflection coefficient and *L12* is the transmission coefficient of the line connection. where *l* is the length of line connection.

$$L_{11} = \frac{b_1}{a_1}\Big|_{a_2=0} \quad = S_{11} + \frac{S_{22}S_{12}^2 e^{-2\gamma l}}{1-S_{22}^2 e^{-2\gamma l}} \tag{3.10}$$

$$L_{12} = \frac{b_1}{a_2}\Big|_{a_1=0} \quad = \frac{S_{12}^2 e^{-2\gamma l}}{1-S_{22}^2 e^{-2\gamma l}} \tag{3.11}$$
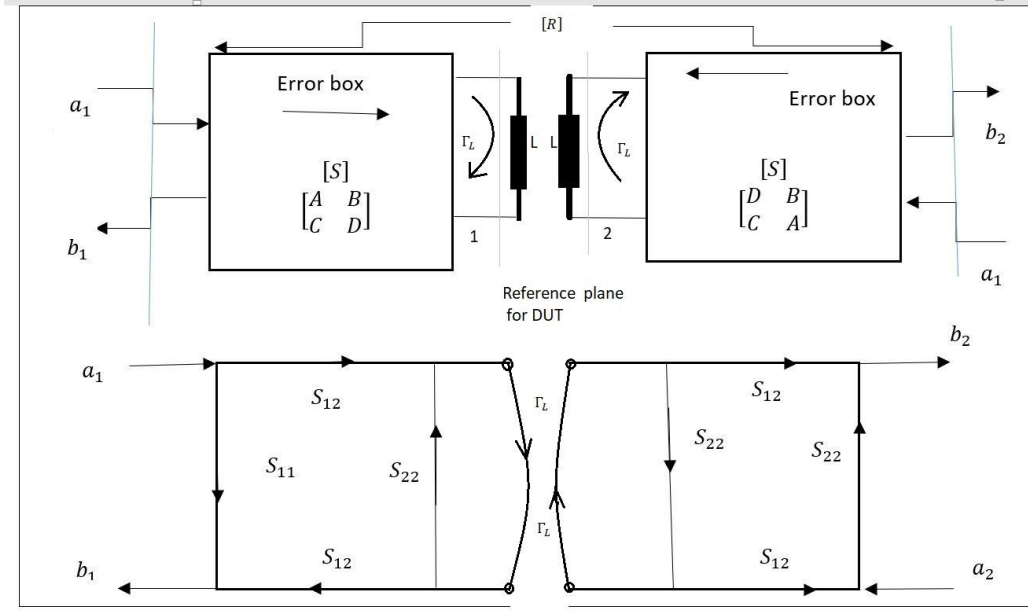
Figure 3.8. Block diagram and signal flow graph of reflection connection [25].
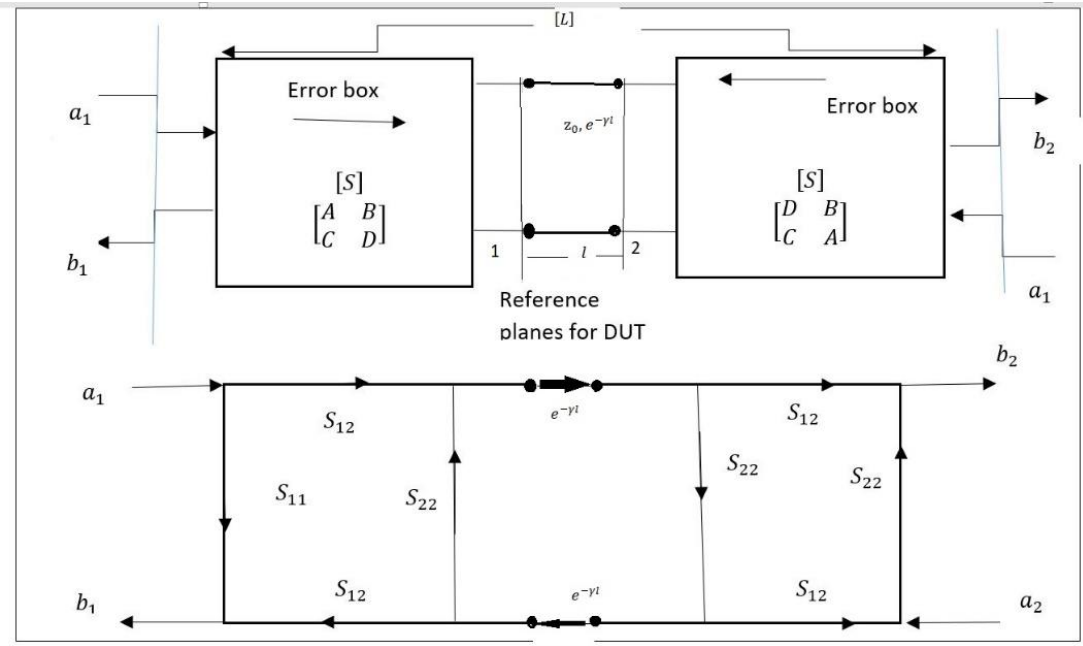
Figure 3.9. Block diagram and signal flow graph of line connections [25].

The propagation factor $e^{-\gamma l}$ and the S parameters of the error box are obtained by solving the above equations, the resulting equations are given below.

$$e^{-\gamma l} = \frac{L_{12}^2 + T_{12}^2 - (T_{11} - L_{11})^2 \pm \sqrt{\left[L_{12}^2 + T_{12}^2 - (T_{11} - L_{11})^2\right]^2 - 4L_{12}^2 T_{12}^2}}{2L_{12}T_{12}} \tag{3.12}$$

$$S_{22} = \frac{T_{11} - L_{11}}{T_{12} - L_{12}e^{-\gamma l}} \tag{3.13}$$

$$S_{11} = T_{11} - S_{22}T_{12} \tag{3.14}$$

27

$$S_{12}^2 = T_{12}(1 - S_{22}^2) \tag{3.15}$$

Finally, the reflection coeffect Γ_L can be calculated as

$$\Gamma_L = \frac{R_{11} - S_{11}}{S_{12}^2 + S_{22}(R_{11} - S_{11})} \tag{3.16}$$

To calculate dielectric properties correctly, the scattering parameters of the sample under test must be deduced from the scattering parameters of the cascaded system. For ease of calculation, the measured S-parameters are converted into ABCD parameters and then ABCD parameters of the sample are calculated by using the relation given below. In the end, the ABCD parameters are converted again into S-Parameters [25].

$$\begin{bmatrix} A' & B' \\ C' & D' \end{bmatrix} = \begin{bmatrix} A & B \\ C & D \end{bmatrix}^{-1} \begin{bmatrix} A^m & B^m \\ C^m & D^m \end{bmatrix} \begin{bmatrix} A & B \\ C & D \end{bmatrix}^{-1} \tag{3.17}$$

The Nicolson Ross Weir algorithm is used to determine unknown dielectric parameters of material under test from S-parameters derived from the cascaded system using the TRL technique.

3.1.4. Nicolson Ross Weir algorithm

The Nicolson Ross Weir algorithm is used to determine the dielectric properties from the S-parameters of the sample. The permeability and permittivity are determined by using the following formulation [46-47].

$$K = \frac{S_{11}^2 - S_{21}^2 + 1}{2S_{11}} \tag{3.18}$$

The reflection and transmission coefficients can then be calculated using the relations given in below.

$$\Gamma = K \pm \sqrt{K^2 - 1} \tag{3.19}$$

$$T = \frac{S_{11} + S_{21} - \Gamma}{1 - (S_{11} + S_{21})\Gamma} \tag{3.20}$$

After calculating the Γ and T the propagation constant of sample γ and propagation constant of the empty waveguide γ_0 are determined by using the following relations.

$$\gamma = \frac{\ln\left(\frac{1}{T}\right)}{d} \tag{3.21}$$

$$\gamma_0 = j\frac{2\pi}{\lambda_0} \tag{3.22}$$

Then relative permittivity ε_r and relative permeability of μ_r of material are determined by using reflection coefficient and propagation constants as shown in relation 3.23 and 3.24.

$$\varepsilon_r = \frac{\gamma}{\gamma_0} \frac{(1-\Gamma)}{(1+\Gamma)} \qquad (3.23)$$

$$\mu_r = \frac{\gamma}{\gamma_0} \frac{(1+\Gamma)}{(1-\Gamma)} \qquad (3.24)$$

There are some ambiguities in the results due to equation 3.21. The log of the imaginary part of the transmission coefficient (T) is equal to the angle of transmission coefficient plus $2\pi n$, where n is an integer multiple. This problem can be solved by using the phase unwrapping method. In the phase unwrapping method, the jump of more the π in the phase on consecutive frequencies must be detected, and then $2n\pi$ has to be added to shift the phase in the opposite direction. Figure 3.10 describes the phenomena of phase wrapping and unwrapping [24].
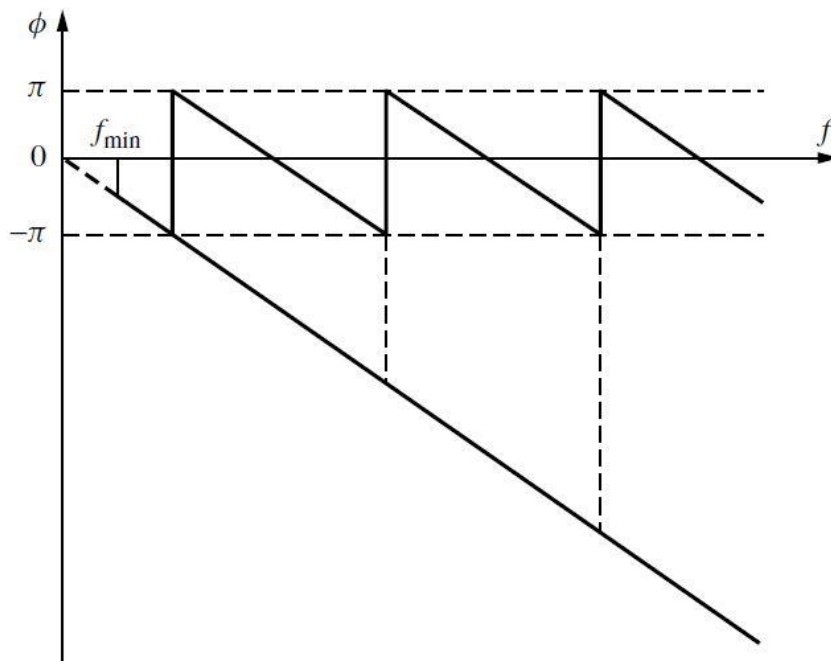
Figure 3.10. Phase unwrapping of the transmission coefficient.

From Figure 3.10, it can be seen that the phase of transmission coefficients (T) fluctuates between $-\pi$ and $+\pi$. After adding the $2n\pi$ the unwrapped phase of the transmission coefficient is also depicted in the figure.

Error correction for Improper Sample Preparation

Another source of error in measurements with the waveguide method is improper sample preparation due to which some air gaps appear between MUT and waveguide. The error in the measured values of relative permittivity and relative permeability is compensated by using the following relations [48]:

$$\varepsilon_m = \left(\frac{1-\Delta}{\varepsilon_s} + \frac{\Delta}{\varepsilon_g}\right)^{-1} \tag{3.25}$$

$$\mu_m = (1 - \Delta)\mu_s + \Delta\mu_g \tag{3.26}$$

where Δ is the correction factor and calculated as $\Delta = \left(\frac{b-b_s}{b}\right)$. ε_s and ε_g are the measured and gap permittivity whereas, μ_s and μ_g are measure and gap permeability respectively. The value b represents the height of the waveguide and b_s indicates the sample height.

Figure 3.11. represents the waveguide setup and prepared samples for the experiment.
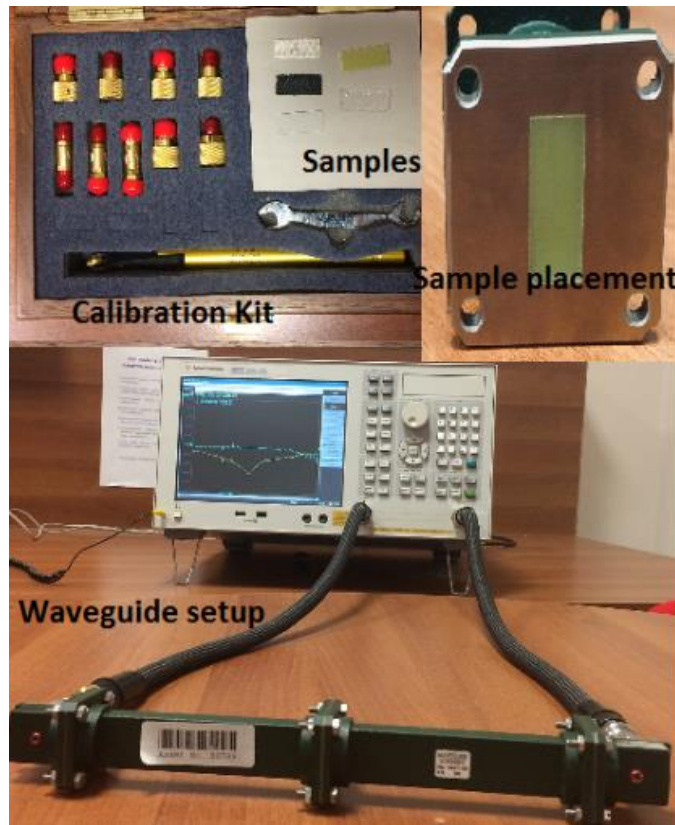
Figure 3.11. Waveguide setup, prepared samples, and sample placement.

3.2. Microstrip Planar Resonator

3.2.1. Microstrip Transmission Line

The dielectric constant of the substrate is one of the key parameters, which affect the resonant frequency of the microstrip structure [49-52]. In the resonance method, dielectric properties can be calculated in two different ways, one by analyzing resonance frequency through S-parameters and the other is measuring the group delays of the material for a particular resonance frequency [53]. Till now scientist has explored different planar resonant structure which includes microstrip lines, microstrip ring resonator, planar patch antennas [54-56].

In the S-parameters method, the material under test behaves as part of the resonant circuit and affects the resonance frequency. The resonance frequency is first determined from S-parameters, and then the permittivity of a material is calculated from resonance frequency relation, which is given below:

$$f_{rn} = \frac{nc_o}{2L_{eff}\sqrt{\varepsilon_{reff}}} \tag{3.27}$$

$$\varepsilon_{reff} = \left(\frac{nc_o}{2L_{eff}\,f_{rn}}\right)^2 \tag{3.28}$$

where f_{rn} is the resonance frequency, ε_{reff} is the effective relative permittivity and L_{eff} is the effective length. The relative permittivity ε_r is derived from equation 3.29 given below.

$$\varepsilon_{reff} = \begin{cases} \frac{\varepsilon_r+1}{2} + \frac{\varepsilon_r-1}{2}\left[\left(1 + 12\left(\frac{h}{w}\right)\right)^{-\frac{1}{2}}\right] & \frac{w}{h} < 1 \\ \frac{\varepsilon_r+1}{2} + \frac{\varepsilon_r-1}{2}\left[\left(1 + 12\left(\frac{h}{w}\right)\right)^{-\frac{1}{2}} + 0.04\left(1 + \frac{w}{h}\right)^2\right] & \frac{w}{h} \geq 1 \end{cases} \tag{3.29}$$

The microstrip transmission line or microstrip patch structure is suitable for determining the material's dielectric properties for very few discrete frequencies. The loop-like microstrip planar structures can increase the number of resonance harmonics that enrich the frequency range [57]. The microstrip resonator technique requires the fabrication of microstrip structure on every material under test, and the fabrication process is very complicated for some materials. This research has fabricated a microstrip transmission line on cotton and FR4 substrates due to ease of fabrication.

The dimension of the microstrip line on cotton and FR4 substrate are enlisted in Table 3.1 whereas, Figure 3.12 depicts fabricated designs.

Table 3.1.Dimensions of microstrip line for cotton and FR4 substrate.

Parameter	Value (mm) Cotton	Value (mm) FR4
W	12.53	3
L	39	50
H	0.4	1.5
T	0.16	0.035
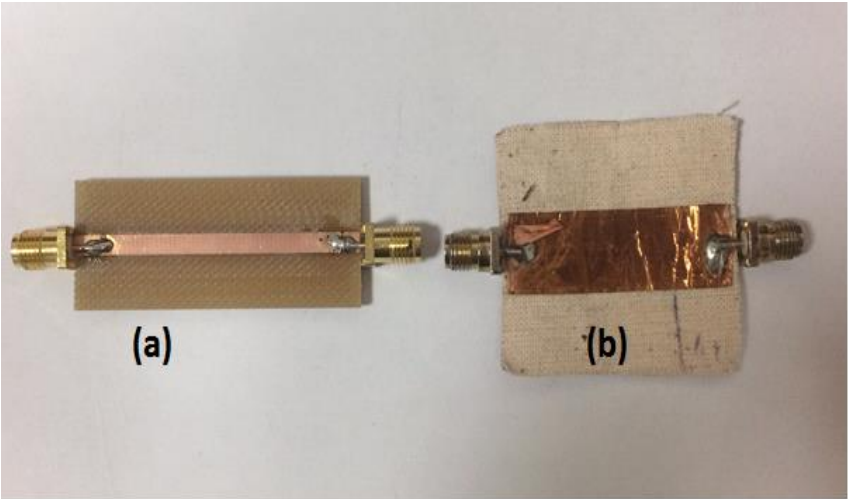
Figure 3.12. (a) Transmission line fabricated on FR4. (b) Transmission line fabricated on cotton textile.

3.2.2. Modified Microstrip Ring Resonator Technique

An improved version of the microstrip resonator method is a multilayer microstrip resonator structure technique, where the different substrate layers are stacked on a resonator structure and then dielectric properties are analyzed from resonance frequency shift due to that stacked material [58- 60].

A two-layer technique with a microstrip ring resonator and the material whose dielectric constant must be measured is placed on top is as shown in Figure 3.13 below.
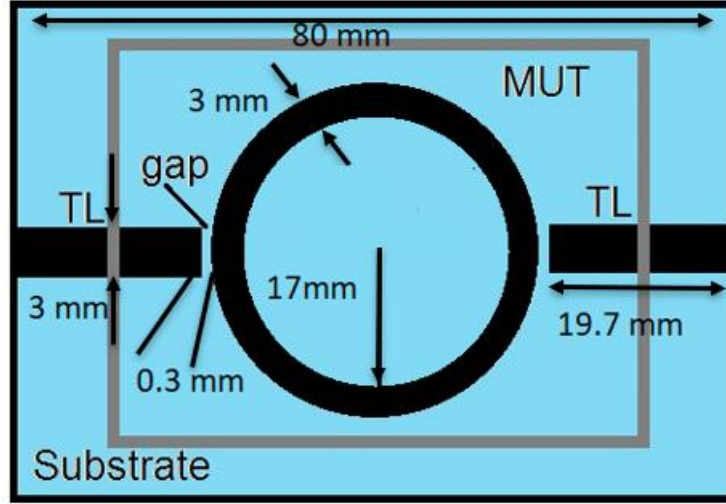
Figure 3.13. Multilayer microstrip ring resonator.

The sample piled on top of the ring resonator must be large enough to cover the ring and the coupling gaps between the transmission line and the ring resonator to overcome fringing fields. The effective dielectric constant ε_{eff2} of the setup having a ring resonator and material on top of it is calculated from the shift in the resonance frequency of the ring resonator with and without material, mathematically represented as under [60].

$$\varepsilon_{eff2} = \left(\frac{f_{r1}}{f_{r2}}\right)^2 \varepsilon_{eff1} \tag{3.30}$$

where ε_{eff1} is the effective dielectric constant one layer structure i.e. microstrip ring resonator without material on top of it. The f_{r2} and f_{r1} are the resonance frequency of the ring resonator with and without the sample, respectively.

The relative dielectric constant of the sample ε_{r2} is calculated by using the following formula.

$$\varepsilon_{r2} = \frac{q_2}{q_1 + q_2 - 1 + \frac{(1-q_1)^2}{\varepsilon_{eff2} - q_1 \varepsilon_{r1}}} \tag{3.31}$$

q_1 and q_2 are the Wheeler filling factors for 2-layer geometry and can be calculated by using the relation presented in [61].

$$q_1 = \begin{cases} 1 - \frac{1}{2} \frac{ln\left(\frac{\pi}{h} w_{ef} - 1\right)}{\frac{w_{ef}}{h}} & \frac{w}{h} \geq 1 \\ \frac{1}{2} + \frac{0.9}{\pi \cdot \frac{h}{w}} & \frac{w}{h} < 1 \end{cases} \tag{3.32}$$

$$q_2 = \begin{cases} 1 - q_1 - \dfrac{1}{2}\dfrac{h-v_e}{w_{ef}} \, ln\left[\pi \dfrac{w_{ef}}{h} \dfrac{cos\left(\frac{v_e}{2}\cdot\frac{\pi}{h}\right)}{\pi\left(\frac{h_2}{h}-\frac{1}{2}\right)+\frac{v_e}{2}\cdot\frac{\pi}{h}} sin\left(\frac{v_e}{2}\cdot\frac{\pi}{h}\right)\right] & \dfrac{w}{h} \geq 1 \\[2em] \dfrac{1}{2} - \dfrac{0.9+\frac{\pi}{4}ln\left(\frac{\frac{h_2}{h}+1}{\frac{h_2}{h}+\frac{w}{4h}-1}\right)\cdot arccos\left\{\left[1-\frac{h}{h_2}\left(1-\frac{w}{8h}\right)\right]\sqrt{\frac{\frac{h_2}{h}+1}{\frac{h_2}{h}+\frac{w}{4h}-1}}\right\}}{\pi\cdot ln\frac{8h}{w}} & \dfrac{w}{h} < 1 \end{cases} \tag{3.33}$$

where h is the substrate height of microstrip ring resonator, h_2 is the height of two-layer structure, w and w_{ef} are the width and the effective width of the conductive trace, respectively.

$$w_{ef} = w + \frac{2h}{\pi} \, ln\left[17.08\left(\frac{w}{2h}+0.92\right)\right] \tag{3.34}$$

The quantity v_e is defined given below

$$v_e = 2\frac{h}{\pi} arctg\left[\frac{\pi}{\frac{\pi}{2}\frac{w_{ef}}{h}-2}\left(\frac{h_2}{h}-1\right)\right] \tag{3.35}$$

The dimension of the ring resonator is given below.

Table 3.2 Microstrip Ring Resonator dimensions

Parameter	Value (mm/GHz)
R	17
w	3
L_r	19
t_r	0.035
h	1.5
G_{ap}	0.3
f_{r1}	1.66

Where r is the inner ring radius, w is the width of the conductor, L_r is the length of the transmission line of the microstrip ring resonator, t_r is the thickness of the conductor, G_{ap} is the coupling gap between ring and transmission lines, whereas f_{r1} is the resonance frequency of microstrip ring resonator without material on it. The insertion loss of a ring resonator with and without sample material is shown in Figure 3.14. Whereas the experimental setup and prepared sample are depicted in Figure 3.15.
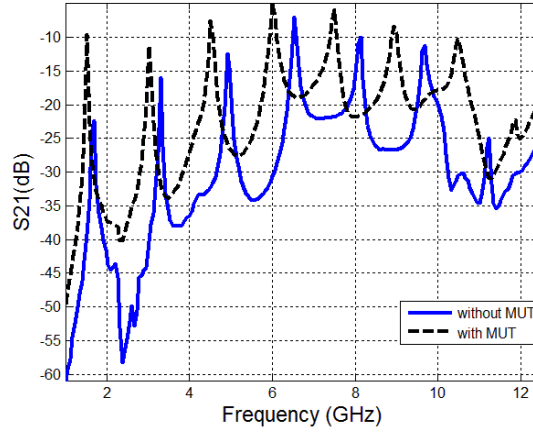
Figure 3.14. Insertion loss of ring resonator with and without material layer.
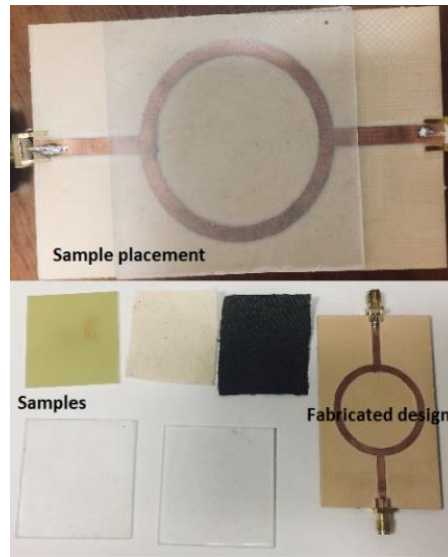
Figure 3.15. Experimental setup, prepared sample, and fabricated design.

To measure the loss factor of material under test, we assume that superimposed test material has a negligible effect on conductor and radiation loss of microstrip ring resonator, which implies that

$$\frac{1}{Q_{D2}} - \frac{1}{Q_{D1}} = \frac{1}{Q_2} - \frac{1}{Q_1} \tag{3.36}$$

The resonance frequency and 3dB bandwidth are considered the main parameters, which vary due to the inclusion of the second layer. The unloaded Q-factor of the one and two-layer setup represents through Q_1 and Q_2 respectively, and can be computed from the measured insertion loss (L) and 3dB bandwidth (BW) of the microstrip ring resonator by using the following relation [60].

$$Q_i = \frac{f_{ri}}{BW_i} \frac{1}{1 - 10^{-L/20}} \tag{3.37}$$

35

Where f_r represents resonance frequency, and i is the index for one layer and two-layer setup. The Q_{D1} and Q_{D2} are the dielectric losses of the one layer and two-layer setup respectively and are related to the loss tangent $tan\delta$ through the following relation

$$\sum_{i=1}^{N} p_{i,N} tan\delta_i = \frac{1}{Q_{Di}} \tag{3.38}$$

Here $p_{i,N}$ is the Schneider filling factor for ith layer, for two-layer setup N=2. The filling factor for the respective layer can be calculated by using the procedure given in reference [60].

3.3.   Results and Measurements

The results of all the test samples measured with the waveguide, microstrip transmission line, and modified ring resonator techniques are presented in this section. The estimated S-parameters magnitude and phase of the empty waveguide and Error box are shown in Figure 3.16 and Figure 3.17, respectively.
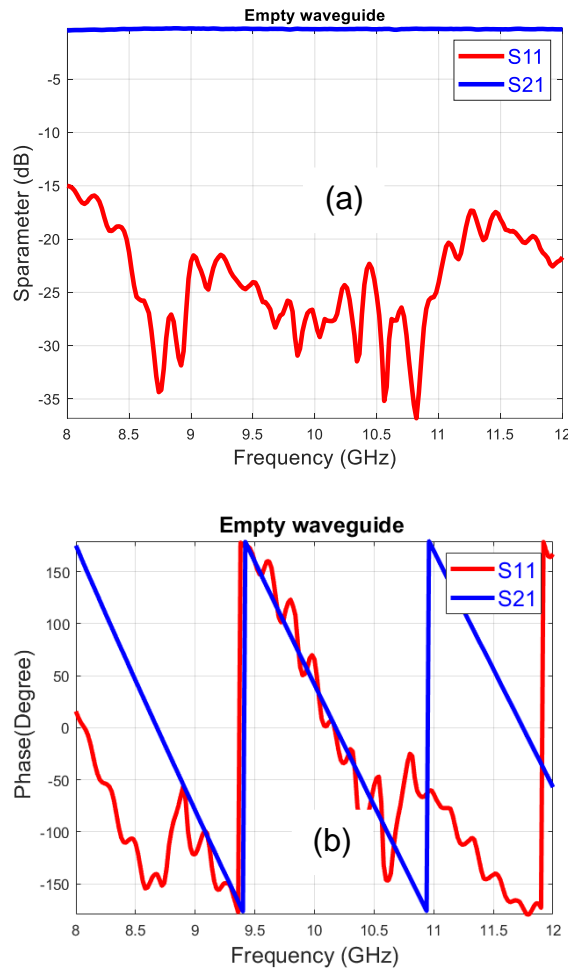
Figure 3.16. S-Parameter of the empty waveguide. (a) Magnitude in dB. (b) Phase in degree.

36
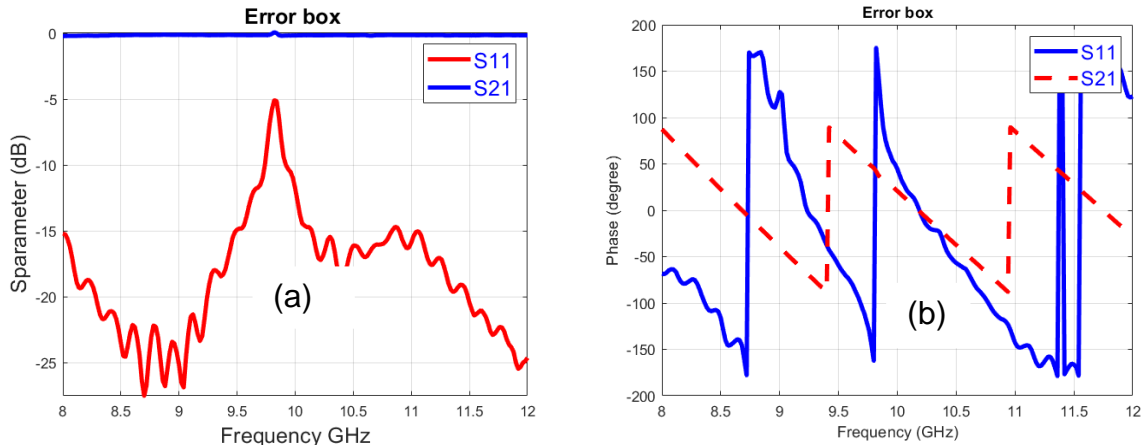
Figure 3.17. S-Parameters of the error box. (a) Magnitude in dB. (b) Phase in degree.

3.3.1. Textile Material

Wearable Electronics is the emerging trend in the electronic industry, which encourages scientists to explore new flexible dielectric materials to use as an alternative to the conventional rigid dielectric substrate. Due to low-cost roll-to-roll production, flexibility, and ease of fabrication of circuits, textile has now become a good alternative for use as a substrate. The textiles are very porous; they absorb water, different weather condition like humidity and temperature affect their dielectric properties. Due to these reasons, it is essential to determine the exact dielectric behavior of textiles before using them as a substrate for microwave and RF circuits.

Cotton and jeans are the most widely used low-cost textile, are used for test measurements. They have low dielectric constant and loss factor, which make them very suitable for wearable antennas. The test results by using the resonant and non-resonant methods for both materials are presented.

Figure 3.18 represents the S-Parameters and phase of the cascaded system whereas, extracted S-Parameters are shown in Figure 3.19. The correct S-Parameters of material are deduced from measured S-Parameters of the cascaded system through the TRL calibration method. Figure 3.18 (a) shows the S-parameter magnitude in dB of cascaded system, and Figure 3.18(b) indicates the S-Parameter phase in degrees of cascaded system. The S-Parameters magnitude (dB) and phase (degree) of the cotton sample are presented in Figure 3.19 (a) and Figure 3.19 (b), respectively.

37

Figure 3.18. S-Parameters of cascaded system. (a) S-Parameters magnitude in dB. (b) Phase in degree.
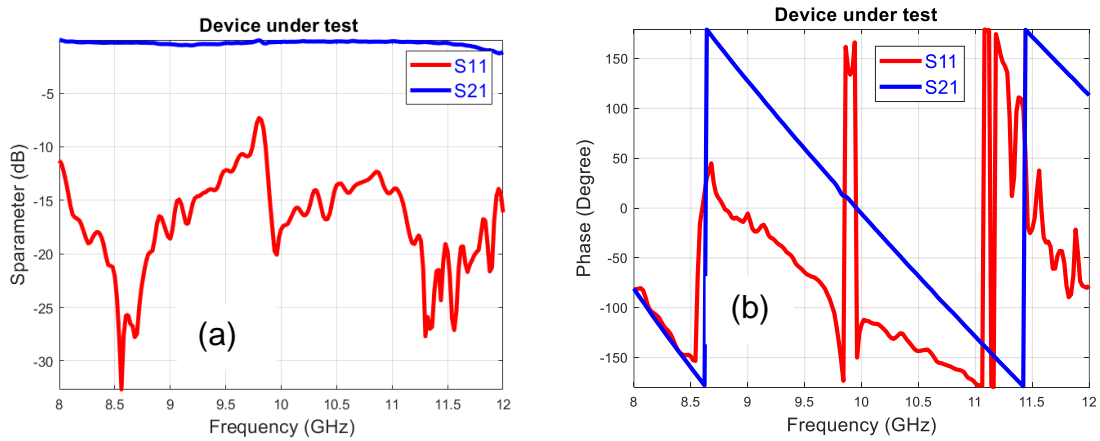
Figure 3.19. S-Parameters of cotton. (a) S-Parameters magnitude in dB. (b) Phase in degree.

The NRW algorithm is used to calculate the dielectric properties of textile material from the deduced S-Parameters of material. The reflection and transmission coefficients are determined by using equations 3.19 and 3.20. As described above, one of the significant sources of error in the calculation is phase error in transmission coefficient, which arises due to phase wrapping between $-\pi$ and $+\pi$. The error compensation by using phase unwrapping for the cotton sample is shown in Figure 3.20.
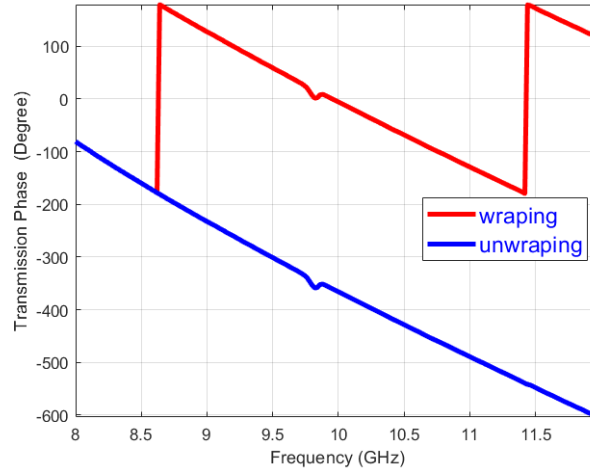
Figure 3.20. Transmission phase wrapping and unwrapping.

The calculated dielectric constant ε_r' and loss factor ε_r'' for 0.35 mm thick cotton material through the waveguide method are shown in Figure 3.21. The red line represents the dielectric constant, whereas the blue represents the loss factor. It can be observed that the average dielectric constant is around $\varepsilon_r' = 1.68$, and the loss factor is $\varepsilon_r'' = 0.038$. Some spontaneous peaks are observed in both dielectric constant and loss factor curves on specific frequencies. These improvised peaks are; a well-known issue related to NRW algorithm. These peaks arise whether the material is so thick that its thickness becomes equal to the integral multiple of half of the wavelength in the material or so thin that the coupling fringing effect produced between opposite faces of the material becomes more prominent.

Moreover, these peaks have also emerged due to discontinuities in measured and extracted S-Parameters due to random error, drift error, or shortcoming in the calibration process. These discontinuities become more prominent in thin and low-loss materials due to inaccurate measurements of S_{11}-parameter. It can be seen in Figure 3.17 that there is a discontinuity in S-Parameters of the Error box constructed through the TRL method. This discontinuity in extracted S-Parameters of DUT is the reason for the sharp peaks in relative permittivity results.
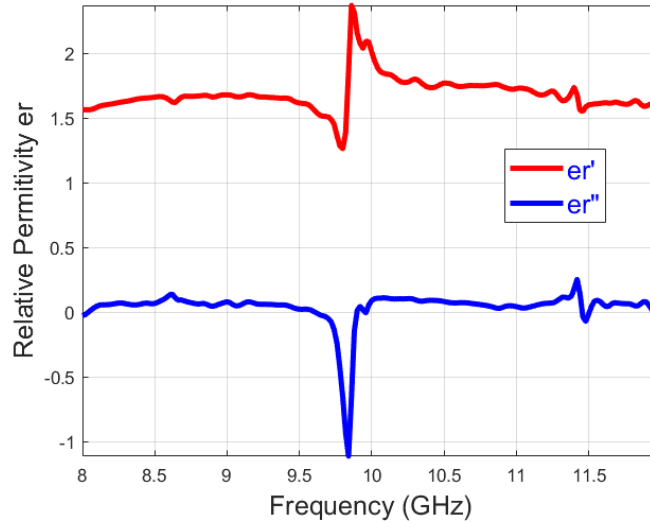
Figure 3.21. The relative permittivity of cotton.

The return loss and calculated dielectric constant of the microstrip line fabricated on the cotton textile using sticky copper tape having dimensions mentioned in table 3.1 are given in Figure 3.22.
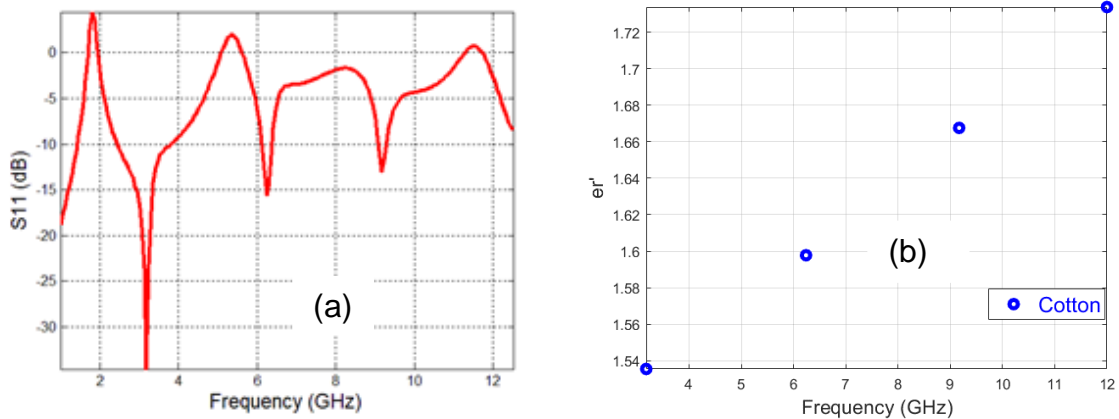
Figure 3.22. S11 parameter of a microstrip line on a cotton substrate. (b) The dielectric constant calculated by using the microstrip transmission line.

From Figure 3.22 (a), it can be observed that the resonance frequency of the microstrip transmission line is at 3.18 GHz having harmonics at 6.24 GHz and 9.17 GHz. The dielectric constant calculated by using relation 3.29 is plotted in Figure 3.22 (b).

The S-parameters and dielectric constant obtained through the modified microstrip ring resonator technique are given in Figure 3.23.
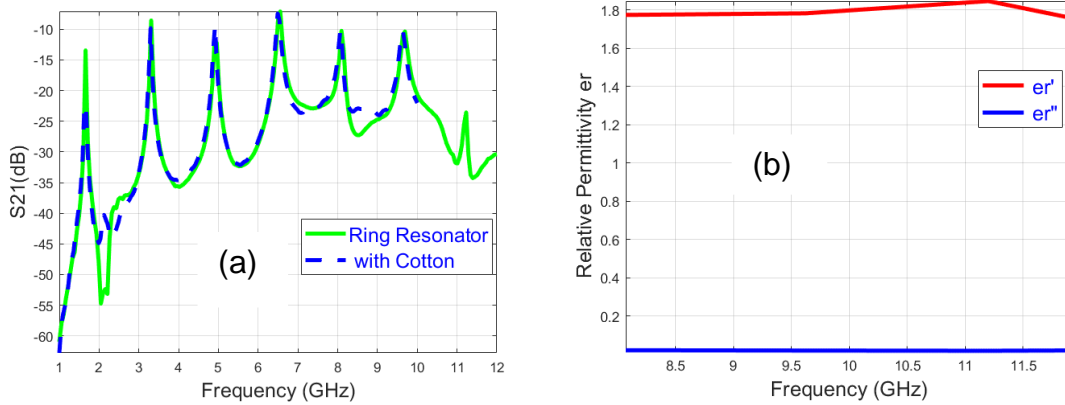
Figure 3.23. S21-Parameters of modified ring resonator method. (b) Calculated relative permittivity.

In Figure 3.23 (a) the red line represents S_{21} parameter of the ring resonator, and the blue line represents the S_{21} parameter after placing the cotton sample on the top of the ring resonator. It is worth noting that the resonance frequency is 1.69 GHz, but the number of harmonics for ring resonator structures is much more than the microstrip transmission line structure. It can be noted that there is no significant shift in resonance frequency for cotton material. Figure 3.23 (b) specifies the calculated real and imaginary part of relative permittivity of cotton textile through the modified ring resonator method.

The comparison of the real and imaginary part of relative permittivity calculated through all the three techniques for X- band frequencies are given in Figure 3.24 (a) and (b) respectively.
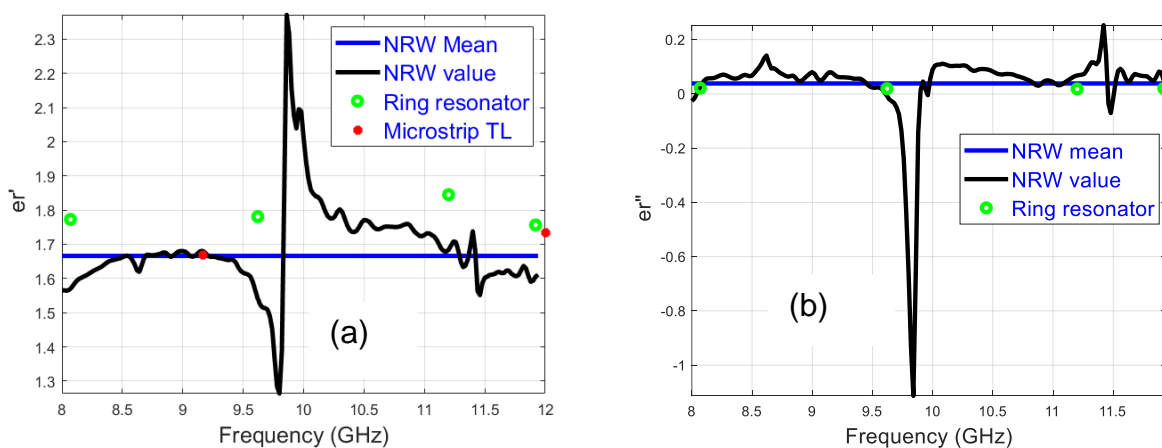
Figure 3.24. Comparison of relative permittivity of cotton measured through resonant and non resonant techniques. (a) Dielectric constant. (b) Loss factor.

The mean value of the dielectric constant for the waveguide method is 1.68 while the loss factor is equal to 0.038. When compared with the modified ring resonator method these values are turn out to be 1.78 and 0.02 respectively. The average dielectric constant of cotton textile through microstrip transmission line for X-band frequency is around 1.70.

Jeans fabric is traditionally made from cotton wrap and is very similar to cotton; its dielectric constant is expected to be near to that of cotton material. Figures 3.25 and 3.26 show the measured S-Parameters of the complete cascaded system and extracted S-Parameters for the jeans sample.
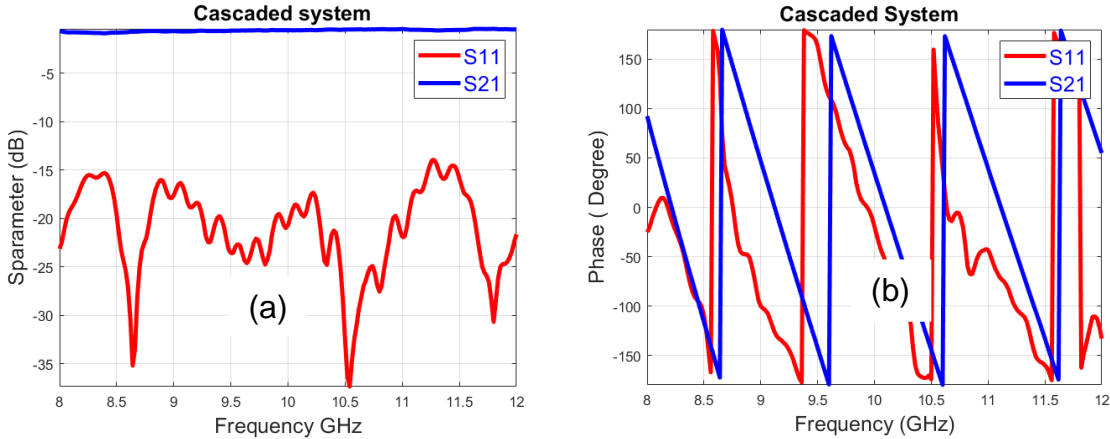
Figure 3.25. S-Parameters of cascaded system. (a) S-Parameters magnitude in dB. (b) Phase in degree.
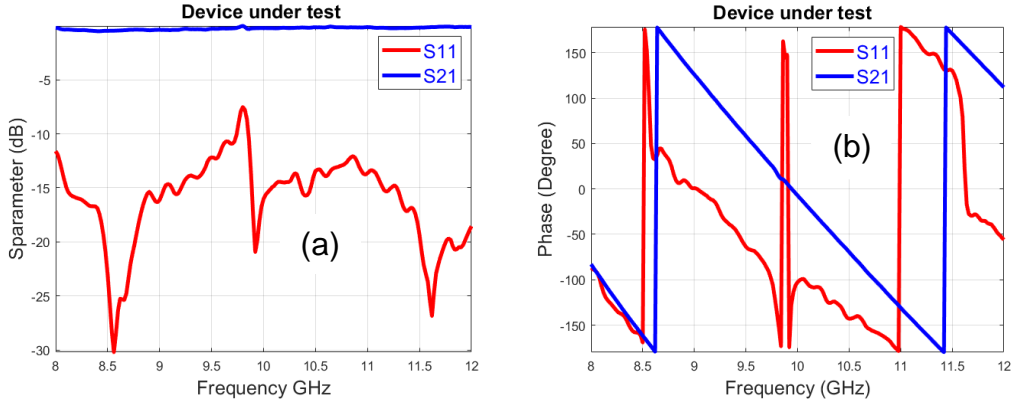
Figure 3.26. S-Parameters of Jeans. (a) S-Parameters magnitude in dB. (b) Phase in degree.
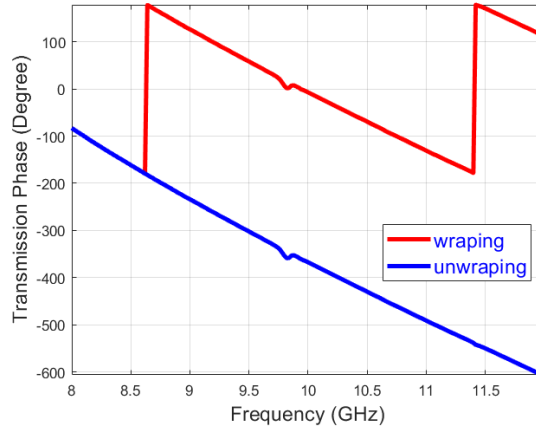
Figure 3.27. Transmission phase wrapping and unwrapping.
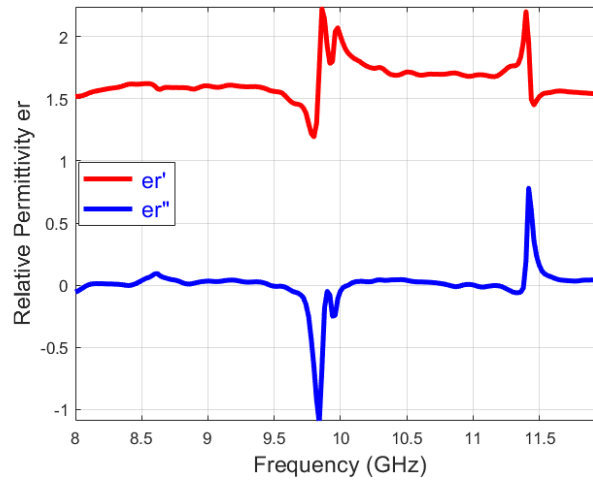
Figure 3.28. The relative permittivity of jeans through the waveguide method.
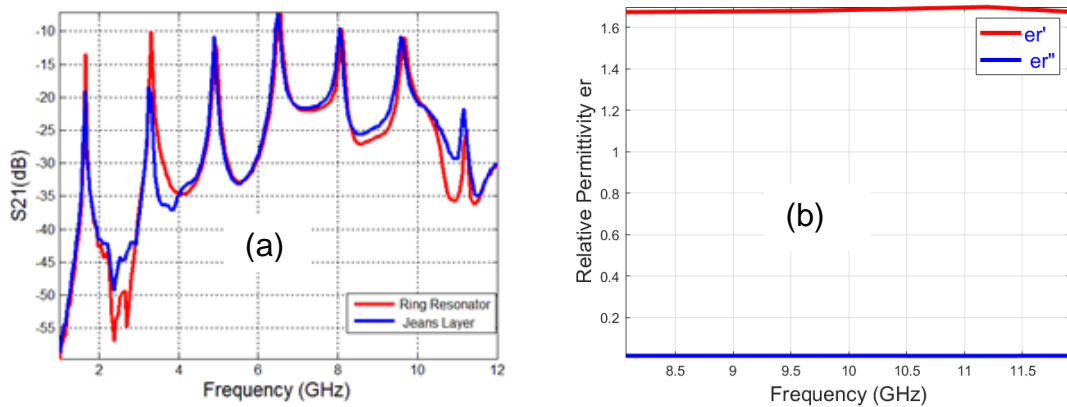
Figure 3.29. S21-Parameters for modified ring resonator. (b) The relative permittivity of jeans.
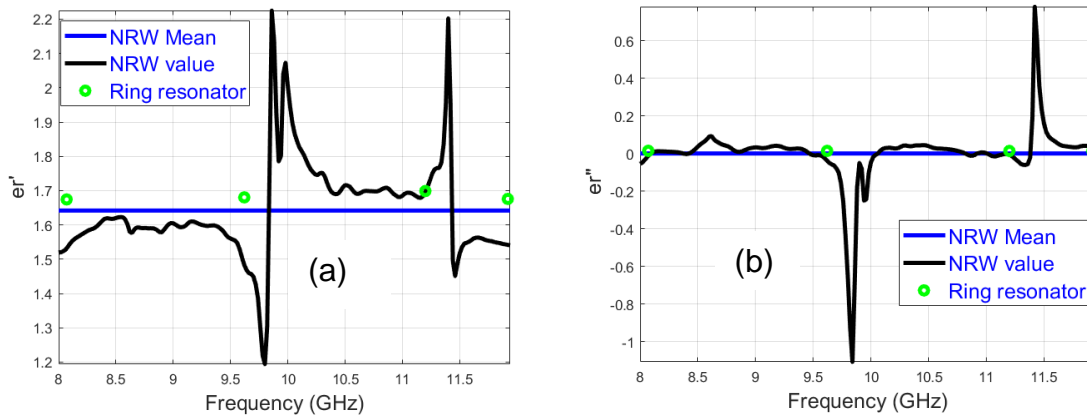
Figure 3.30. Comparison of relative permittivity for jeans. (a) Dielectric constant (b) Loss factor.

The Figure 3.28-3.30 represent results for relative permittivity of jeans by using the waveguide and the microstrip ring resonator method. The 0.6 mm thick jeans sample is used in the experiment. The mean value of the dielectric constant for jeans calculated using the waveguide method is $\varepsilon_r' = 1.65$ while the loss factor is $\varepsilon_r'' = 0.001$ as shown. The dielectric constant of jeans achieved the microstrip ring resonator method is about 1.68 whereas the loss factor is 0.011.

3.3.2. Synthesized Materials

The two synthesized materials, Polydimethylsiloxanes (PDMS) and silicone-based Ak-Sil T1310 are tested for electromagnetic properties. PDMS and silicone have excellent electro-mechanical properties, due to which these materials are widely used in actuators, generators, and sensors. The elastomer and biodegradable nature of both materials make them an excellent candidate for flexible electronics.

These materials are primarily synthesized in laboratories, which causes the dielectric properties of these materials can differ from sample to sample. Their dielectric properties mainly depend upon the amount and type of additive, elongation, toughness, and viscosity of crude silicone, and atmospheric condition of the laboratory.
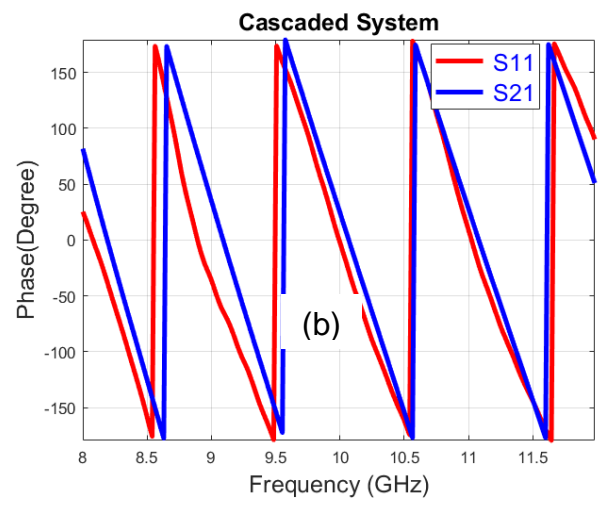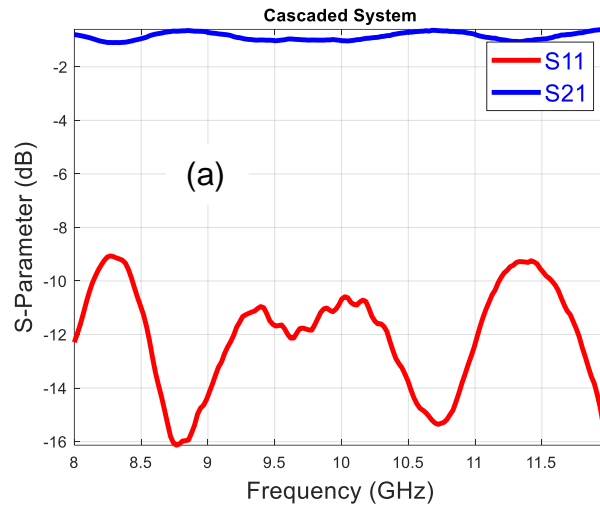
Figure 3.31. S-Parameters of cascaded system. (a) S-Parameters magnitude in dB. (b) Phase in degree.
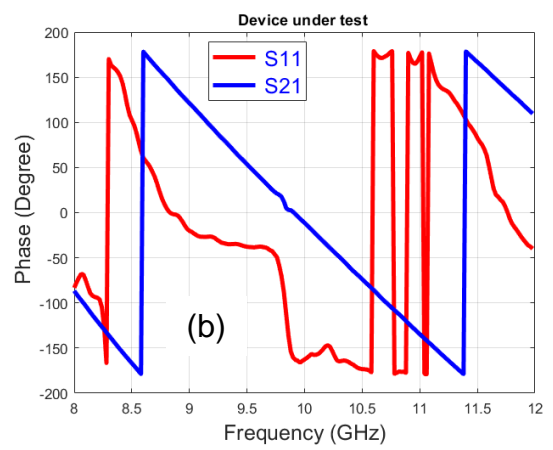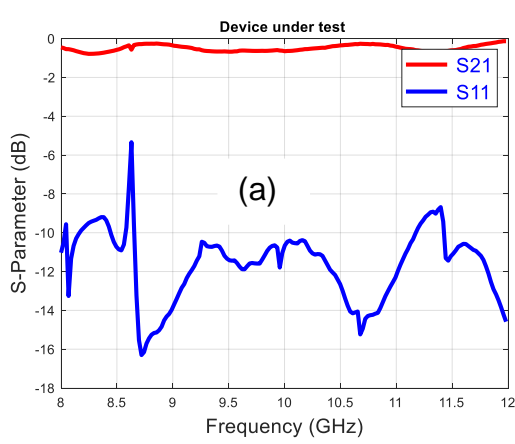
Figure 3.32. S-Parameters of PDMS. (a) S-Parameters magnitude in dB. (b) Phase in degree.
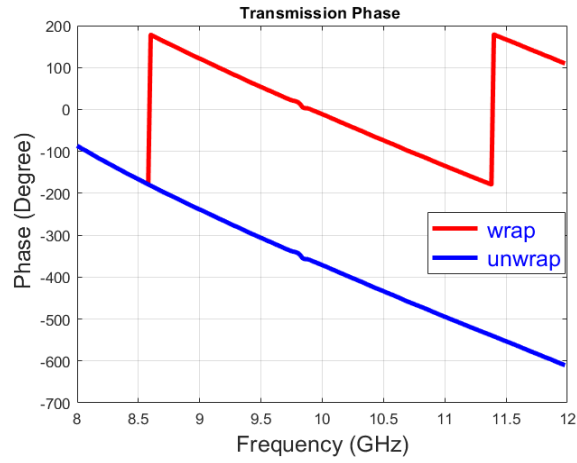
Figure 3.33. Transmission phase wrapping and unwrapping.
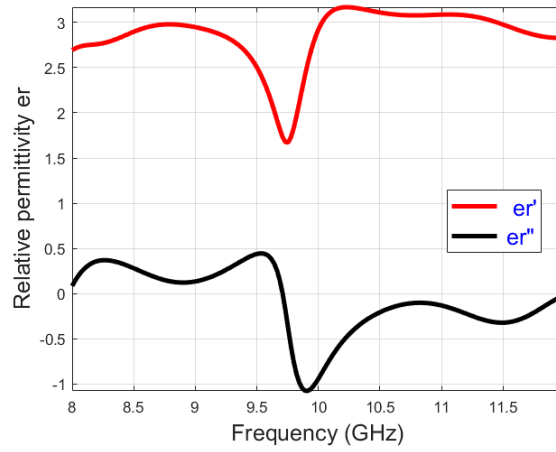
Figure 3.34. The relative permittivity of PDMS.
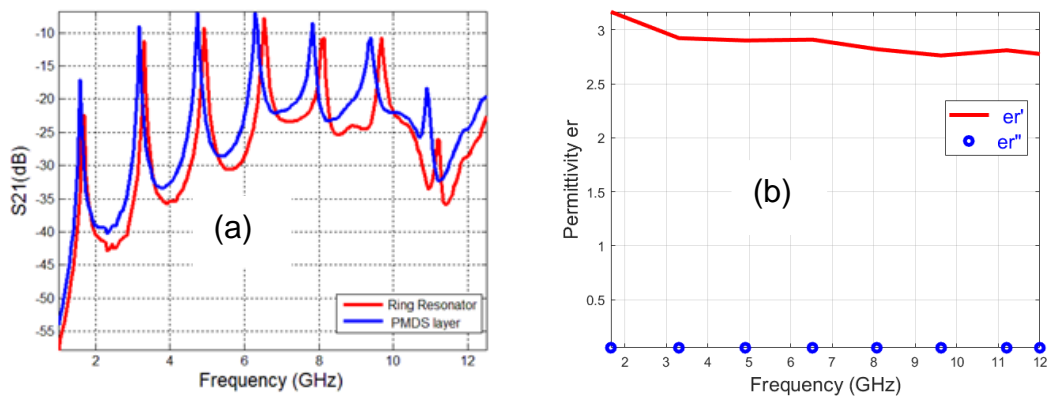
Figure 3.35. S21-Parameters of modified ring resonator technique for PDMS
material. (b) The relative permittivity of PDMS.
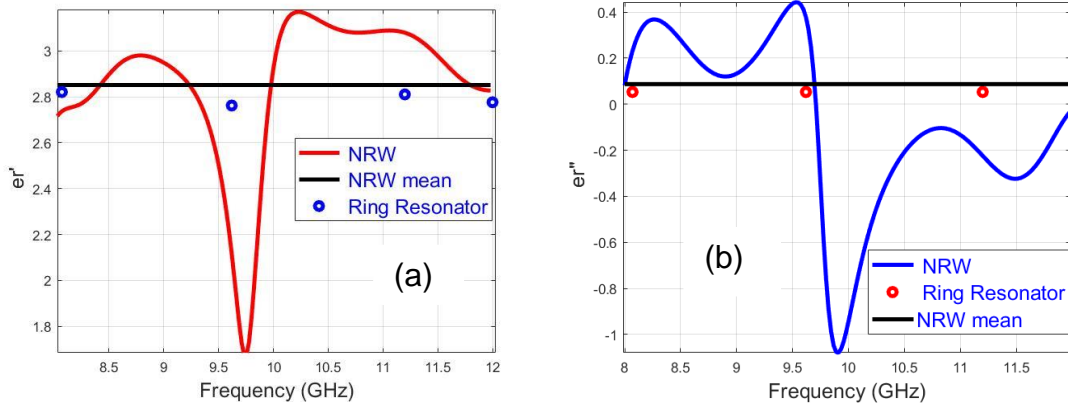
Figure 3.36. Comparison of the relative permittivity of PDMS. (a) Dielectric constant. (b) Loss factor.

Figure 3.34 represents relative permittivity results achieved through the waveguide method for the PDMS sample. Figure 3.35 represents the results from the modified ring resonator method, while Figure 3.36 shows a comparison between both methods. The results show that the dielectric constant and loss factor of 1 mm thick sample calculated by using waveguide has a mean value $\varepsilon'_r = 2.84$ and $\varepsilon''_r = 0.079$. In contrast, from the modified ring resonator technique, the dielectric constant is $\varepsilon'_r = 2.7$ and loss factor is $\varepsilon''_r = 0.05$ respectively.
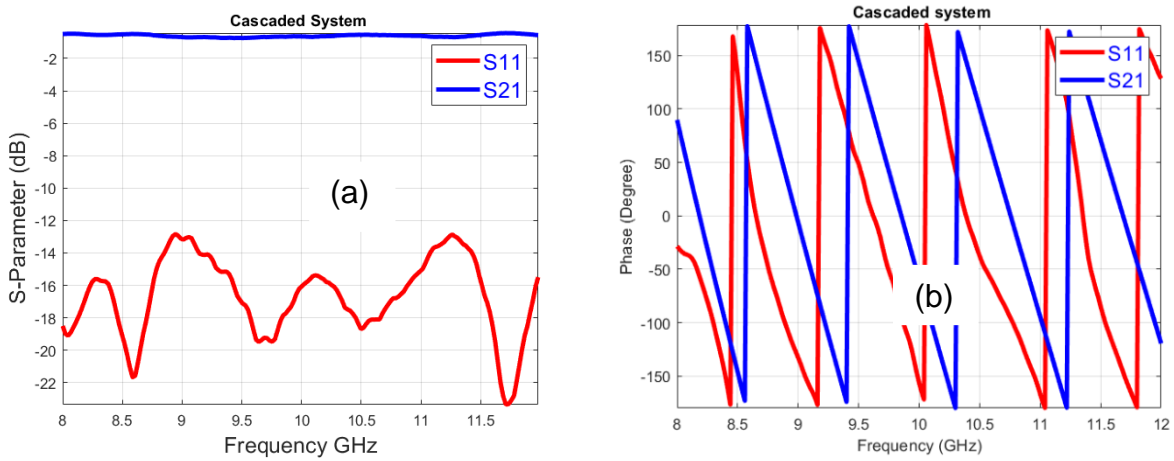
Figure 3.37. S-Parameters of cascaded system. (a) S-Parameters magnitude in dB. (b) Phase in degree.
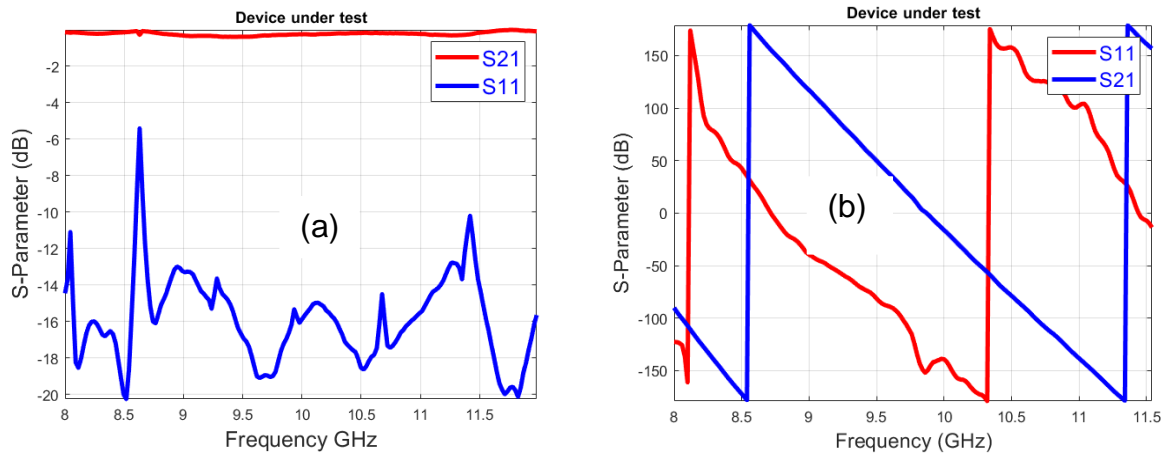
Figure 3.38. Deduced S-Parameter of Ak-Sil T1310. (a) Magnitude in dB. (b) Phase in degree.
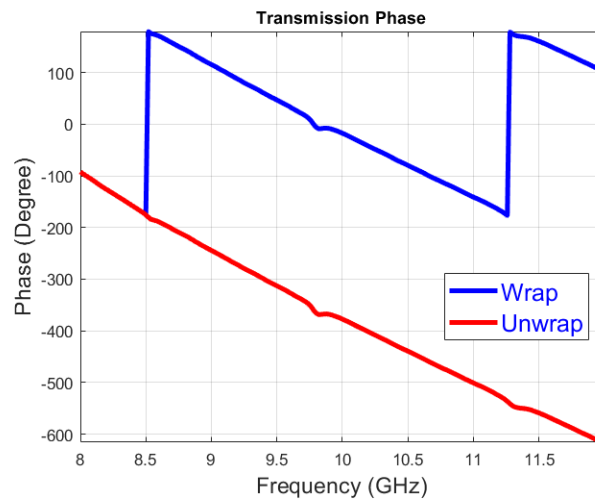
Figure 3.39.. Transmission phase wrapping and unwrapping.
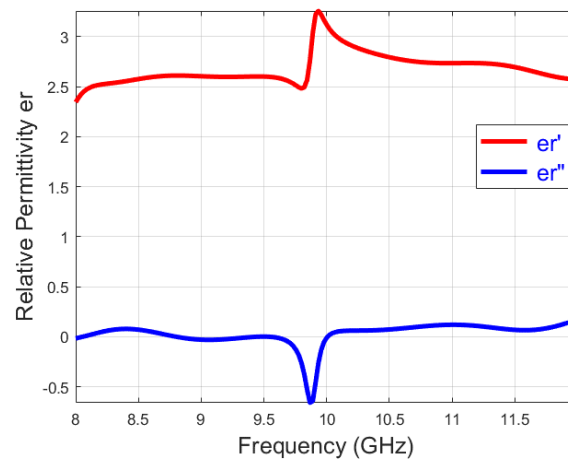
Figure 3.40. Relative permittivity of AK-Sil T1310.
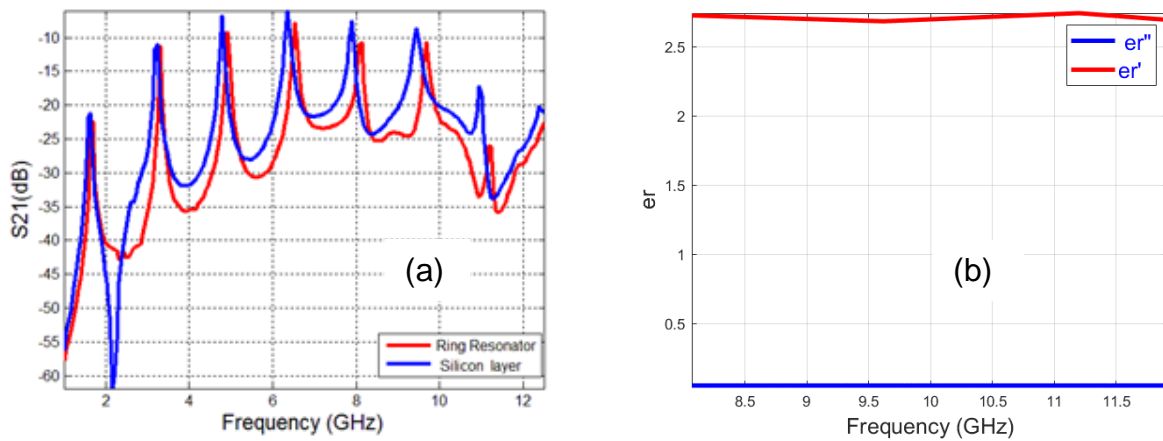
Figure 3.41. S21-Parameters of modified ring resonator technique with AK-Sil T1310 material. (b) The relative permittivity of AK-Sil T1310.
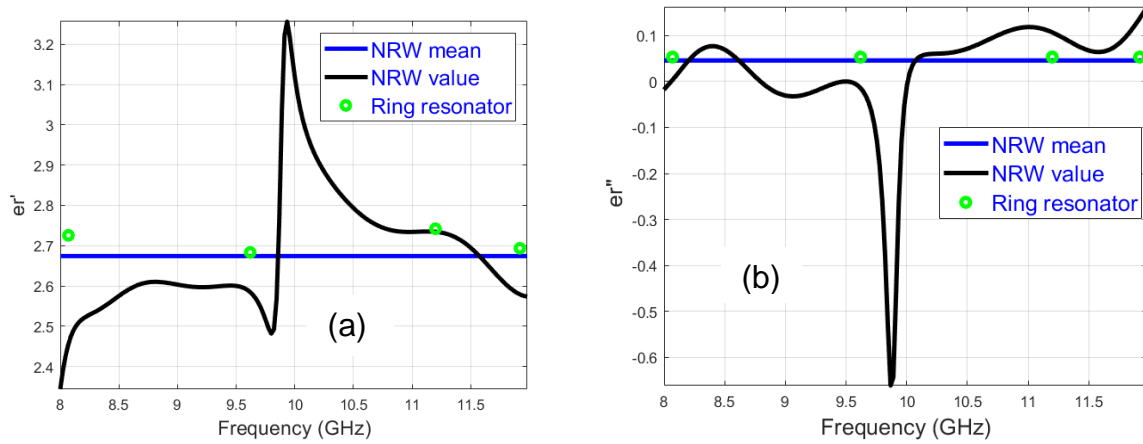
Figure 3.42. Comparison of relative permittivity of AK-Sil T1310 material. (a) Dielectric constant . (b) Loss factor.

Figures 3.39-3.41 are for 0.9 mm thick silicone-based Ak-Sil T1310 material. From the waveguide method, the calculated dielectric constant and loss factor are $\varepsilon_r' = 2.67$ and $\varepsilon_r'' = 0.045$, respectively. While for the modified ring resonator technique, the dielectric constant $\varepsilon_r' = 2.7$ and loss factor $\varepsilon_r'' = 0.05$ are obtained.

The results for all the materials are authenticated by measuring the dielectric constant of the most used FR4 substrate through all the three techniques discussed.
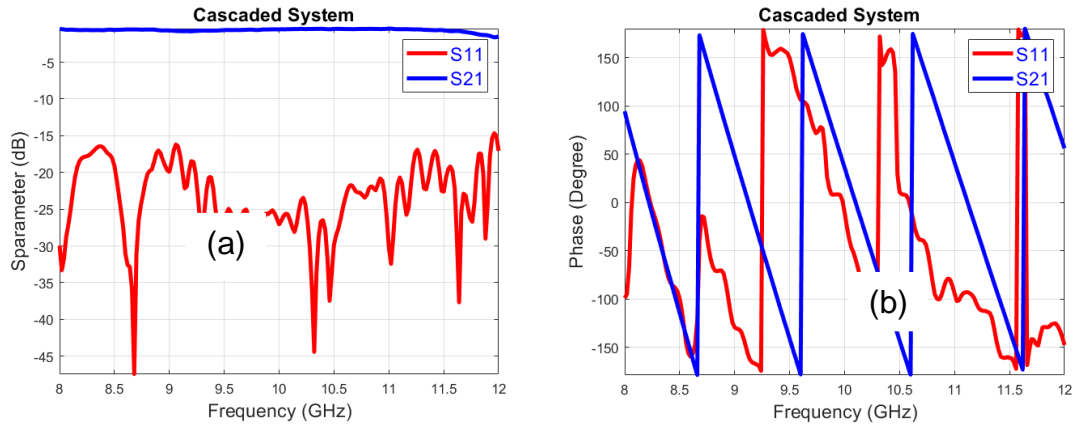
49
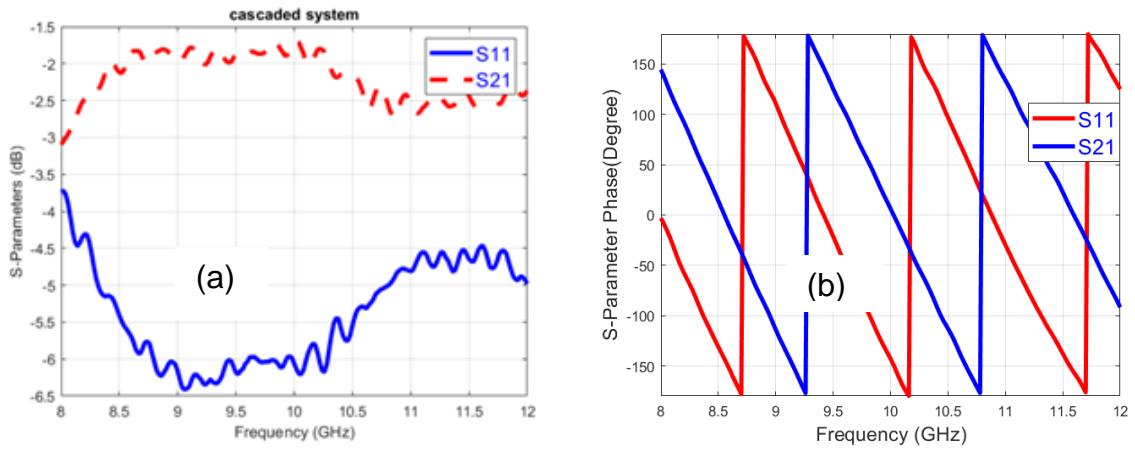
Figure 3.43. S-Parameters of cascaded system. (a) S-Parameters magnitude in dB.
(b) Phase in degree.
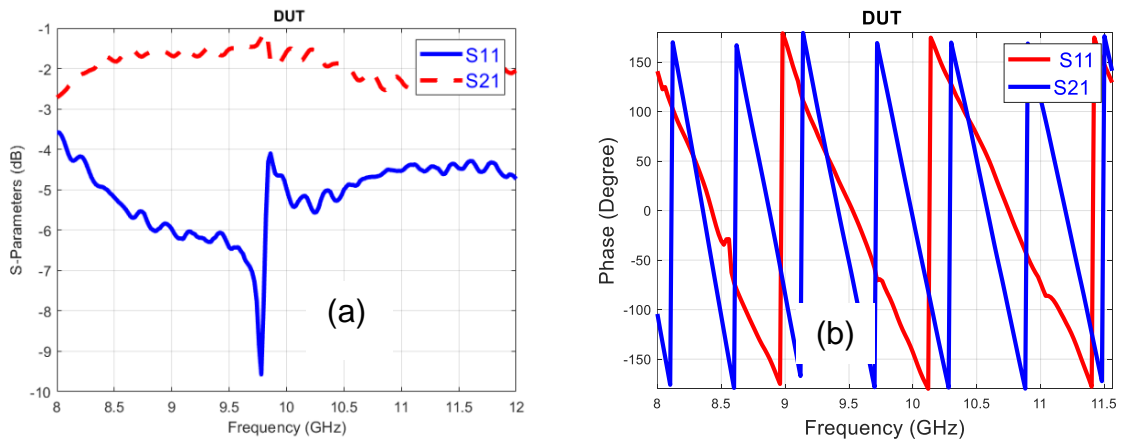
Figure 3.44. S-Parameters of FR4. (a) S-Parameters magnitude in dB. (b) Phase in degree.
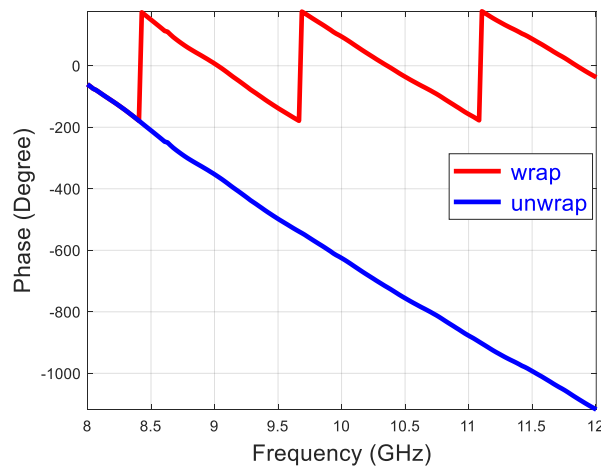
Figure 3.45. Transmission phase wrapping and unwrapping.
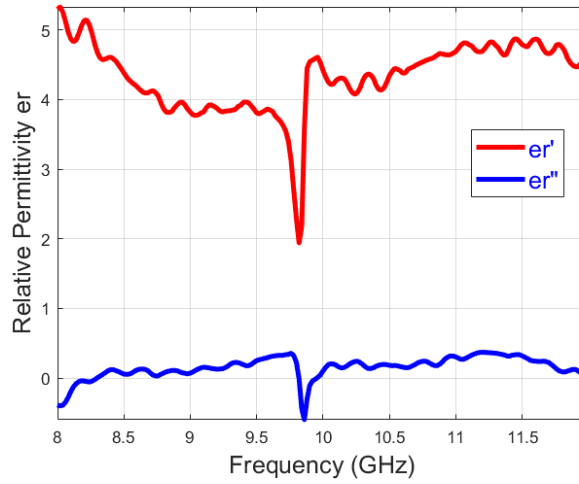
Figure 3.46. The relative permittivity of FR4.
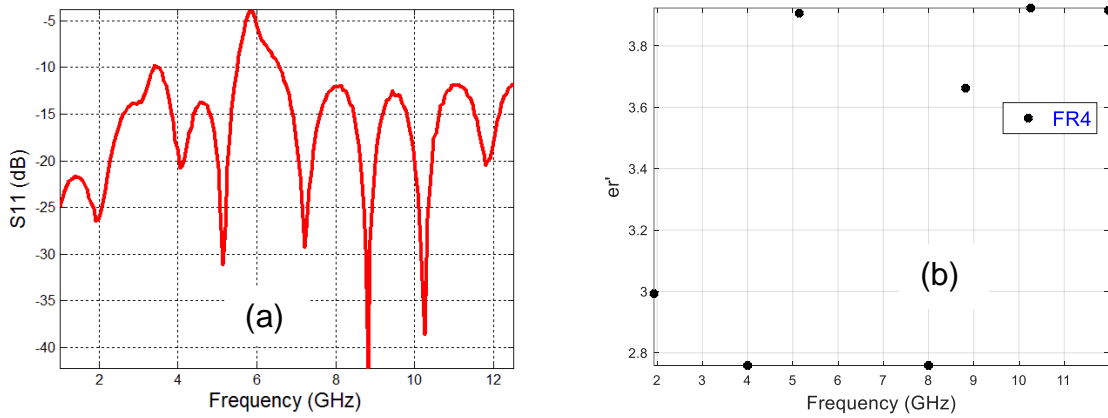
Figure 3.47. (a) S11-Parameter of the microstrip line on the FR4 substrate. (b) Dielectric constant of FR4 using the transmission line method.
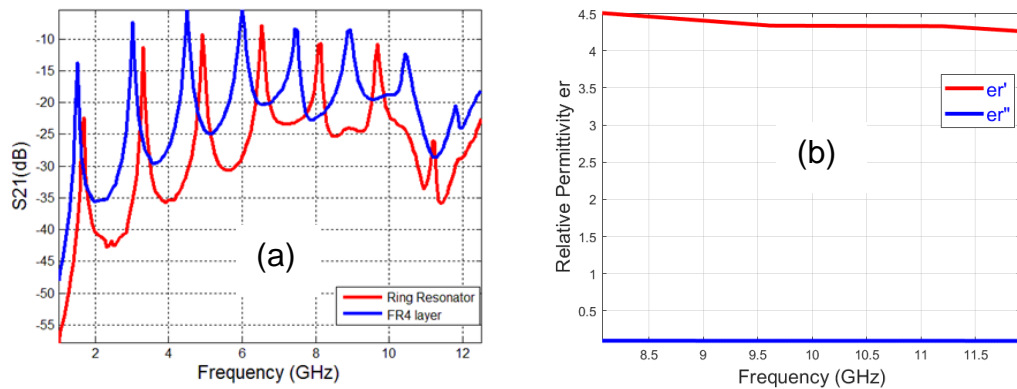
Figure 3.48. (a) S21-Parameters of the modified ring resonator with FR4 material. (b) The relative permittivity of FR4.

51
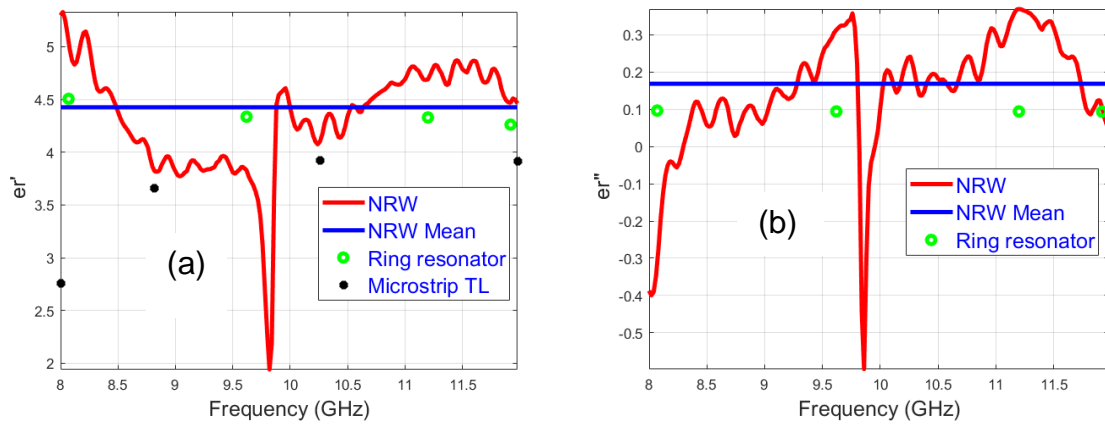
Figure 3.49.Comparison of relative permittivity of FR4. (a) Dielectric constant. (b) Loss factor .

Figure 3.49 depicts the comparison of FR4 substrate measured through the waveguide, modified ring resonator, and microstrip transmission line for X-frequency band. The dielectric constant and loss factor measured through the waveguide method are $\varepsilon'_r = 4.48$ and $\varepsilon''_r = 0.15$. Using the modified ring resonator, the dielectric constant and loss factor are obtained as 4.45 and 0.094 respectively.

In the end, an overall comparison of measured results for all the material with the data available in the literature is presented in table 3.3.

Table 3.3 Comparison of the dielectric constant of the material at X-Band

Techniques		Cotton	Jeans	PDMS	Ak-Sil T1310	FR4
Waveguide	ε'_r	1.68	1.65	2.84	2.67	4.48
	ε''_r	0.038	0.001	0.079	0.04	0.15
Modified Ring Resonator	ε'_r	1.78	1.68	2.8	2.7	4.45
	ε''_r	0.02	0.014	0.05	0.05	0.09
Microstrip Line	ε'_r	1.7	X	X	X	3.56
	ε''_r	x	X	X	X	X
Value in literature	ε'_r	1.6 [62]	1.6 [62]	2.3-2.8 [63]	2.8 [64]	4.4 [65]

3.4. Investigation of Fabrication Techniques and Conducting Materials

The fabrication of electronic circuits on the textile and flexible material is a difficult task. The metallization of these substrates is the main challenging issue. The performance of design mainly depends upon the type of conductive material and the method of metallization. As both factors are linked, a thorough investigation of their collective performance is required. Following are the electric circuit fabrication techniques on a flexible substrate.

3.4.1. Screen printing

This is the most versatile flexible circuit fabrication process [66-67]. It is based on the conventional silk screen printing process where a screen is developed having design patterns to be drawn on the film. The printer pushes the conductive ink through the screen openings onto the substrate and after drying, the circuit is finalized. The screens used for the electronic printing applications are made from silk and the required print is transferred onto the screen using a special coating which has extremely fine edge resolution. Screen printing is known to produce designs with 50 microns of width or gaps [18], [68-69]. Figure 3.50 shown below explains the entire process of screen printing.
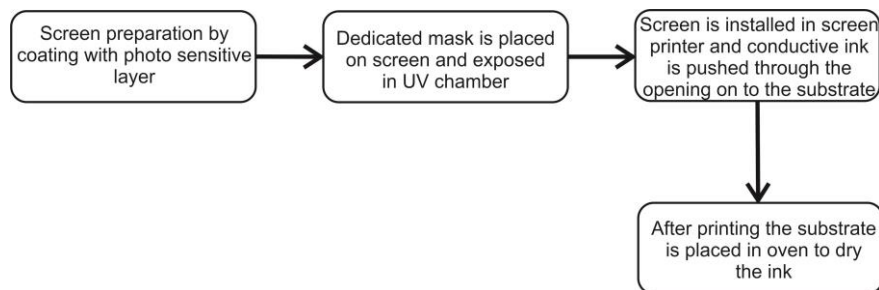
Figure 3.50. Screen printing of flexible RF components.

3.4.2. Photolithography through photo-imageable inks.

The most recent technique which is popular in making flexible circuits is through photo-imageable inks [70]. These are special conductive inks that are light sensitive. The ink is coated onto the substrate using a screen printer with a uniform coat of 10 to 20 microns. Once dried in a controlled light environment the special mask is prepared which resembles the one used for the chemical etching process. The mask aligned on a coated substrate is placed in an ultra violet exposure unit. The portions which are exposed to the light undergo a chemical reaction and get hardened. The other unexposed sections are

53

removed through a chemical process in the development phase. This process is known to produce extremely fine features of 20 microns with high edge resolution [71] and is widely adopted for flexible circuit fabrication [72]. However, the consumables and photo-imageable inks used in this process are very expensive and have a limited shelf life. The process is also popular in the bulk production phase. The complete process is summarized in the flow chart given in Figure 3.51.
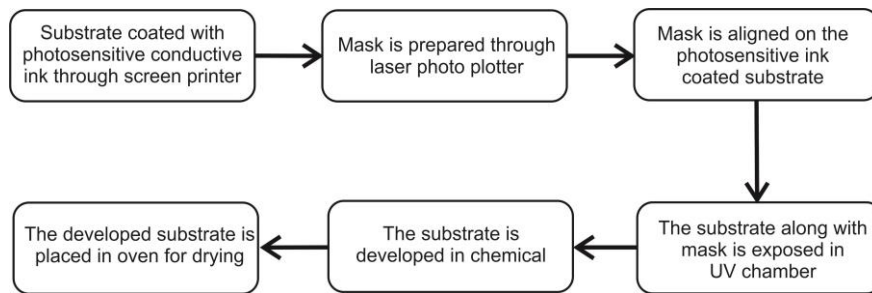
Figure 3.51. Photo-imageable ink printing technique of flexible RF components.

3.4.3. Ink jet printing

A recently developed technique of ink jet printing is gaining popularity due to its straightforward usage and cost-effectiveness [73 -75]. It is based on conventional ink jet printing technique where ink droplets are sprayed in a specific pattern to develop the design. The conventional ink is replaced with conductive ink which is developed with a special recipe. Once the conductive pattern is printed on the substrate it is cured at a high temperature around 150° C to dry the ink. In this phase, the vehicles and other organic solvents evaporate leaving behind the conductive dry pattern [76].

3.4.4. Stitching, Sewing and Computerized Embroidery

The stitching/sewing and computerized embroidery are also very promising fabrication techniques to draw the electric circuit on a textile substrate. Initially, conductive textiles are developed for electromagnetic shielding purposes. Due to surface tension, the conductive wires were not suitable for circuit fabrication. With the recent development of silver and gold-coated conductive yarns and fibers, open a door to use these yarn/fibers to design electric circuits on textiles moreover the computerized embroidery also made it easy to design complicated circuits.

A brief overview of widely used fabrication techniques for the flexible substrate is presented above. In this thesis, textile is shortlisted for the substrate. In the next section performances of different fabrication techniques are investigated.

3.5. Fabrication Techniques for Textile Substrate

The standard fabrication techniques for fabricating electric circuits on the textile substrate include inkjet printing, screen printing, stitching, and sewing. In this research, we have investigated the performance of screen printing, PVD, and stitching techniques. The screen printing and PVD techniques use conductive ink for metallization, whereas the stitching technique requires conductive threads.

3.5.1. Stitching, Sewing, Sticking

To check the performance of each technique, a Frequency Selective Surface (FSS) unit cell for X-band is designed, and its frequency behavior is investigated through the waveguide method. The Computer Simulation Tool (CST) is used for simulation purposes. The two textile materials, one is a regular jeans, and the other is DuPont's Tyvek fabric which is mainly used to prepare personal protection kits is used as a substrate. In simulation Perfect Electric Conductor (PEC) is used. The simulated design and waveguide setup are shown in Figure 3.52.
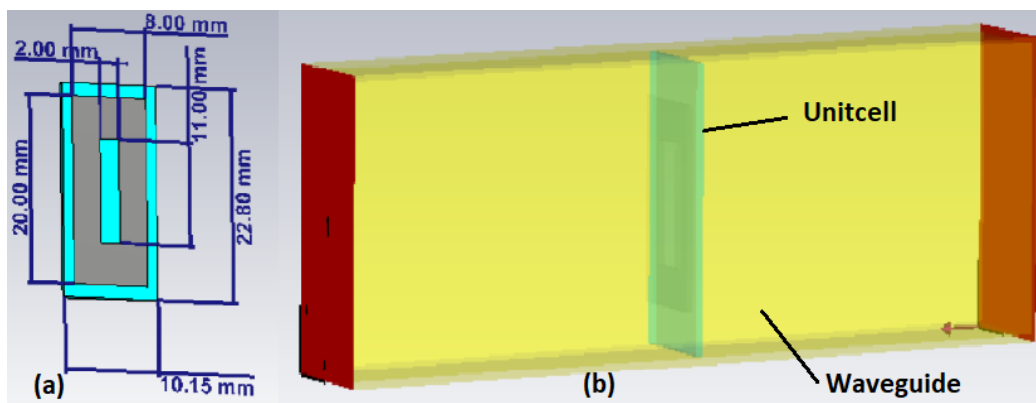
Figure 3.52. (a) Unit cell design. (b) Simulated waveguide setup.

The measurement setup and fabricated design through sticking and stitching are shown in Figure 3.53. Three different types of conducting materials sticky copper tape, conductive textile, and copper thread are used. The measured and simulated S-parameters are shown in Figure 3.54.
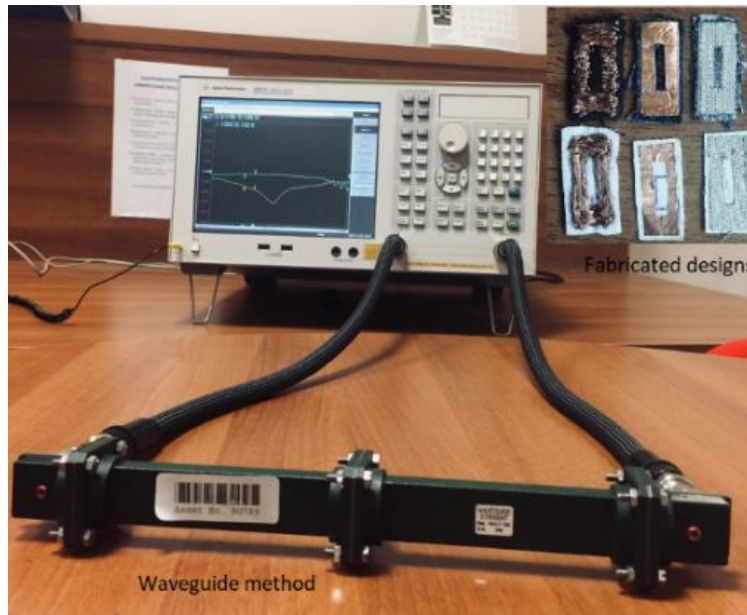
Figure 3.53. Measurement setup and fabricated design
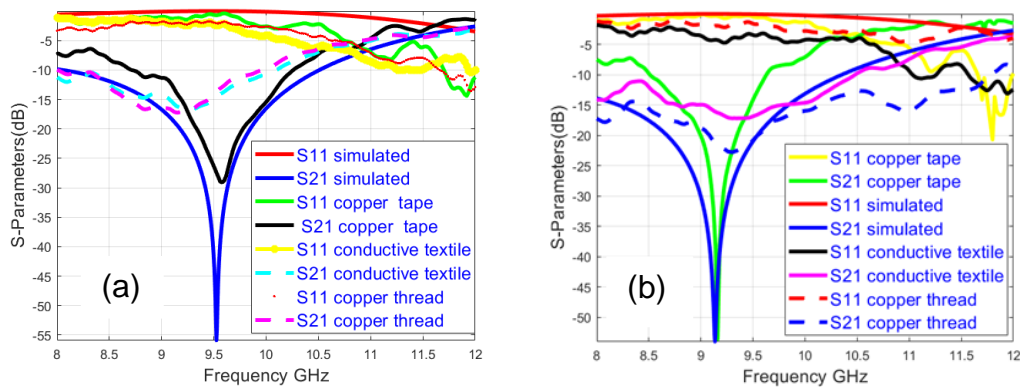
Figure 3.54. (a) FSS unit cell simulated and measured results for the jeans substrate. (b) FSS unit cell simulated and measured results.

Figure 3.54 (a) is about the simulated and fabricated results for the FSS unit cell on jeans substrate with investigated conductive materials, while Figure 3.54 (b) represents simulated and measured results of the FSS unit cell on Tyvek substrate. It can be observed that results for Tyvek material have frequency resonance more resembled simulated design than the jeans material. It is because in Tyvek thread or very closely packed very tightly compressed, there are no air gaps between them. Whereas, in jeans, there are some air gaps in between threads. In the simulation, we used a flat and smooth PEC, which is more like copper tape, the Figure 3.54 shows that the copper tape has shown results nearer to the simulated one than conductive thread and textile. The samples with conductive

56

thread and textiles have rough surfaces. Moreover, the diameter and density of threads are also the critical factors affecting the performance of the design.

3.5.2. Physical Vapor Deposition Technique

The Physical-Vapor-deposition (PVD) technique is only implemented on Tyvek textile because jeans and regular cotton materials are incompatible with the deposition process. The PVD techniques show deplorable behavior almost all the incident waves transmitted through it. Moreover, for PVD techniques the conductor layer start peeling off with time. The fabricated design and results are presented in the Figure 3.55 given below.
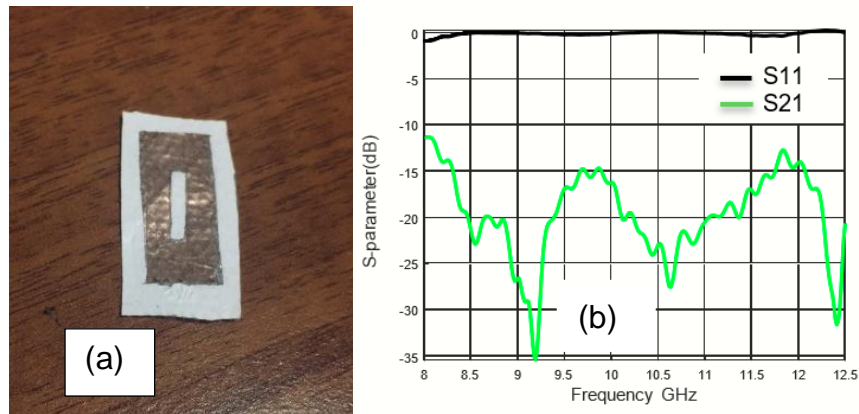
Figure 3.55: (a) Fabricated design. (b) Measured and simulated design

3.5.3. Screen Printing Technique

For screen printing, a split ring resonator design is used for the fabrication. The bare conductive paint is used to make conductive traces. The bare conductive shows inferior performance compared to simulated results and measure S11 and S21 parameters observed very near each other, as shown in Figure 3.56 (b).
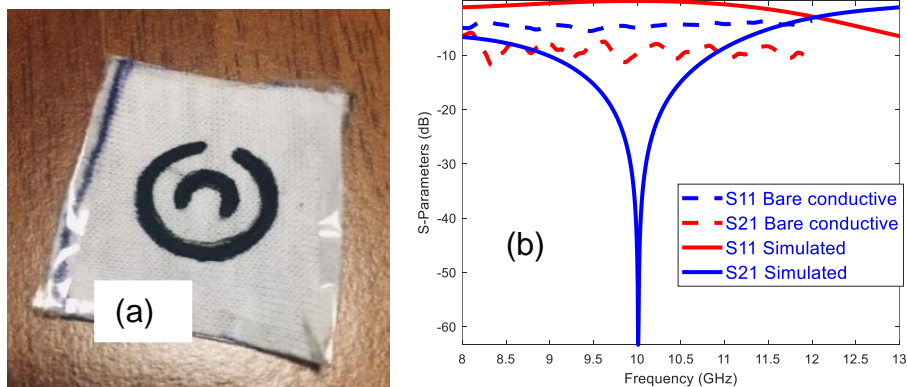
Figure 3.56: (a) SRR fabricated design. (b) Simulated and measured results

From the above results, it was concluded that the sticking, stitching/sewing fabrication technique has superior performance as compared to other techniques, due to this reason stitching/ sewing technique is chosen for design fabrication.

4. REFLECTARRAY ANTENNA THEORY

The satellite, radar, and long-distance communication could not be possible without high-gain antennas. Thanks to the reflector and array antennas, the desired high gain requirement can be achieved. The reflector antennas have a wide range of applications. Bulky and ridged parabolic antennas were initially used, but with the advent of time, those reflector antennas were swapped by reflectarray antennas. The concept of reflectarray antennas gained much more popularity in 1980, after developing low profile printed antennas. The reflectarray combines the advantages of a reflector and phased array antenna. Although parabolic reflectors provide high gain requirements significantly but have serious manufacturing and installation issues, and for high frequencies, these issues worsen more and more. Additionally, the reflectors are incapable of producing wide beam angle scanning.

On the other hand, a high gain phased array antenna can produce desired beam scanning but with the expense of additional complicated electronic equipment. Reflectarray mitigates these issues related to parabolic and array antennas. It behaves as a parabolic reflector in terms of spatial illumination and gain, whereas phase synthesis and beam collimation work as an antenna array. The reflectarray reflects incident wave when illuminated by a feed antenna; the radiating element of the array adjusts the phase of the reflected wave to focus the beam in a particular direction. The printed reflectarray antenna exploits the advantage of parabolic reflectors and phased array antennas. They are developed on plane substrates through modern printed circuit fabrication techniques and eliminate rigidity and bulkiness and provide higher efficiency. Their main drawback is their narrow-bandwidth characteristic. This problem becomes more severe for reflectarray having a thin substrate, scientists continually exploring different methods to improve the bandwidth. The concepts of a parabolic reflector, phased array, and reflectarray are shown in Figure 4.1.

Figure 4.1. (a) represent the reflection of the incident field from a parabolic reflector. The incident wave has reflected the broadside due to spatial phase distribution on the aperture. Figure 4.1. (b) shows a collimated beam from a phased array antenna. The beam is directed in a specific direction; each element of the array produces the required phase with the help of a phase shifter attached at the back end of the array. Figure 4.1. (c) represents the reflectarray. The beam yields in a broadside direction in a planar antenna

array due to uniform phase distribution on the aperture. The progressive phase distribution is required to focus a beam in a specific direction.
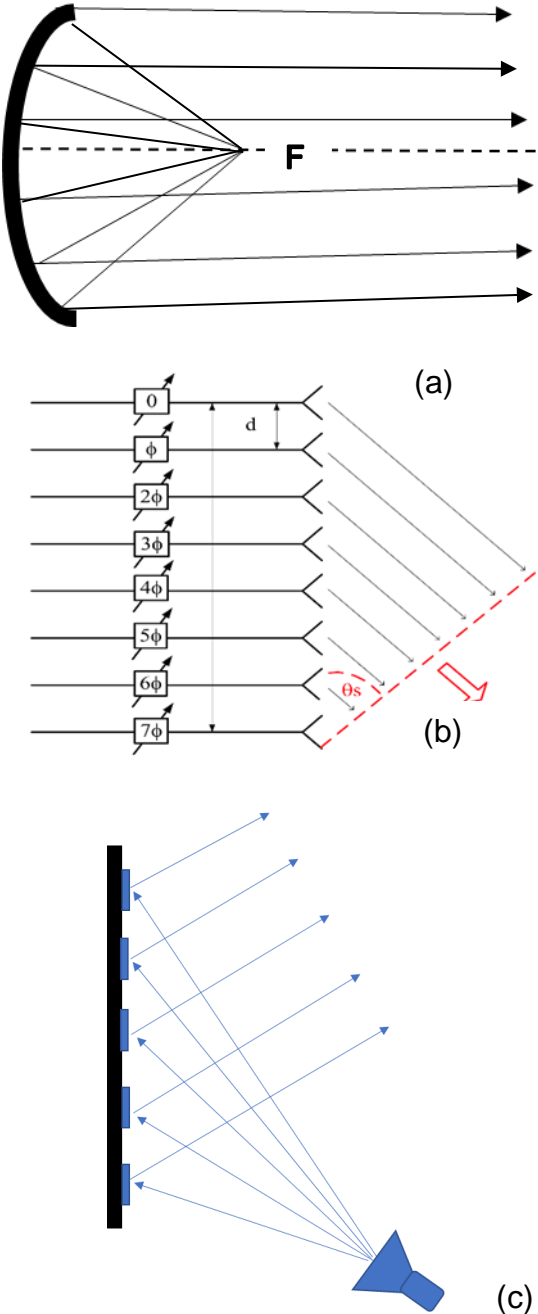
Figure 4.1. (a) Parabolic reflector. (b) Phased array antenna. (c) Reflectarray

4.1. Early History of Reflectarray

Berry, Malech, and Kennedy developed the array of short-ended variable-length waveguides illuminated by a horn antenna in early 1960 to realize a collimated far-field beam is considered the first reflectarray [77]. The basic principle was to collimate the

beam in the far-field region by controlling each waveguide element's length. The design consisted of bulky waveguides arrays and heavy antennas. After its invention, the waveguide-based reflectarray quickly became obsolete within ten years, and no further efforts were made to optimize it.
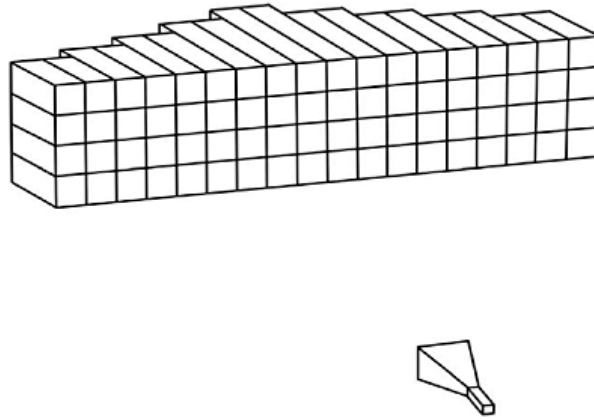
Figure 4.2. Waveguide reflectarray concept.

The next major development in reflectarray was made in the 1970s when Phelan invented a spiral-phase reflectarray. The spiral-phase array consisted of four-arm spiral or cross dipole elements connected with a switching diode. The spiral/cross dipole elements used to produce co-phrasal beam at far-field while switching diodes made wide-angle beam scanning possible by activating and deactivating arms of factors [78]. After that, no significant development was observed in the reflectarray area until the emergence of printed microstrip antennas in the 1980s. Malagisi pioneered microstrip reflectarray, and he developed the first microstrip radiating patch-based reflectarray [79]. Later that year, Montgomery used the infinite ground plane technique to analyze reflectarray elements [80]. Later, many researchers started investigating the microstrip reflectarray. Their main focus was to reduce the size and mass of the antenna array, mainly using differential-length phase delay lines to produce the desired beam at the far-field [81-86]. Continued progress was observed in a reflectarray field later.

A printed dipole reflectarray was presented in [87]. The author used elements with different dipole lengths to get the required phase characteristics. In [88], elements with variable patch sizes are used for phase tuning, opening a window to use the Method of Moments technique to design and analyze reflectarray [89-90]. A more improved approach is presented based on the physical rotation element and keeping stub length and element size fixed to improve sidelobe and cross-polarization performance [91-92]. Along with the reflectarray patch shape, size, and phase compensation technique

researcher also investigates feeding methods to improve the performance of a reflectarray. To mitigate feed blockage, an offset feed configuration is used by the authors in [93]. An offset feed configuration was used to feed printed dipole reflectarray with variable length dipole elements used for frequency scanned grating reflector antenna [94]. Moreover, devices operating at higher frequencies urge scientists and researchers to develop reflectarray on higher frequencies as well. An X band two-layer reflectarray with Minkowski element is investigated in [95] a reflectarray with 3 ferrite phases shifters operating at 35 GHz is reported in [96] whereas, A reflectarray operating on 94 GHz fabricated on a single waffle equipped with a one-bit PIN diode to achieve wide-angle beam scanning is presented in [97]

4.2. Recent Trends

Technology is transforming very rapidly, which also opens a new horizon for research and development. For example, with the advancement of fabrication technologies, the multilayer reflectarray also draws wide attention [98]. On the one hand, sophisticated electronic devices encouraging electronic beam scanning based reflectarray are gaining attraction [99]. On the other hand, progress in micro-electro-mechanical systems adds a new dimension to current reflectarray research trends [100].

 The substrate is an integral part of any RF and microwave circuit. A lot of research is available on the use of different types of substrates in reflectarray design. The conventional substrate material used for reflectarray is ridged, inflexible, and hard, for example, FR4 and substrates from Rogers corporation [101-102]. In [103] authors used organic material as a substrate for reflectarray. In [104] H. I. Malik and coauthors use a paper-based material to analyze the reflection phase of the reflectarray antenna. A reflectarray was developed through 3D printing material in [105]. In that research 3D reflectarray was created, the phase was tuned by adjusting the height of each unit cell. The increasing application of reflectarray in different interdisciplinary areas required conformal reflectarray instead of planer ones. These arrays are designed according to the object's surface geometry where the antenna is installed [106]. The invention of thin-film and membrane revolutionized the reflectarray antennas for space applications. The new thin, lightweight, and easy-to-install antennas are an alternative to heavy, bulky conventional space antennas. Below are some examples of thin membrane reflectarray for satellite and space communication [107-110]. These antennas are mainly developed on thin films like Kapton. A less explored but potential alternative of thin membrane

reflectarray having the advantage of low cost and ease of fabrication is textile reflectarray. In recent years' textile substrate for antennas has gained wide popularity. Most textile-based antennas are developed for biomedical applications or on-body communication. The textile-based reflectarray is a relatively new topic for research. Ahmed A. Kishk and co-researchers do the only work in this domain. They have practically investigated different possible unit cells on a textile substrate in [111], flexible and portable reflectarray in [112], and linearly polarized reflectarray in [113], respectively. All the mentioned research is for C-band.

In this dissertation, X-band textile reflectarray with both center and offset configurations are implemented.
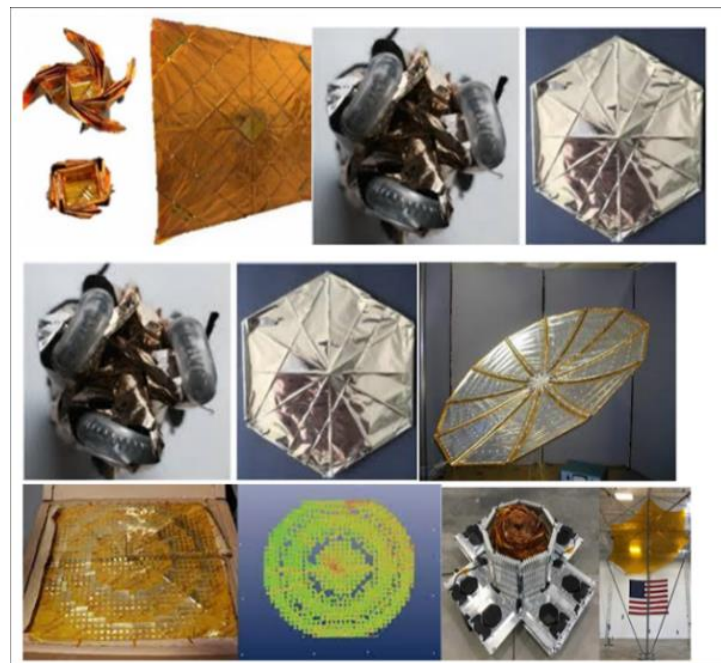
Figure 4.3. Examples of deployable, flexible space antennas [107-110].

Designing a reflectarray antenna generally requires the following steps

- Designing a unit cell to get the desired phase range

- Designing array with suitable size and number of elements

- Designing and placement of feed antenna

The unit cell serves as a building block of reflectarray. The progressive phase distribution, phase range, efficiency, and overall radiation pattern of reflectarray mainly depend upon unit cell attributes. The return loss and radiation pattern mainly depend upon radiating patch geometry, while different phase tuning techniques characterize phase

range. The following two steps, which involve array and feed designing, can also be termed the system design. The system design mainly deals with a gain requirement, aperture efficiency, and directivity.

The most crucial step in designing a reflectarray is the accurate characterization of patch elements. The characterization of the element includes phase distribution with respect to the given geometry and the effect of each polarization field. The techniques used to characterize reflectarray elements include circuit models [114], and computer simulation tools [115-116]. First, phase curves of the unit cell for geometric parameters are obtained, and then radiation characteristics for co and cross-polarization are obtained.

Different techniques are used to obtain phase curves of the unit cell. The simplest method is based on the concept that the phase response of a unit cell is independent of the angle of incidence of the incident wave. This assumption is valid for central fed reflectarray with normal incidence having a larger F/D ratio. As most of the incident wave is reflected back from the central part of reflectarray, it is assumed that the central element of reflectarray with a very large F/D ratio is considered to have a minimum phase difference. Assumption of normal incidence can provide a good estimation. The technique is unsuitable for the elements on the edges or has larger incident phase differences [117]. Moreover, the technique mentioned above does not work for offset configuration because the offset configuration angle of the incident must be considered in the analysis.

The other important parameters which must be analyzed during unit cell analysis are cross-polarization level and mutual coupling. The technique mentioned above based on the independence of phase distribution on incident angle does not work for cross-polarization level prediction. The computation of cross-polarization requires both parallel and perpendicular components of the incident wave. The incident wave impinging on the reflectarray element with a certain angle (θ, φ) has two orthogonal components. It produces a reflected wave with two orthogonal components that can be computed using a full-wave analysis method.

The reflected wave from a reflectarray is the combination of the reflected field from the patch element and the ground plane. If the ground plane's effect is ignored or not considered during analysis, completely different phase curves will be obtained [118].

The analysis of reflectarray can be done by considering each element in isolation or in an array environment. The analysis assumes that the unit cell in isolation mode does not

account for mutual coupling between neighboring elements and is mainly applied on reflectarray elements with stubs for phase tuning [119]. To implement this technique for analysis of reflectarray having a variable patch method for phase compensation, the distance between edges of two neighboring elements must be larger than $0.25\lambda_g$ (here λ_g is the wavelength in dielectric material); otherwise, this technique is not applicable. A severe issue of grating lobe rises for the inter-element distance greater than $0.25\lambda_g$, and sometimes this distance must be smaller than $0.25\ \lambda_g$ to obtain correct phase characteristics [120- 121]. The effect of mutual coupling is more prominent for the reflectarray, which uses a variable patch method for phase compensation as the difference between each element changes with patch size.

The effect of mutual coupling can be analyzed by using the Finite Difference Time Domain (FDTD) analysis technique as presented in [122]. This technique considers a unit cell in an environment of neighboring elements and estimates reflected wave from it. The process is applied to each array element, which requires a lot of computation time for a large reflectarray. This problem is solved by using Floquet's theorem. This technique considers a unit cell in a periodic environment to estimate the phase difference and then predicts the result for the array by taking mutual coupling into account [123-124].

The full-wave analysis of a periodic structure can be done by using a different numerical model. The choice of these models depends upon many factors, including the domain of computation, mathematical model (integral, differential), computational speed and cost, and type of geometry. The MoM operates in the frequency domain and uses a mathematical model based on the integral equation [125]. The Finite Element Method (FEM) [126], and Finite Difference Time Domain Method (FDTD) [127] use the differential equation for computation. There are some other techniques like Geometric Optics, and hybrid of FEM and Generalized Scattering Matrix [128], Sparse Matrix Canonical Grid (SMCG) method, and Characteristics Basic Function (CBF). The analysis in the time domain has the advantage of a wide frequency band of computation but also suffers from more CPU time consumption. Many simulation tools based on these numerical computational methods are available in the market. The most widely used tool for full-wave analysis of reflectarray includes HFSS Ansys, CST, and FEKO.

4.3. Reflectarray Analysis Techniques

The design and analysis of reflectarray is a complicated process for two reasons. The first reason is the large number of elements that make conducting a complete array analysis challenging. The other reason is to account for mutual coupling between array elements. The effect of mutual coupling becomes more challenging if the distance between two elements is lesser than half of the wavelength in the medium. These complications are solved by considering reflectarray as an infinite array [120-122]. In an infinite array approach, all the elements other than those located at the edge of an array are considered similar behavior because they are not suspected of edge variation. This consideration makes it easy to analyze the single array element in a periodic environment by assuming all the surrounding features identical. In an actual situation, a reflectarray is not a regular structure but a quasi-periodic instead, as their elements are not similar. However, in most cases, this periodic consideration works adequately for reflectarray analysis.

Following are the main techniques to analyze a periodic structure

- Waveguide technique

- Circuit model technique

- Floquet port technique

4.3.1. Waveguide Technique

In the waveguide technique, the element is placed inside a waveguide and then exited through a normal incident plane wave with the help of a waveguide port. This technique replicates an infinite array scenario based on image theory; all the four walls of the waveguide serve as periodic boundary conditions [129]. This technique accurately mimics the periodic structure analysis only for a normal incident plane wave. Generally, the normal incident provides a good prediction for center-feed reflectarray with a suitably large focal length and aperture size ratio (F/D). The dominant TE mode is used for excitation. In the case of a rectangular waveguide having $a > b$ the excitation mode will be dominant TE_{10}. Every waveguide has a certain excitation angle depending upon the dimension of the waveguide and can be calculated as.

$$\Psi = cos^{-1}\left(\left(\sqrt{1 - \left(\frac{\lambda}{2a}\right)^2}\right)\right) \qquad (4.1)$$

λ is the free space wavelength, a is the larger dimension of rectangular waveguide. A waveguide with different dimensions corresponding to that incident angle will be required to analyze the unit for different incident angles. The above factors limit the use of this technique. It is also important to note that the incident wave in a waveguide is not a uniform plane but can characterize the reflection properties correctly.
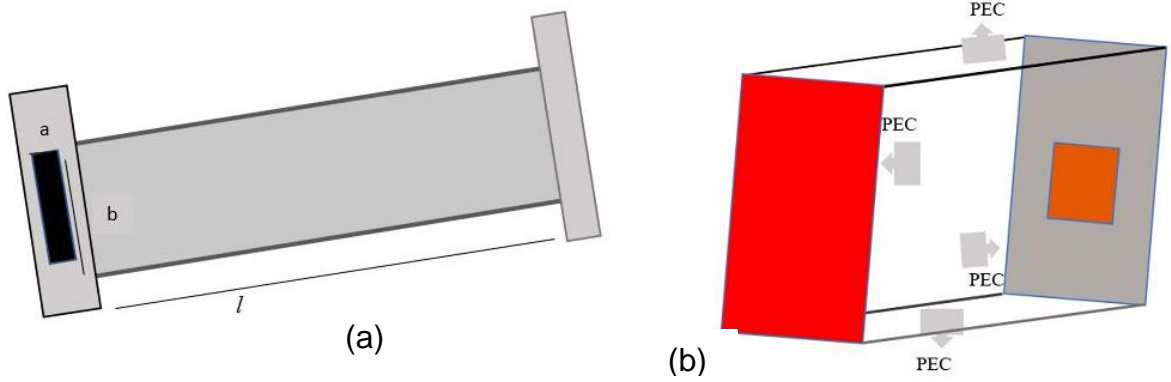
Figure 4.4. (a) Rectangular waveguide Model. (b) Boundary conditions for waveguide model.

4.3.2. Analytical Circuit Models

The circuit model technique is an analytical technique in which unit cells are analyzed using transmission line circuit theory [130]. Based on the geometry of the unit cell analogs circuit model is created. A complete unit cell can be considered as a parallel RLC circuit model. The conductive patches of two consecutive elements can be modeled as parallel capacitors, short-circuited ground of the unit cell can be regarded as a parallel inductor. In contrast, a dielectric loss can be taken as a parallel resistor. The desired parameter such as surface impended Z_s, and reflection coefficient Γ is then estimated from that circuit model.

$$\Gamma = \frac{Z_s - Z_0}{Z_s + Z_0} \tag{4.2}$$

The main problem with this technique is to develop the correct equivalent circuit model of the unit cell. The main advantage of this technique is to get a direct understanding of a unit cell operation; moreover, the circuit model technique can also be applicable to oblique incidence angle (θ, φ).
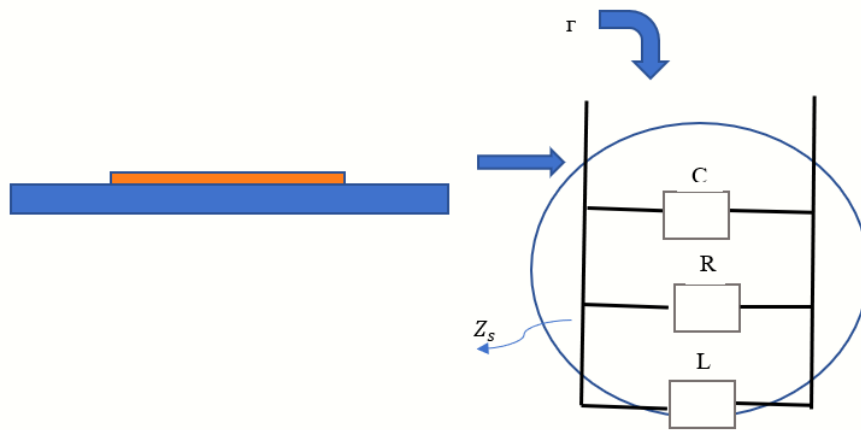
Figure 4.5. Circuit Model of unit cell

4.3.3. Floquet Port Technique

The waveguide technique is only applicable for normal incidence angles, but in reality, every element has a different incidence angle. As we move away from the center of the unit cell, the difference between normal and oblique incidence angles also increases correspondingly. For unit cell excited through a plane wave incidence through certain angles (θ_i, φ_i) and polarization (TE, TM) requires analyzing all the incidence angles. For oblique incidence, Floquet port or circuit model techniques are used [116]. In the Floquet port method, a rectangular box with the same cross-section dimension as that of the unit cell is created around the unit cell. The master and slave boundary conditions are assigned to the opposite sidewall of the box. This setup then excited from a top surface through a Floquet port situated at the distance $\frac{\lambda}{2}$ of the minimum frequency. The fundamental plane waves are generated by the set of Floquet modes which are excited by the Floquet port. These modes can produce any angle of incident or sense of polarization required for unit cell analysis. By default, two Floquet modes with indices $m = n = 0$, are present. These modes are named specular modes, have zero dB attenuation, and are considered as propagating modes. The other higher-order modes are taken as attenuating modes. The cutoff for higher-order modes depends upon the Floquet port scan angles. If the scan angle increases, some of these higher-order attenuating modes might become propagating modes.
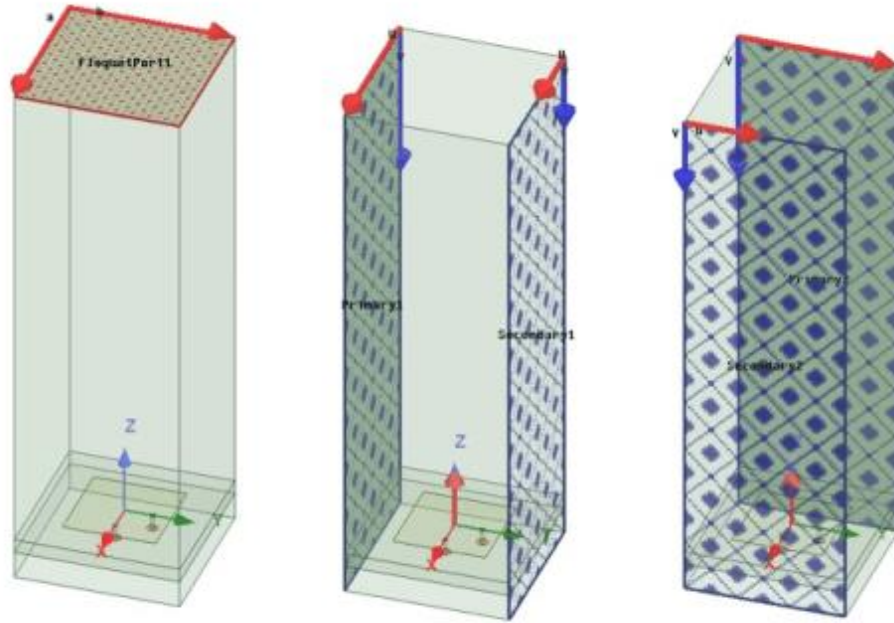
Figure 4.6. Floquet Port Model.

4.4. Phase Tuning Techniques

The choice of phase tuning method is the most critical step in the designing of a reflectarray. Once the tuning method is selected, then element characteristics and ultimately radiation characteristics can be realized easily. Following are general phase tuning techniques:

- Element with phase delay lines

- Element with variable size

- Element with a variable rotation angle

In the first technique, the phase shifting is achieved by using a delay line microwave network. It is also known as the guided wave technique [91], [131-132]. In the second method, the phase is controlled by changing the dimension of the element [88- 89], [133-134]. The last technique can be applied to the circularly polarized design and based on changing the element's orientation [132], [92]. These three techniques are presented in Figure 4.7 given below:
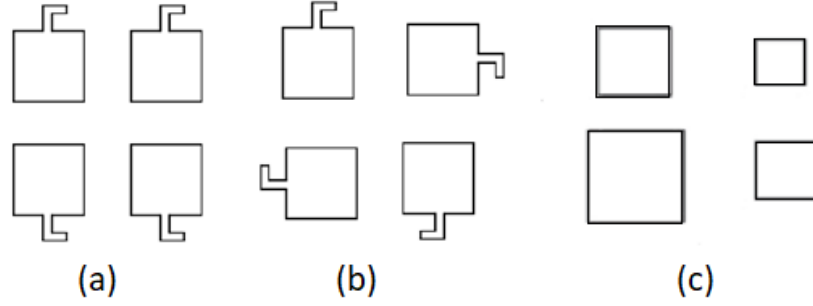
Figure 4.7. Phase tuning techniques. (a) phase delay line method, (b) element orientation rotation method (c) the variable size element method.

4.4.1. Element with Phase Delay Lines

In the phase delay line technique element, the radiating patch with an attached stub is used. The radiating patch receives an incident wave and if the stub characteristic impedance is matched with the patched then incident wave guides towards the attached stub with a specific wavelength. The stub might be terminated with an open or short configuration, the guided wave in the stub reflects back to the patch from these terminations. The radiating patch reradiates this reflected wave with a phase equal to double the stub length [135].

$$\varphi_{dl} = 2kl \qquad (4.3)$$

Where φ_{dl} is the phase shift of delay line configuration, l is the stub length, and k is the propagation constant along the stub.

The phase distribution on the aperture of reflectarray is controlled by changing the length of the stub/phase delay line. The difference of distance between two elements for the required phase difference is calculated as below.

$$\Delta l = \frac{\Delta \varphi_{dl}}{2k} \qquad (4.4)$$

In the ideal scenario, this technique produces a linear phase curve but has dissipative losses due to bends in the transmission line, transmission line impedance miss-match, and ground plane effect distort the phase resonance. The element with the phase delay line method is depicted in Figure 4.7 (a).

4.4.2. Variable Dimension Method

The physical dimension of reflectarray elements like width and length are changed to achieve the required phase variation. The resonant element dimension changes the resonant frequency, corresponding to a change in radiated phase at specific frequencies. The central concept is that two elements having different sizes would have a different phase. This method was first used for printed cross dipoles [133] and then letter-on used for rectangular patches [134]. The most conventionally adopted geometries are square or circular patches. The element with variable size method is shown in Figure 4.7 (c).

In this study, we aim to design a flexible printed reflectarray using a square patch geometry, and the variable dimension techniques are used for the phase tuning. A printed antenna is a highly resonated element with a significant quality factor; therefore, a small change can produce a wide range of phase variations in reflectarray. Ideally, a single resonance can provide a complete phase cycle of 360°. However, the total achieved phase range depends upon many factors, such as the separation between patches, substrate thickness, and the dielectric constant of the material used for the substrate. For substrate having a small thickness typically less than one-tenth of wavelength ($\frac{\lambda}{10}$) the tuning range above 300° can usually be achieved [132], which is sufficient for most reflectarray designs. The phase variation obtained using element size variation is highly nonlinear because of the high Q resonant nature of printed antennas with a thin substrate. This results in rapid phase variation near resonance and slow variation at the extreme corners [136].

In the next section, the proposed design and the effect of different physical parameters of reflectarray antennas such as patch length, substrate height, the incident angle of wave illuminating reflectarray are explained thoroughly.

4.4.3. Element Rotation Method

In elements with variable rotation angles, the element is physically rotated around the axis. The rotation of the antenna element around the axis with a specific angle φ^o reflects the incident field with the same angle. The phase distribution on aperture is controlled by rotating the neighboring element with a certain angle, whereas phase lead and lag are determined from rotation's direction [137]. This technique is only applicable for circular polarization cases. The element with variable rotation angle is shown in Figure 4.7 (b).

4.5.   The Bandwidth of the Reflectarray Antenna

Reflectarray array antenna combines high gain rigid reflector and low cost, lightweight microstrip antenna array. This hybrid configuration brings many advantages such as high gain, low cost, low profile, and mass. On the other hand, it has inherent major bandwidth limitations. The reflectarray antennas serve as a good alternative to the reflector, but both have significant differences regarding bandwidth performance. A reflector is considered a frequency-independent antenna with infinite bandwidth, and its bandwidth depends upon the bandwidth limitation of the feed antenna. At the same time, a reflectarray has a narrowband frequency behavior. The patch element, aperture of antenna, focal length, and bandwidth limitation of feed antenna are the prime factors limiting a reflectarray bandwidth performance and typically do not go beyond 10%.

The patch element of a reflectarray is used to be designed according to a certain frequency requirement. These patch elements are responsible for producing the required phase distribution on the aperture of an antenna to get a collimated beam in the desired direction for that particular frequency. Any change in operational frequency results in phase error which results in pattern deterioration, gain reduction, and bandwidth limitation. The phasing element must compensate for phase error results due to frequency change to operate efficiently on a new frequency.

The phase difference between the central element and an arbitrary element at the central frequency f_0 can be computed as follow:

$$\psi_2(f_0) - \psi_1(f_0) = k_0(R_2 - R_1) \tag{4.5}$$

When operational frequency changes from f_0 to f_1, the equation become

$$\psi_2(f_1) - \psi_1(f_1) = k_1(R_2 - R_1) \tag{4.6}$$

From the above equations, it can be noted that the phase difference also changes when the frequency changes, resulting in phase error.

$$PhaseError(f) = \psi_2(f_1) - \psi_1(f_1) - k_1(R_2 - R_1) \tag{4.7}$$

The equation consists of two terms one is frequency behavior, and the other is required phase delay. The phase difference increases as frequency increases, and the phase difference decreases with a decrease in frequency. It can also be deduced from the equation that a minor phase difference corresponds to a broader bandwidth.

4.5.1. Single-layer and Multi-layer Reflectarray

The phase range and bandwidth of the reflectarray element are interdependent and depend upon the substrate thickness. If substrate thickness increases, the phase curves transition becomes more linear; consequently, bandwidth improves; however, the phase range decreases. The substrate with a thickness smaller than $\frac{1}{10}$ of wavelength in the material can yield a maximum phase range around 360°. To get the optimized performance of reflectarray, substrate thickness has to be chosen very carefully.

More than one layer of substrates can be stacked to get a more comprehensive phase range, smother, and more linear variation of phase response [138-139]. These stacked layers can be of the same substrate materials having radiating patches on them or of different materials with and without radiating patches. The multilayer structure with radiating patches can produce a phase range of several times 360°. The multilayer structure with varying substrate materials produce more linear phase response than a single layer by producing different reflection phases at the junction of the material layer. A multilayer reflectarray having two layers of same substrate separated through air produce 740° wide phase range is demonstrated in [138]. The multilayer configurations are shown in the figure below.
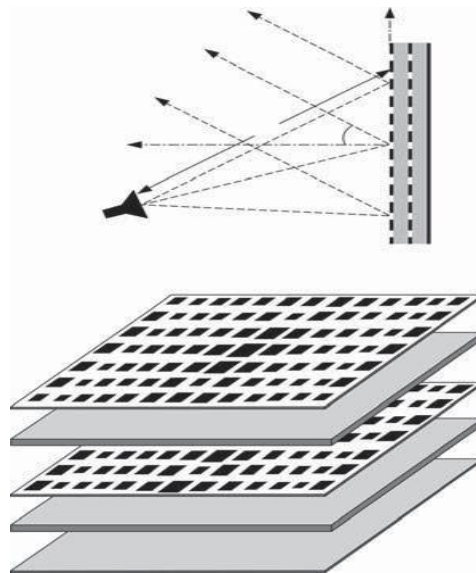
Figure 4.8. Example of multilayer reflectarray.

5. Design and Simulations

5.1. Unit Cell Design

5.1.1. Single Layer Unit Cell

This section presents the analysis and design of a square patch unit cell for X-band reflectarray antenna on the textile substrate. The element size variation technique is used for tuning the phase range of the reflectarray antenna. The two designs are investigated, the first one is single layer unit cell, and the other is a two-layer unit cell. The Floquet port method with master and slave boundary conditions is used to simulate the unit cell in HFSS. The jeans substrate having dielectric constant $\varepsilon_r = 1.65$ and loss tangent $tan\delta = 0.002$ is used for design simulation. As the periodicity of the unit cell contributes to both mutual coupling and grating lobes effects so the distance d between consecutive cells must fulfil $\frac{d}{\lambda_0} \leq \frac{1}{1+sin(\theta)}$ criteria, where θ is the incidence angle. Based on this criterion the optimized substrate dimensions are 17.1×17.1 mm whereas, the substrate thickness is 0.5 mm. The proposed square unit cell is shown in Figure 5.1.
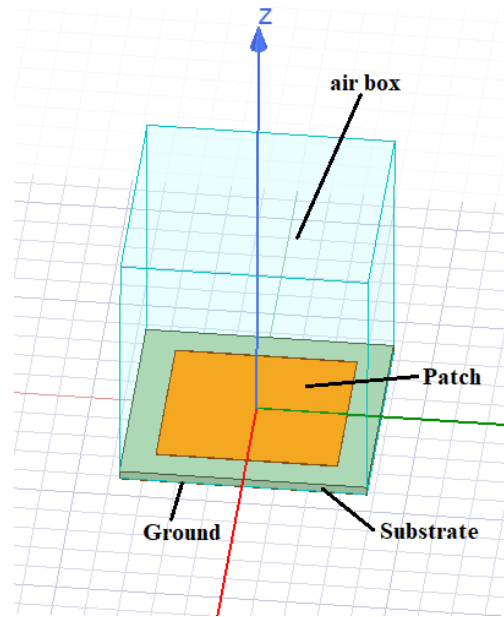
Figure 5.1. Unit cell.

The return loss and phase variation for 0.5 mm thick single layer textile unit cell on the whole frequency band for normal incidence is presented in Figure 5.2 given below. It can be observed from the figure that the phase variation resembles a typical S shape phase curve, where the phase varies rapidly and nonlinearly near resonance frequency (10 GHz). At the same time, varies slowly around the edges, which shows narrowband behavior of

radiating patch. The return loss curve shows that approximately -2.3 dB return loss is achieved at around 10 GHz center frequency.
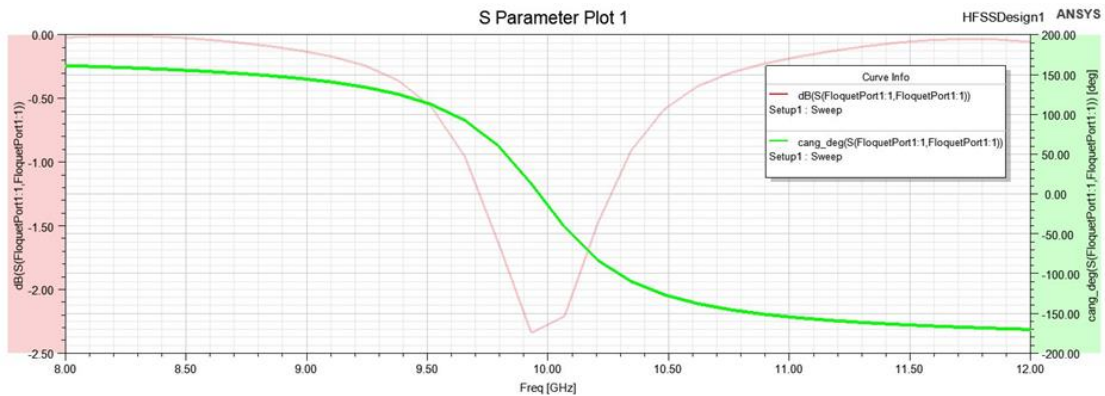
Figure 5.2. Return loss and phase variation along the X-band.

The above phase-frequency curve was obtained for the patch dimensions corresponding to 10 GHz resonance frequency. Change in element dimension also shifts the resonant frequency. The variation of patch dimensions significantly affects the phase range of the element, fabrication tolerance, and element bandwidth. The phase-length curve gives insight into fabrication tolerance and element bandwidth. The steeper phase-length curve is anticipated as higher sensitivity to fabrication error and narrow bandwidth. The effect of variation in the dimension of the proposed unit cell for different incident angles on phase range and return loss is shown in Figures 5.3-5.4.
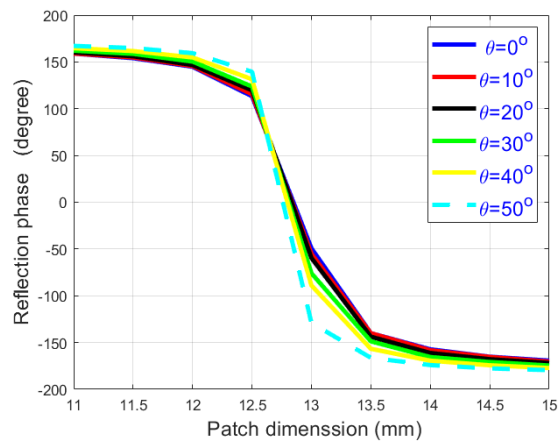
Figure 5.3. Phase variation of single layer unit cell ($\varphi=0^o$).
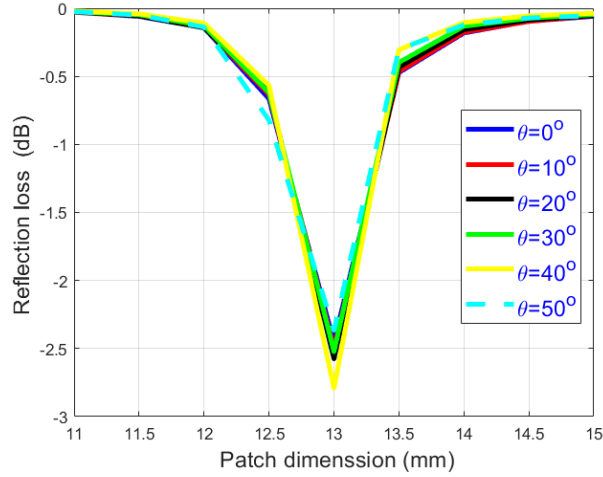
Figure 5.4. Reflection loss single layer unit cell ($\varphi=0^o$).

For a center feed reflectarray configuration, analyzing the phase curve only for the normal incident is sufficient mainly, but for offset configuration, the angle of the incident has substantial importance [84]. In [90, 139] the authors present a study for oblique excitation for rectangular patches with variable sizes. It was found that the phase difference between a normal incident and the oblique incident with 40° angle is 25°, and it goes to 50° for 60° incidence. Normally phase variation for design with a thin substrate is less susceptive to oblique incidence but still significantly impacts the magnitude of the reflected wave. In the above figures, the results are plotted for different incident angles by varying θ from 0° to 50° and keeping the φ at 0° degree. The phase curves in Figure 5.3-5.4 show that the phase range for the simulated square patch element is around 330° for one complete cycle. Usually, 360° phase variation is required for optimal performance, but the 300° degree phase variation is enough for satisfactory performance [132]. It can also be observed that the phase variation is very steep and highly nonlinear, which shows that the design is susceptible to fabrication error and a small error can cause a significant change in aperture phase distribution; moreover, element bandwidth is also very narrow. The return loss results show that the maximum return loss is around -3 dB. It is also observed that the highest phase variation is achieved for the elements with dimensions (12 mm-13 mm) around resonance, but the loss is also high for these elements. Figures 5.5-5.8 represent phase variation and return loss for the incident angle at $\varphi=30^o$ and $\varphi=90^o$ while varying $\theta=0^o$-50°.
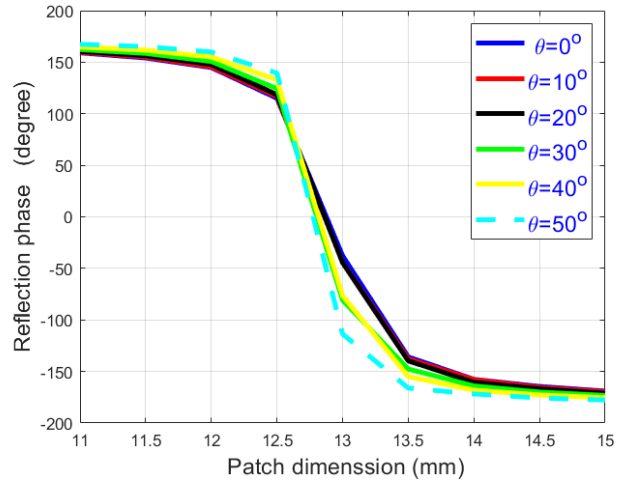
Figure 5.5. Phase variation of single layer unit cell (φ=30°).
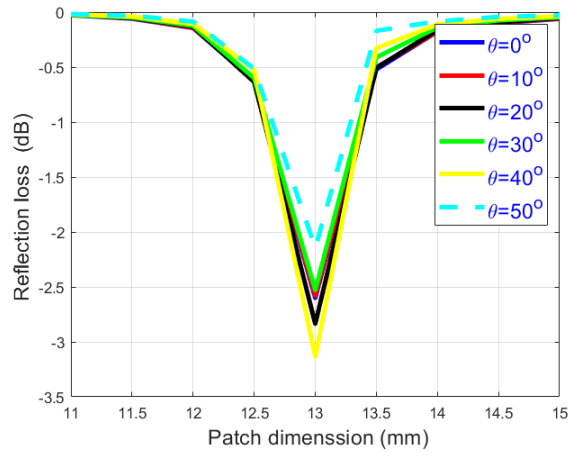
Figure 5.6. Reflection loss single layer unit cell (φ=30°).
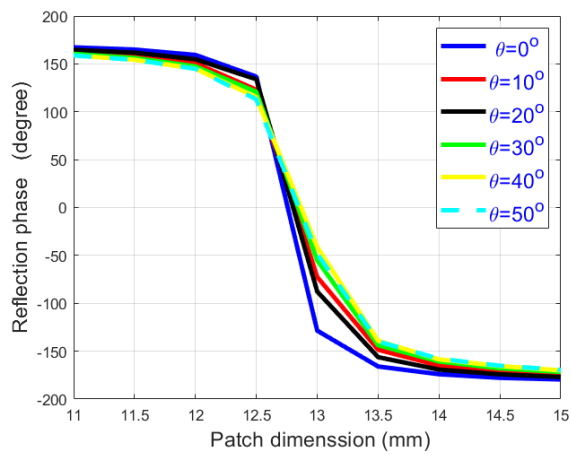
Figure 5.7. Phase variation of single layer unit cell (φ=90°).
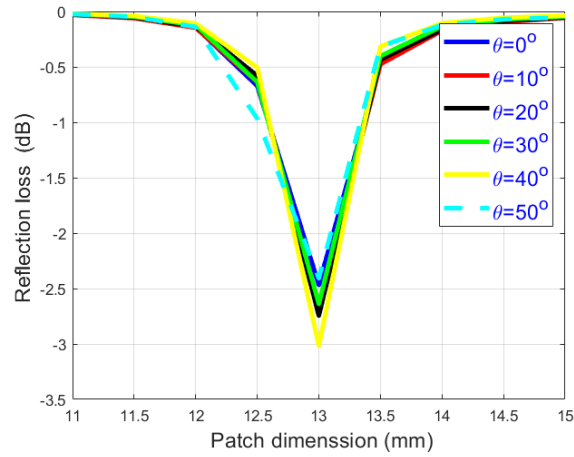
Figure 5.8. Reflection loss single layer unit cell (φ=90º).

In subsequent figures, the results are shown for different incident angles by keeping θ=30º,40º and varying φ from -45º to 45º.
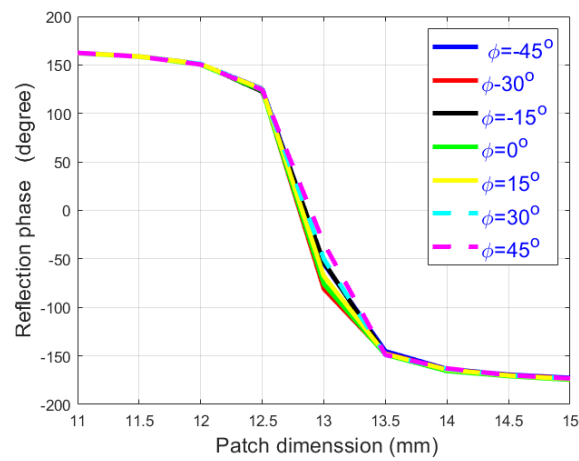
Figure 5.9. Phase variation of single layer unit cell (θ=30º).
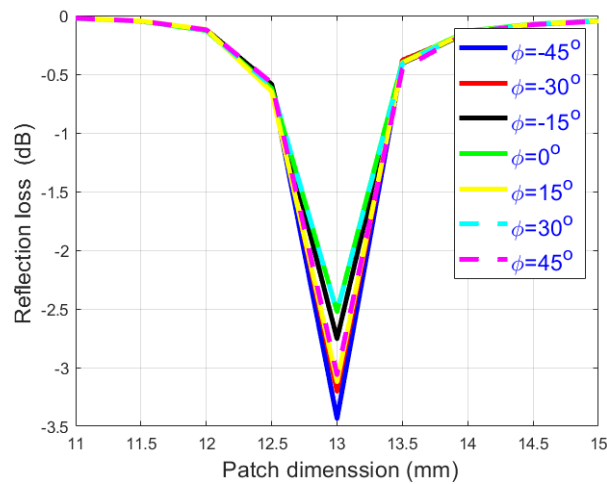
Figure 5.10. S11 parameter of single layer unit cell (θ=30º).
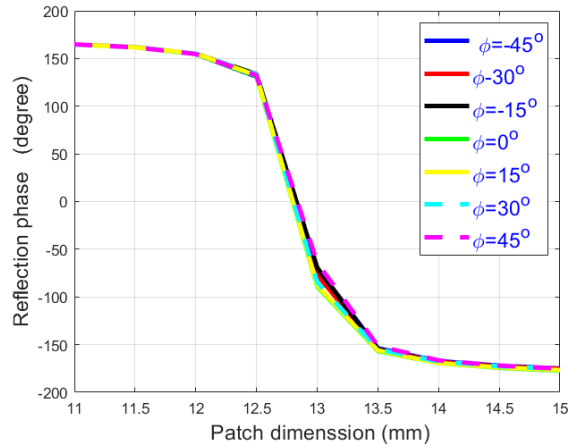
Figure 5.11. Phase variation of single layer unit cell (θ=40°).
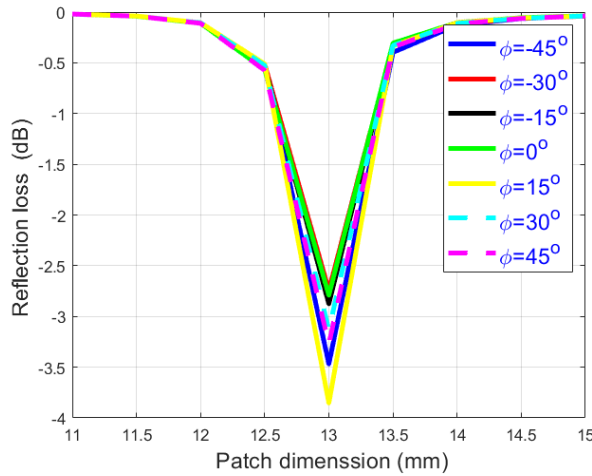
Figure 5.12. S11 parameter of single layer unit cell (θ=40°).

One of the inherent drawbacks of microstrip reflectarray antennas is their narrow bandwidth nature. The bandwidth of small and medium-sized reflectarray mainly depends upon the bandwidth of individual array elements, whereas for large reflectarray, the bandwidth is governed by differential spatial delay. For small and medium-size reflectarray, the element bandwidth is an imperative design parameter that needs thorough investigation while analyzing a unit cell. The substrate thickness is considered as the main parameter affecting the bandwidth of an element. Generally, elements with thicker substrates provide better bandwidth. Other than substrate thickness, the phase tuning techniques also widely affect the bandwidth performance of the element. In each method, different parameters specify the bandwidth performance. For example, in delay line techniques, return loss bandwidth is taken as element bandwidth. At the same time, in the case of the variable rotation method, the tolerance level of the cross-polarization or 3dB axial ratio determines the element bandwidth. However variable size method has a bit

more complex criteria to determine the element bandwidth. In the variable size method, the bandwidth is selected from the slope of the phase curve. The phase curve with a slight slope provides better bandwidth performance. This bandwidth definition is based on how fast the element the phase changes concerning frequency. The bandwidth performance of the proposed single-layer unit cell is shown in Figure 5.13.

The phase curves vs. patch dimension for three frequencies 9 GHz, 10 GHz, and 11 GHz are plotted in Figure 5.13. The phase difference between two consecutive frequencies is significant, and the phase change quite rapidly with the change in frequency.
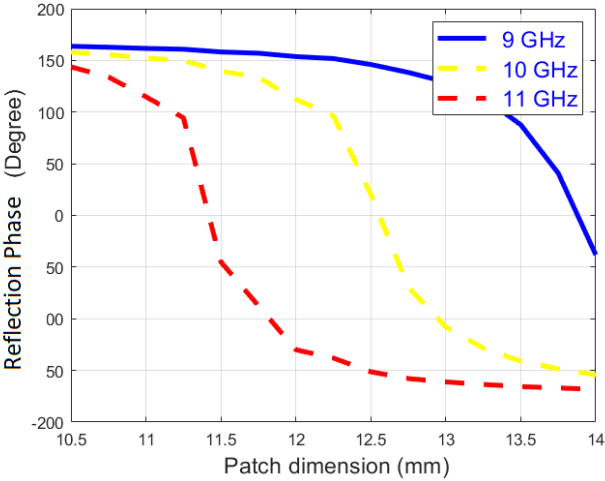
Figure 5.13. Bandwidth analysis of single-layer unit cell.

It can be seen from the curve that when the frequency has increased, the nonlinearity also increases, and consequently, the bandwidth efficiency is decreased. This nonlinear dependency of the phase curve on the frequency for reflectarray with variable size elements is the main reason for its narrowband behavior.

As described above, the substrate thickness is one of the critical parameters affecting the element bandwidth. It is essential to analyze the phase curve variation corresponding to substrate thickness variation. The effect of substrate thickness on phase range and return loss are shown in Figures 5.14-5.15.
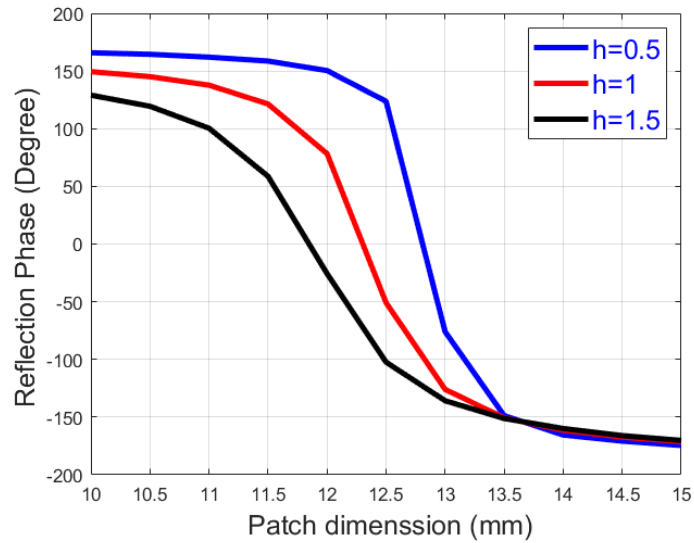
Figure 5.14. Effect of substrate thickness on phase variation.

The phase-length curve and return loss are plotted for three different substrate thicknesses, which are 0.5 mm, 1 mm, and 1.5 mm respectively. The increasing trend in thickness makes the phase curve less steep and improves return loss characteristics but at the cost of phase range which reduces accordingly.
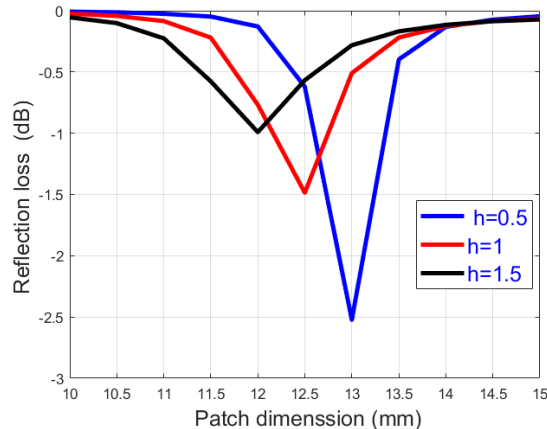
Figure 5.15. Effect of substrate thickness on return loss.

5.1.2. Two Layer Unit Cell

The phase curves depicted in Figures 5.2-5.15 show that the phase range for a single layer square patch on 0.5 mm thick textile substrate is approximately around 330° but the variation is highly nonlinear. Due to this nonlinearity, the reflectarray is very sensitive to fabrication tolerance. Moreover, the reflection phase also has a narrow frequency band of operation. These shortcomings can be overcome by introducing air as a second layer between the textile and ground plane. The second layer produces more gradual slope

variation, which results in wider element bandwidth. The improved design is shown in Figure 5.16. The first layer consists of the square patch and 0.5 mm thick textile dielectric substrate, and then there is air sandwiched between the ground plane and textile layer. The comparison between the phase-length curve for a single layer and two-layer unit cell is shown in Figure 5.17.
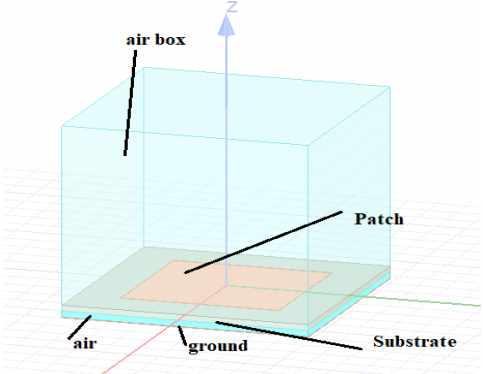
Figure 5.16. Two-layer unit cell.
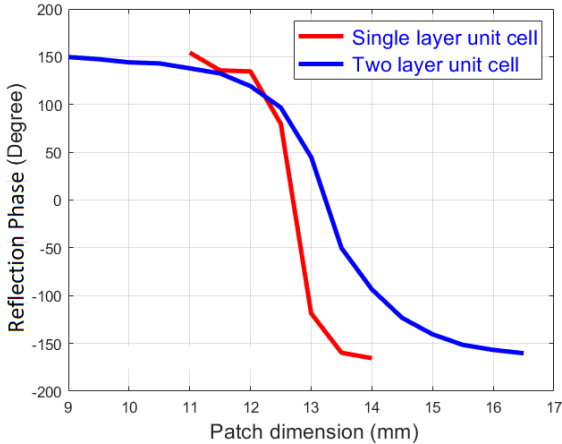
Figure 5.17. Phase variation for the two-layer unit cell.

As it can be seen from the figure that the single layer unit cell is highly nonlinear and have narrow bandwidth, and the insertion of air between substrate and ground plane as a second layer improves the unit cell performance extensively. The improved two-layer design is now more linear and wideband as compared to a single layer. As stated earlier, incident angles are also essential to consider for design performance as both phase and magnitude depend upon them. The maximum allowable incident angle is dependent upon two main factors, which are feed coordinates and array size, but during unit cell analysis, the general rule for incident angle is that if the jump between phase-length curve for a normal and oblique incident is more than 50° it must be avoided. The phase curve and

return loss vs. dimension for different incident angles of two-layer unit cells are presented in Figures 5.18 -5.19.
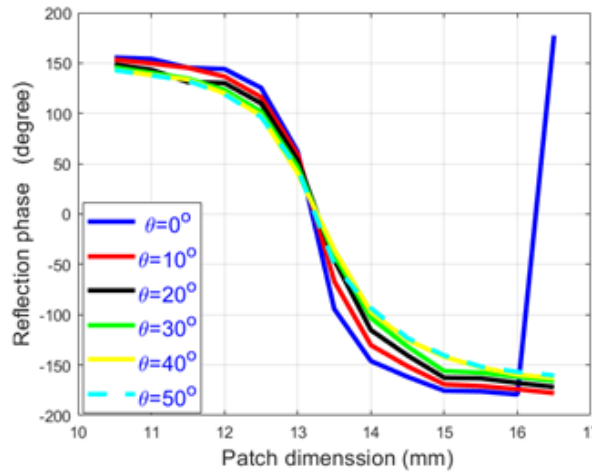
Figure 5.18. The return phase of two-layer unit cell ($\varphi=0^o$).
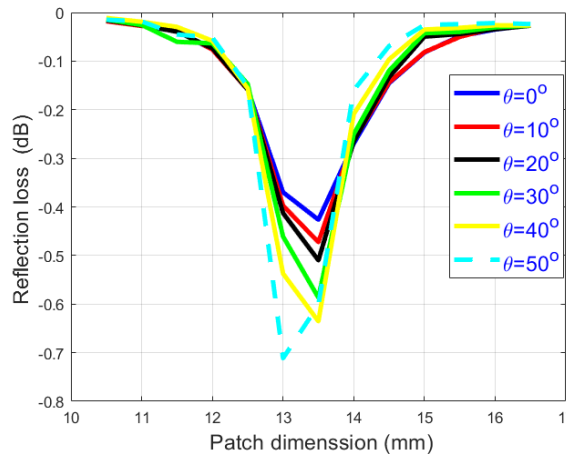
Figure 5.19. The return loss of two-layer unit cell ($\varphi=0^o$).

In the above figures, the results are plotted for incident angles by varying θ from 0° -50° while keeping φ at 0°. By comparing the phase curves of single-layer and two-layer unit cells it is observed the effect of oblique incident angles is more prominent in the design with a thicker substrate than the thinner one. Figures 5.14- 5.15 show that both the phase and magnitude of reflected wave vary significantly as the incident angle changes from 0° -50° degrees. It can also be observed that for the oblique incident with 50° angle shows maximum variation, which is around 50° from the normal incident and have higher-order resonance for the patch whose size is near or equal to the size of the substrate. Therefore, for two-layer unit cells, the useable incident angles range between 0°-50°. Figures 5.20- 5.21 represent the phase and magnitude of the reflected waves for incidence angle $\theta=0^o$-

50° and $\varphi=90^o$ whereas the results for φ variation form -45° to 45° while θ was fixed at 30° degree is shown in Figures 5.22-5.23 respectively.
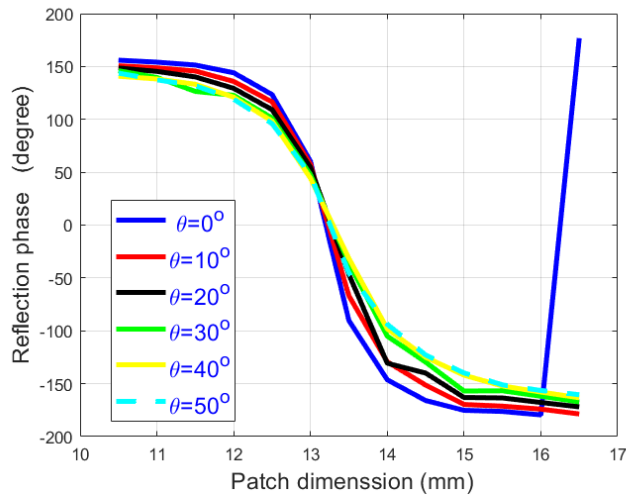
Figure 5.20. Phase variation of two-layer unit cell ($\varphi=90^o$).
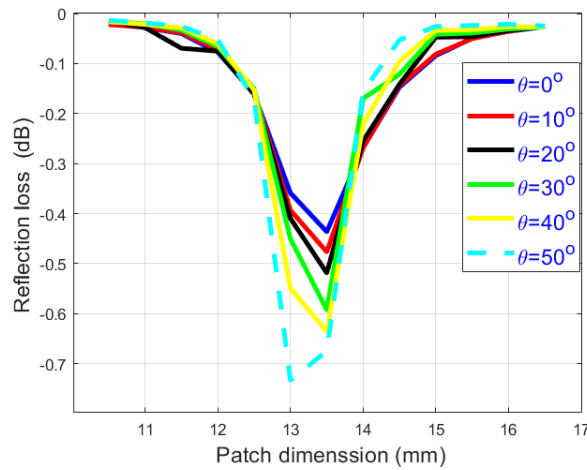
Figure 5.21. The return loss of two-layer unit cell ($\varphi=90^o$).
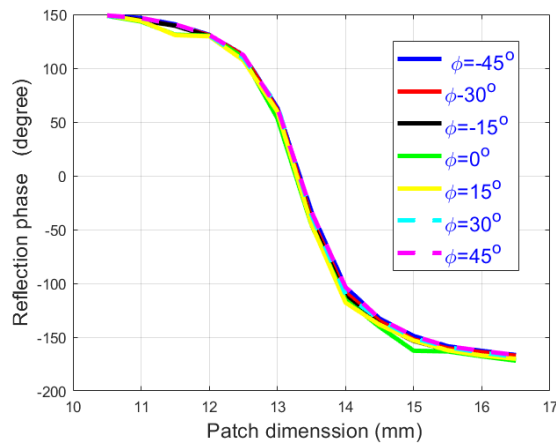
Figure 5.22. Phase variation of the two-layer unit cell ($\theta=30^o$).
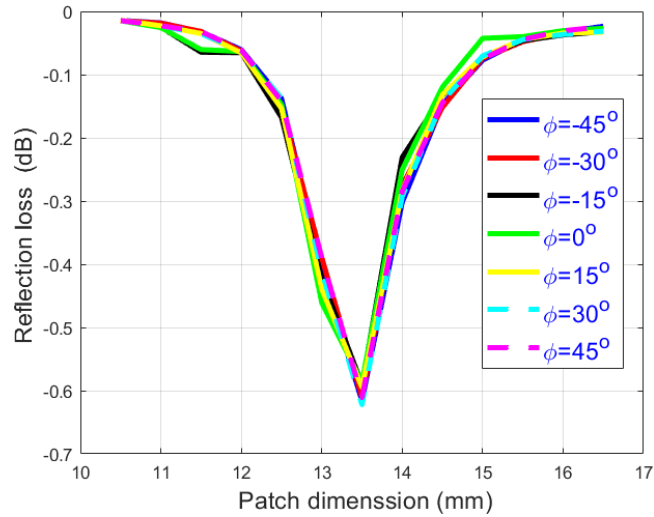
Figure 5.23. The return loss of two-layer unit cell ($\theta=30^\circ$).

The effect of thickness of air on phase characteristics of a two-layer unit cell is shown in Figure 5.24. It is noted that the design with 0.5 mm air thickness showed the best performance in terms of phase range. The other two designs show good bandwidth behavior but have a lower phase range. The design with a 1 mm thick air layer is selected for further analysis based on the above results.
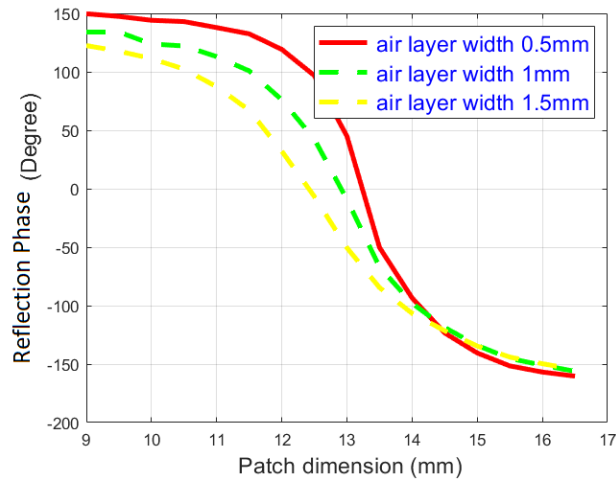
Figure 5.24. Effect of thickness of air layer on phase variation.

As it was concluded from Figure 5.13 that single layer unit cell has narrow bandwidth characteristics, now the effect of air as a second layer on bandwidth will be examined. The following graph (Figure 5.25) shows the bandwidth behavior of the two-layer design for three different resonant frequencies, 9 GHz, 10 GHz, and 11 GHz. It is observed that the design has improved bandwidth performance as compared to the single-layer design.

85

The phase change along the frequency is much slower as compared to the single-layer unit cell.
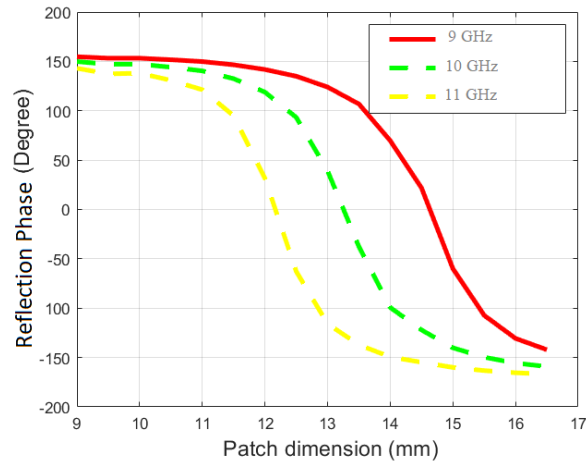
Figure 5.25. Bandwidth analysis of 2-layer unit cell.

So for, the performance of a unit cell in a simulated environment has been studied. At the end of the study, the final unit cell design with the following parameter is obtained.

Table 5.1. Final obtained parameters for the unit cell

Parameter	Value
Frequency	10 GHz
Dielectric constant ε_r	1.65
Loss tangent $tan\delta$	0.002
Radiating patch Length L	13 mm
Radiating patch Width W	13 mm
Substrate thickness	0.5 mm
Width of air layer x	1 mm
Unit cell dimension	17.1x17.1 mm
No of layers	2

The unit cell analysis analyzes the phase range, bandwidth, and radiation pattern of a single unit cell. To design a reflectarray with desired radiation and beam characteristics, the exact phase distribution for reflectarray elements must be determined.

5.2. System Design

In the previous section, we analyzed the phase range and bandwidth of the unit cell. In this section, the phase distribution on the aperture of reflectarray is discussed, which lies

in system design. The system design is based on the phase shift provided by each element and the feed configuration. Both things determine the directivity, gain, and efficiency of reflectarray.

5.2.1. Aperture Phase Distribution

The concept of parabolic reflector and reflectarray is shown in Figure 5.26.
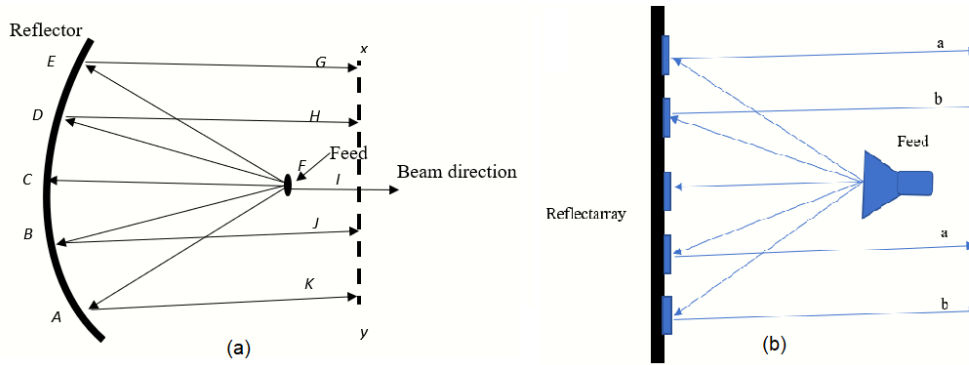
Figure 5.26. (a) Parabolic reflector. (b) Reflectarray.

Figure 5.26 (a) represents the reflection of the incident field from a parabolic reflector whereas, Figure 5.26 (b) shows reflection from a reflectarray antenna. In a planar antenna array, the beam yields in a broadside direction due to uniform phase distribution on the aperture. The progressive phase distribution is required to focus a beam in a particular direction. The basic working principle of a reflectarray is the same: every array element yields a progressive phase distribution [132]. Other factors that also affect the phase distribution are the position of feed and the angle of incident. [140]. A feed antenna illuminates a far-field reflectarray antenna with a particular incident angle. The distance determines the phase of the incident field on the aperture traveled, known as spatial phase delay. To focus a beam in a desirable direction, the elements of the array have to compensate for the phase difference by using one of the above mentioning techniques; a general mechanism of a reflectarray is shown below in Figure 5.27.

The phase of the reflected wave from the reflectarray element should compensate for the spatial phase delay (SPD) from the phase center of feed to that element. The mathematical expression for SPD is given in equation 5.1.

$$\phi_{spd} = -k_0 R_i \tag{5.1}$$

Where ϕ_{spd} is spatial phase delay, k_0 is wavenumber and R_i is the distance of ith element from the phase center of the feed.
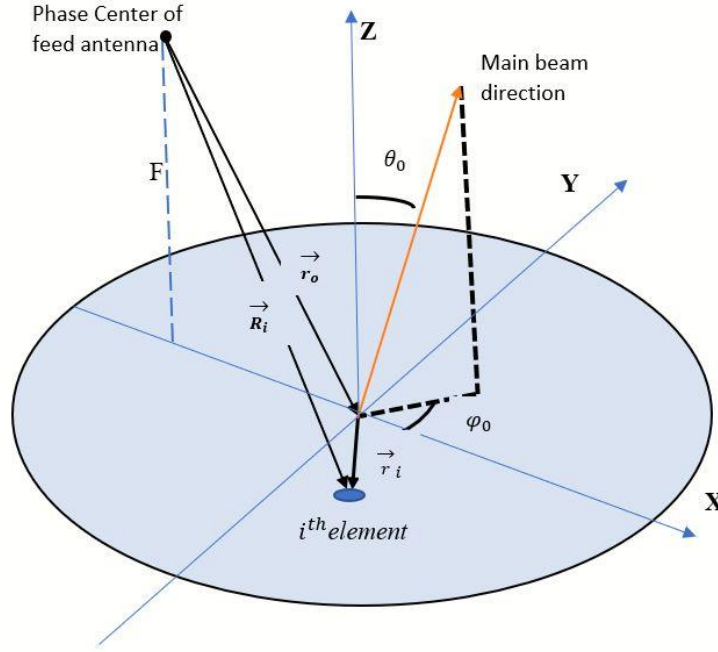
Figure 5.27. Geometric setup of feed and reflectarray [132].

To focus the beam in a desirable direction, every element of the array yields progressive phase distribution [141], [142]. The progressive phase (pp) on the aperture of the reflectarray can be calculated by using equation 5.2.

$$\phi_{pp} = -k_0(x_i sin\theta_0 cos\varphi_0 + y_i sin\theta_0 sin\varphi_0) \tag{5.2}$$

On the other hand, the progressive phase distribution is the sum of spatial phase delay and phase distribution of individual elements

$$\phi_{pp} = \phi_{spd} + \phi_R(x_i, y_i) \tag{5.3}$$

Where $\phi_R(x_i, y_i)$ is phase shift for individual elements.

Therefore, a reflectarray element should compensate for spatial phase delay SPD and progressive phase pp on the aperture to get the desired phase shift mathematically represented below.

$$\phi_R(x_i, y_i) = k_0\big(R_i - sin\theta_0(x_i cos\varphi_0 + y_i sin\varphi_0)\big) \tag{5.4}$$

The equation above determines the phase required by the elements to shape the beam in the desired direction. The equation is based on two essential paraments: the distance between central and other reflectarray elements. The other factor is the position of the feed [140]. The effects of feed orientation on reflectarray performance are described in the next section.

5.2.2. Effect of Antenna Feed

After determining the correct phasing element, the next most important parameters are the position of the feed antenna and its radiation pattern. Reflectarray performance directly depends upon these two factors. A feed antenna illuminates at the far-field of the reflectarray antenna with a particular incident angle. Figure 5.28 shows the excitation of reflectarray through an oblique incident plane wave. The placement of the horn antenna to the correct location concerning the geometric center of reflectarray is very critical to have desired incident angle. Figure 5.29 explains the effect of feed orientation on incident angles. Figure 5.29 (a) shows the center feed, while Figure 5.29 (b) shows offset feed orientation. The central feed has a normal incidence on the geometric center of reflectarray and oblique incidence toward the corner. The value of oblique incident angle depends upon the distance F of horn antenna from reflectarray, and size D of the reflectarray. For offset configuration, the wave incident on the geometric center of reflectarray with a certain incident angle. To excite reflectarray the feed antenna must be at least a far-field distance away from reflectarray [140].
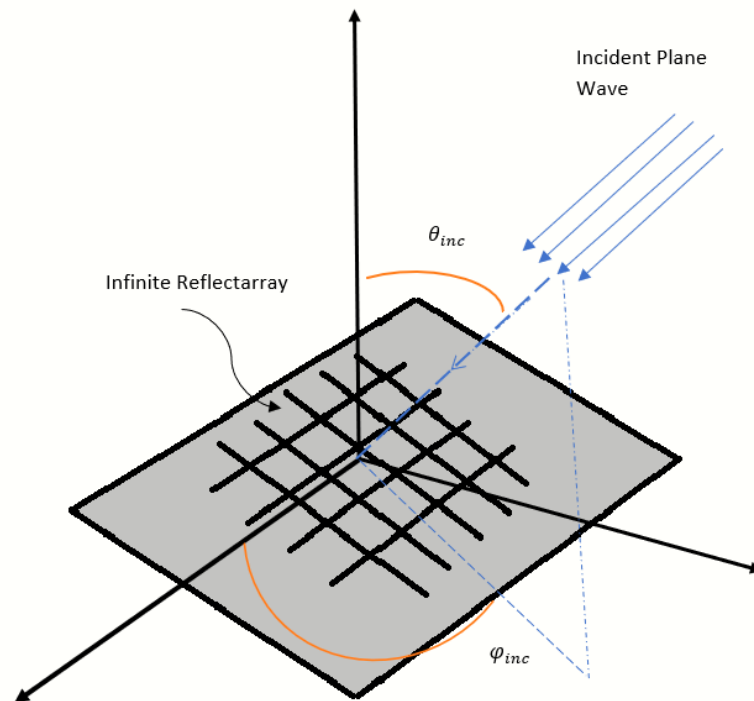
Figure 5.28. Oblique plane wave incidence on infinite reflectarray
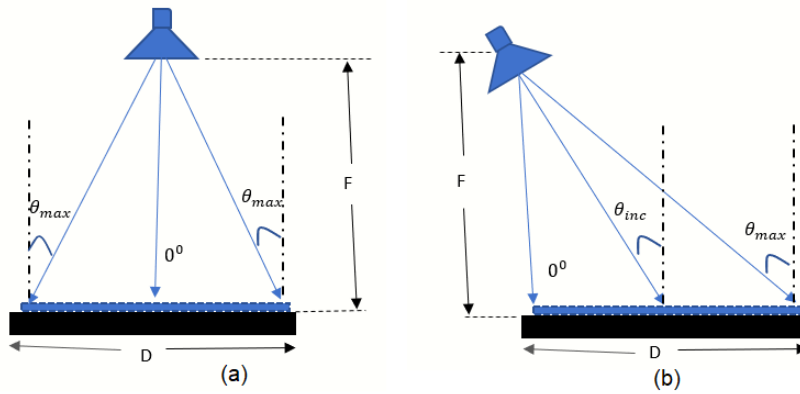
Figure 5.29. Effect of feed orientation on the incident angle, (a) center feed, (b) Offset feed.

This study uses the FMI-16240-15 model X-band horn antenna developed by Flann Microwave Limited as a feed antenna.

Table 5.2. Parameters of horn antenna

Parameters	Value
Frequency band	8.2GHz-12.5GHz
Cutoff frequency	6.5 GHz
A	61 mm
B	44 mm
D	75 mm
L	124 mm
Gain	15 dB

The far-field distance for the given horn antenna can be calculated by using the formula

$$R = \frac{2D^2}{\lambda} \qquad (5.5)$$

Here $D = 75$ mm is the largest dimension of horn antenna whereas, $\lambda = 30\ mm$ corresponds to 10 GHz central frequency. To be at the far-field, both antennas must be more than 375 mm apart from each other. The two different scenarios, one with central feed and the other with offset feed orientation are considered in this study.

5.3. Field on Reflectarray Elements

The incident field on each element of reflectarray depends upon the orientation and radiation pattern of the feed antenna. Although there are many examples of using microstrip array, dipole, and other antennas for feeding purposes, the horn antenna is the most used antenna to feed a reflector or a reflectarray. The radiation pattern of antennas

can be modeled by using different mathematical functions the simplest $cos^q(\theta)$ is used here. The advantage of using this model is that the signal parameter q controls the directivity and shape of the antenna. The x and y-polarized radiation fields from an ideal horn antenna are following [143].

$$E_x(\theta,\varphi) = \frac{jke^{-jkr}}{2\pi r}\left[\hat{\theta}C_E(\theta)cos(\varphi) - \hat{\varphi}C_H(\theta)sin(\varphi)\right] \tag{5.6}$$

$$E_y(\theta,\varphi) = \frac{jke^{-jkr}}{2\pi r}\left[\hat{\theta}C_E(\theta)sin(\varphi) + \hat{\varphi}C_H(\theta)cos(\varphi)\right] \tag{5.7}$$

Here r is the vector from horn antenna phase center to the element of reflectarray, θ,φ are the spherical angles of feed coordinate system whereas, C_E and C_H determine the E and H plane radiation pattern of the feed and can be specified as

$$C_E = cos^{q_E}(\theta) \ , C_H = cos^{q_H}(\theta) \tag{5.8}$$

For axial symmetric pattern $q_E = q_H$ is considered.

The normalized power for the feed modeled with the above mathematical function can be described as

$$P(\theta,\varphi) = \begin{cases} cos^{2q}(\theta) & \text{for } 0 \leq \theta \leq \frac{\pi}{2} \\ 0 & elsewhere \end{cases}$$

(5.9)

5.4. Reflectarray Efficiency

To observe the performance of reflectarray its efficiency must be determined. The aperture type of antennas, like a parabolic reflector and reflectarray, the directivity and gain mainly depend upon the physical aperture. Aperture efficiency is the main criterion to determine the performance of an aperture antenna. The comparison of the aperture efficiency of a parabolic reflector and a reflectarray is shown in the figure below [144].
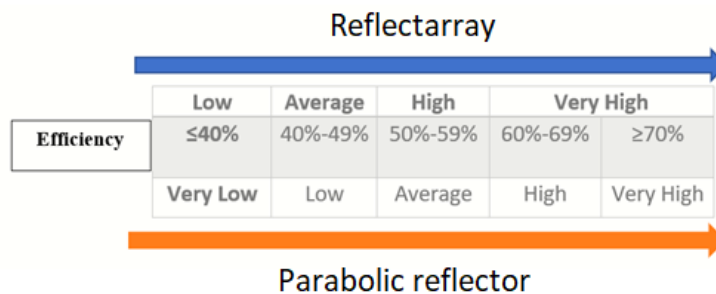
Figure 5.30. Comparison of efficiency of parabolic reflector and reflectarray [144].

Figure 5.30 presents a comparison between the efficiency of a parabolic reflector and reflectarray, the efficiency of a reflectarray is always less than a parabolic reflector of the same size.

The efficiency of a reflectarray depends upon many factors and is the most complex parameter to optimize. The feeding method influences the reflectarray efficiency widely. The feed footprint, subtended angle and radiation pattern are essential considerations that must be kept in mind while designing a reflectarray.

The aperture efficiency of reflectarray is the product of illumination and spillover efficiencies [145].

$$\eta_a = \eta_i \eta_s \qquad (5.10)$$

where η_a is the aperture efficiency η_i , and η_s are the illumination and spillover efficiencies. These two efficacies work oppositely. As shown in the figure, reducing illumination loss will increase the spillover loss and vice versa, and the optimal point must be determined to improve performance.
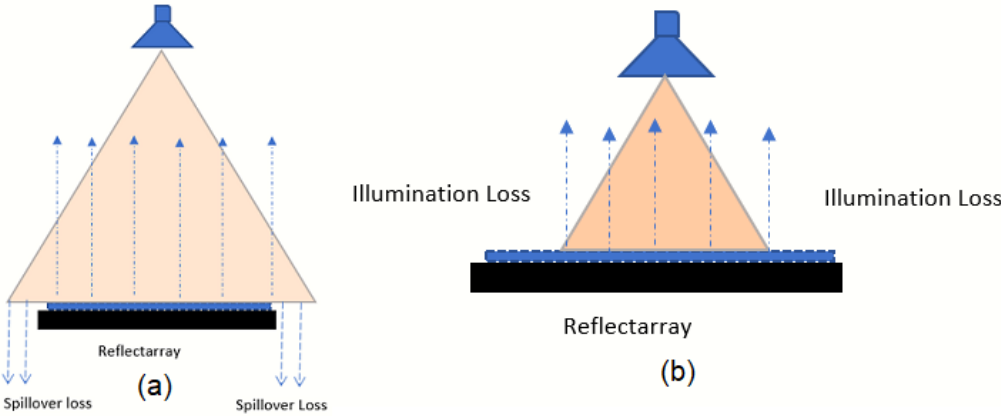
Figure 5.31. (a) Spillover and (b) illumination losses.

5.4.1. Illumination Efficiency

A feed antenna illuminates the reflectarray with a specific footprint. Suppose the reflectarray is very big or the footprint of reflectarray is so small that it illuminates only the central element of reflectarray. In that case, the reflectarray will have higher illumination loss, resulting in low illumination efficiency. It is important to note that

central feed and offset feed configurations have a different footprint, as shown in Figure 5.32.
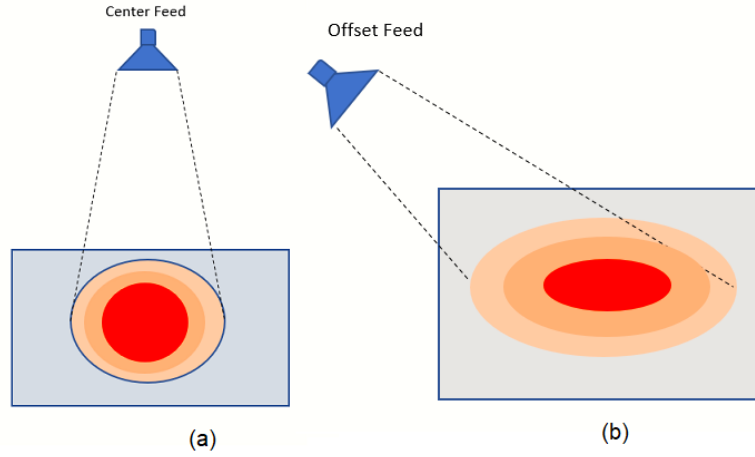
Figure 5.32. The footprint of (a) center and (b) offset feed configuration.

The illumination efficiency for central fed reflectarray with square aperture is calculated as follows [144].

$$\eta_i = \frac{\pi\left[\left\{\frac{\left(1-cos^{q+1}(\theta_s)\right)}{(q+1)}\right\}+\left\{\frac{\left(1-cos^{q}(\theta_s)\right)}{q}\right\}\right]^2}{8tan^2(\theta_s)\left[\frac{\left(1-cos^{2q+1}(\theta_s)\right)}{(2q+1)}\right]}$$

(5.11)

where θ_s is the half of the subtended angle of the feed.

$$\theta_s = tan^{-1}\left[\frac{D}{2F}\right]$$

(5.12)

The D is the maximum dimension of reflectarray, and F is the focal length of feed from the phase center of reflectarray. The equations indicate that the subtended angle only depends upon the F/D ratio.

For offset feed configuration following relation is used to estimate the illumination efficiency [145].

$$\eta_i = \frac{\iint_A \frac{1}{R}\left(\frac{r_0^2+R^2-s^2}{2Rr_0}\right)^q \left(\frac{F}{r}\right)^{qe} dxdy}{A_a \iint_A \frac{F}{R^3}\left(\frac{r_0^2+R^2-s^2}{2Rr_0}\right)^{2q} dxdy}$$

(5.13)

A_a is total area of reflectarray, R is magnitude of position vector from phase center of feed to reflectarray elements, r_o is magnitude of position vector from phase center to the geometric center of the reflectarray, while s is magnitude of position vector form

93

geometric center of reflectarray to the reflectarray element. The spillover efficiency for center feed reflectarray is determined as under [144].

$$\eta_s = 1 - \cos^{2q+1}(\theta_s) \tag{5.14}$$

Whereas for offset configuration, spillover efficiency is [145].

$$\eta_s = \frac{\int \int_A \frac{F}{R^3} \left(\frac{r_0^2 + R^2 - s^2}{2Rr_0} \right)^{2q} dxdy}{\frac{2\pi}{2q+1}} \tag{5.15}$$

Besides these, the other factors affecting the reflectarray performance include phase efficiency, material loss, polarization efficiency, blockage efficiency, and feed efficiency. Although all these factors influence reflectarray total gain and directivity of reflectarray, spillover and illumination efficiencies are the major ones among them.

The feed antenna plays a vital role in the performance of reflectarray. The aperture, illumination, and spillover efficiencies of reflectarray are drastically affected by the choice of feed antenna and its location. Suppose the subtended angle of the wave coming from the feed is very small or the aperture of reflectarray is very big. In that case, only array elements near the center are illuminated properly by incident waves, which causes illumination loss. On the contrary, if the subtended angle is too large or reflectarray size is too small, the feed signal exceeding the physical aperture of the antenna array causes spillover loss. Both these losses are complementary to each other, which implies that the optimal choice of feed distance F from reflectarray can provide good illumination and spillover efficiencies within a specific limit. To improve performance, other feed antennas with better radiation characteristics and gain have to choose. The X-band horn antenna is simulated in the HFSS simulation tool using the parameters given in Table 5.2. The simulated antenna is shown in Figure 5.33, while simulated and measured return loss is given in Figure 5.34.
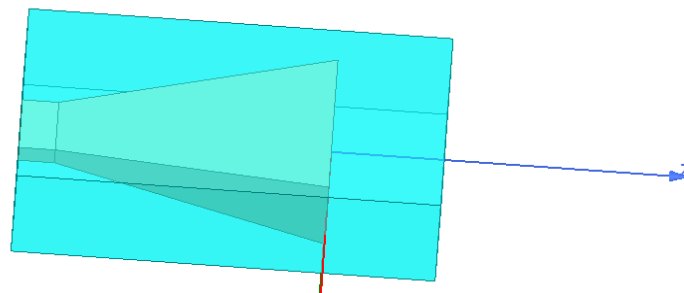
Figure 5.33. Simulate   X-band horn antenna.
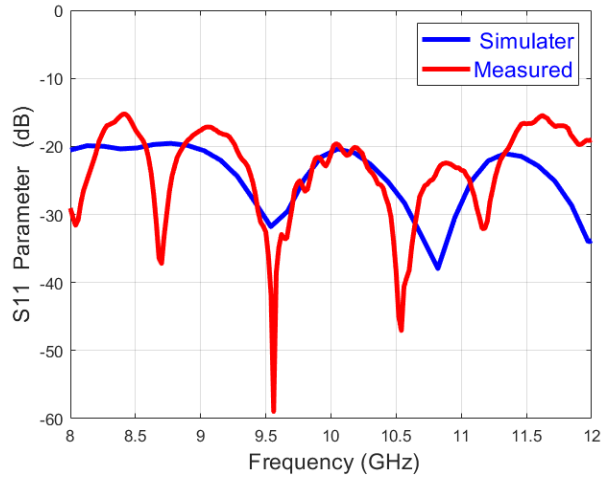
Figure 5.34. Measured and simulated return loss.

From Figure 5.34 it can be observed that the measured return loss of the FMI-16240-15 model X-band horn antenna is below -15 dB while it is below -20 dB for simulated design. The radiation pattern of the horn antenna is another factor that should be considered. To analyze the spread beamwidth of feed, the antenna's radiation pattern is shown in Figure 5.35. For -3 dB gain the beamwidth is around 32 degrees.
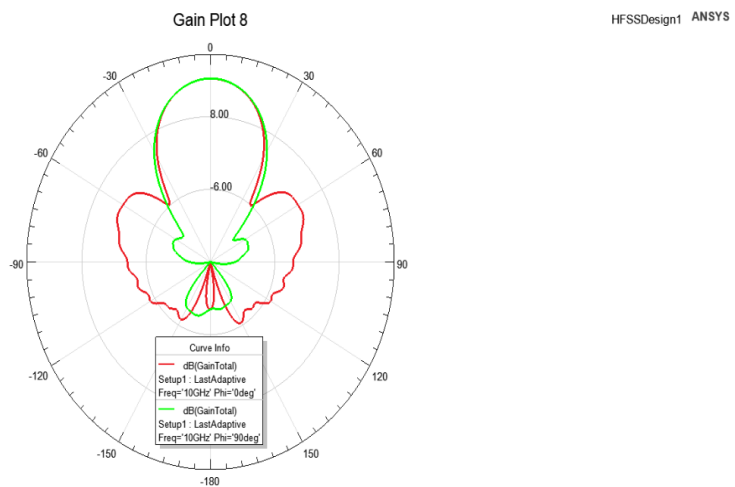
Figure 5.35. The radiation pattern of the horn antenna.

5.5. Feed Configuration

Two feed configurations center and offset feed are analyzed. To determine the optimum feed location first, maximum allowable incident angles are calculated. The mathematical relation use to determine the maximum incident angles obtained by considering the antenna geometries given in Figure 5.27.

$$\theta_{inc}(i,j) = \cos^{-1}\left(\frac{F}{\sqrt{F^2+(X_a-x_{ij})^2+y_{ij}^2}}\right) \quad (5.16)$$

$$\varphi_{inc}(i,j) = -\tan^{-1}\left(\frac{y_{ij}}{X_a-x_{ij}}\right) \quad (5.17)$$

In the above equation F distance of feed from reflectarray along the z-axis, X_a is the distance of feed from the geometric center of reflectarray along the x-axis. For center feed configuration, it is zero. Whereas x_{ij}, y_{ij} represent the coordinates of the unit cell located along the (i,j) index. The phase distribution on the center and offset feed configurations are presented in next sections.

5.5.1. Center Feed Configuration

For the center feed configuration, the feed antenna must be located at some height h from the geometric center of the reflectarray and, incident wave impinges on the geometric center with 0º. For center feed configuration, the feed coordinates are H (0,0, F). The reflectarray with 15×15 elements with center feed configuration is shown in the figure below.
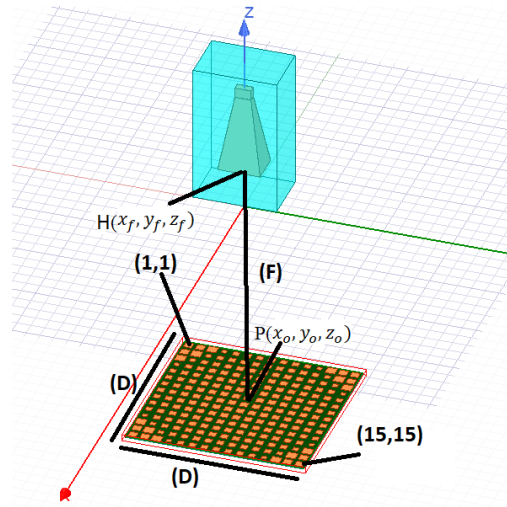
Figure 5.36. Center feed configuration.

The incident wave impinges the phase center of the reflectarray with 0 degree, and as we move away from the center, the incident angle increases gradually. It approaches the maximum value at the edges. The incident angles on each element from the phase center of the feed for center feed configuration are presented in the table given below and its colored map is presented in figure 5.37.

Table 5.3. Incident angles theta $\theta_{inc}(i, j)$ for center feed configuration

X Y	1	2	3	4	5	6	7	8	9	10	11	12	13	14	15
1	23	22	20	19	18	18	17	17	17	18	18	19	20	22	23
2	22	20	19	17	16	15	15	15	15	15	16	17	19	20	22
3	20	19	17	16	14	13	12	12	12	13	14	16	17	19	20
4	19	17	16	14	12	11	10	10	10	11	12	14	16	17	19
5	18	16	14	12	10	9	8	7	8	9	10	12	14	16	18
6	18	15	13	11	9	7	6	5	6	7	9	11	13	15	18
7	17	15	12	10	8	6	4	2	4	6	8	10	12	15	17
8	17	15	12	9.9	7	5	2	0	2	5	7	10	12	15	17
9	17	15	12	10	8	6	4	2	4	6	8	10	12	15	17
10	18	15	13	11	9	7	6	5	6	7	9	11	13	15	18
11	18	16	14	12	10	9	8	7	8	9	10	12	14	16	18
12	19	17	16	14	12	11	10	10	10	11	12	14	16	17	19
13	20	19	17	16	14	13	12	12	12	13	14	16	17	19	20
14	22	20	19	17	16	15	15	15	15	15	16	17	19	20	22
15	23	22	20	19	18	18	17	17	17	18	18	19	20	22	23
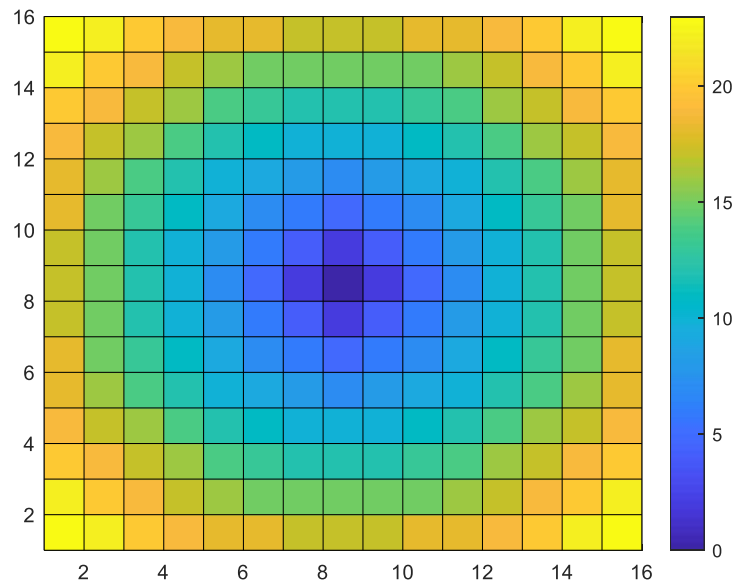
Figure 5.37. Incident angles impeging on reflectarray element in center feed configuration.

From the Table, it is observed that the maximum incident angle incidence on elements (1,1), (15,1), (1,15), and (15,15), which are situated at the edges of reflectarray is 23 degrees. In contrast, the central element has a 0-degree incidence angle. To keep the incident angle inside the θ_{max} Limit, the feed antenna height must be chosen carefully. It is also important to note that the feed antenna must be at least at the far-field distance from the reflectarray to excite the reflectarray with a spherical wave. The calculated far-field distance of the horn antenna is 375 mm the feed antenna must be placed at least a little more than this distance.

Efficiency Calculation for Center feed

The efficiencies for center feed configuration are calculated by using the equations 5.10, 5.11 and 5.14. The radiation pattern q of feed and *F/D* ratio are the main parameters determining the overall efficiency of center feed reflectarray. The normalized simulated feed gain and estimated gain for different values of q are plotted vs beamwidth in degrees in the figure below.
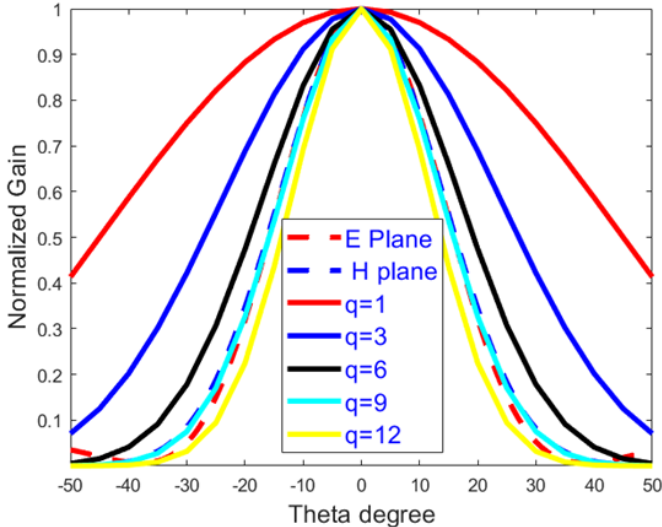
Figure 5.38. Feed antenna radiation pattern corresponding to different values of q.

As it can be seen from the figure that the radiation pattern of the feed antenna can be modeled with $q=9$. The optimum feed for a reflectarray or a parabolic reflector should have a radiation pattern with a higher value of q. The lower value of q results in efficiency degradation. The illumination, spillover, and aperture efficiency for center feed configuration for different values of q are shown in Figure 5.39.
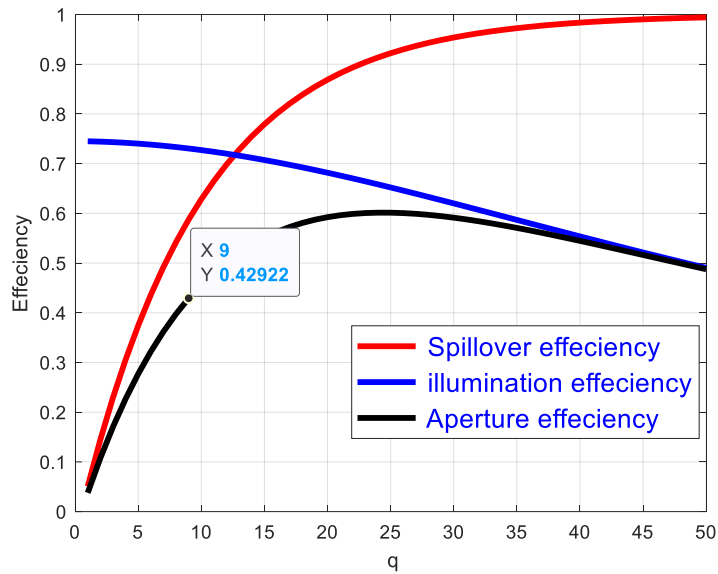
Figure 5.39. Effect of q on reflectarray efficiency.

The spillover efficiency is low for lower values of q and increases as the value of q increases whereas, illumination efficacy has a higher value for low q and decreases gradually for increasing values of q. For the horn antenna used in the analysis modeled with q=9, the aperture efficiency turned out to be 42.5%, which lies in the high-efficiency range.

The effect of the F/D ratio on antenna efficiencies is presented below.
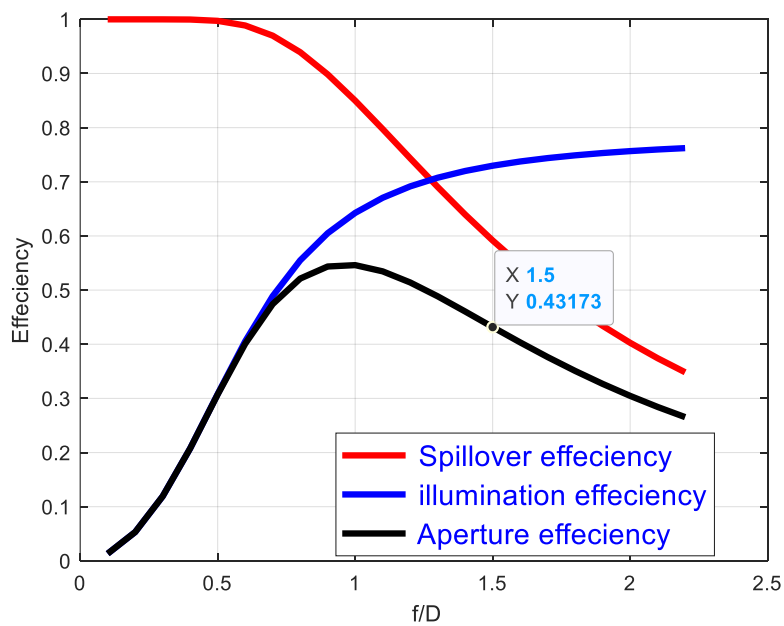
Figure 5.40. Effect of the F/D ratio on antenna efficiencies.

The antenna efficiencies are plotted against different F/D values. The maximum efficiency is obtained when the F/D ratio is equal to 1. For center feed configuration, the reflectarray consists of 15×15 elements, and the overall size of reflectarray is 256.5×256.5 mm. In contrast, the feed is placed at 387 mm above the reflectarray geometric center, chosen empirically. The F/D ratio for the center feed configuration is 1.5, which provides 43 % efficiency.

Phase Distribution and Radiation Pattern for Center Feed Configuration

The phase distribution on antenna aperture for optimum feed location (F=387 mm), horn radiation pattern with q=9, and reflectarray size D=256.5 mm, is computed using equation 5.3. The main beam is directed towards ($\theta_0=0^o$, $\varphi_0=0^o$). A python script developed by ANSYS corporation is used for the automation of reflectarray. The script takes phase vs. dimension curve, size and shape of the unit cell, number of elements, main beam direction, and feed coordinates as input and generates the required reflectarray. The required phase distribution to focus the reflected beam towards ($\theta_0=0^o$, $\varphi_0=0^o$). direction is shown in Figure 5.41.
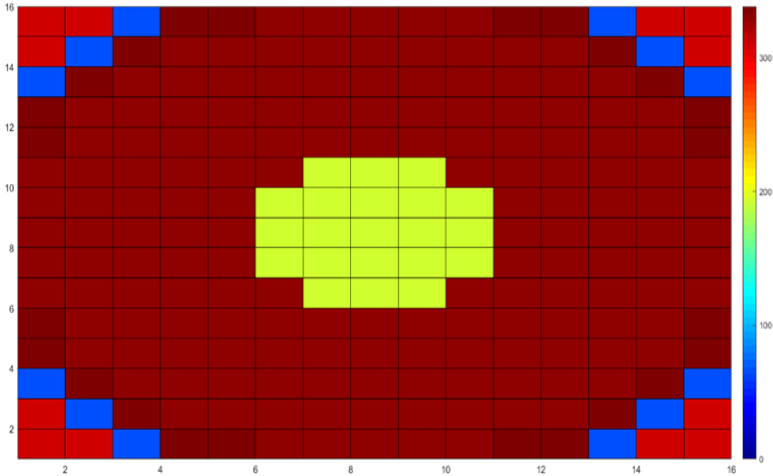
Figure 5.41. Phase distribution on aperture.

The radiation pattern of a reflectarray is computed through full-wave analysis. Feed transmit mode full-wave analysis is applied in this study. The feed antenna illuminates reflectarray aperture, and the far-field radiation pattern is obtained through the finite element method (FEM) in a hybrid finite element boundary integral approach (HFEBI) [146]. The simulated radiation pattern for the center feed configuration is shown in Figure 5.42.
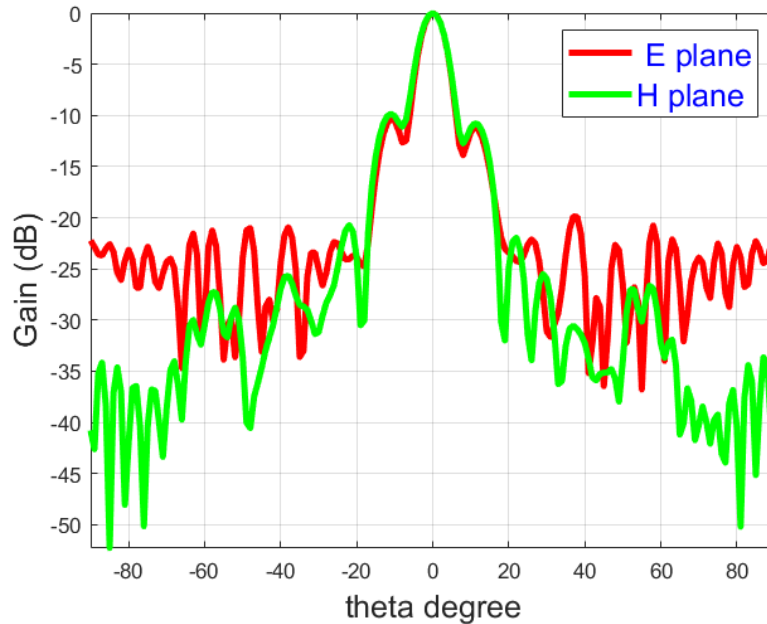
Figure 5.42. E and H- plane radiation pattern of center feed reflectarray.

The normalized E-plane radiation pattern is represented through the red line, and the H-plane radiation pattern is depicted through the green line. It can have been seen that the array is radiating in a broadside direction with narrow beamwidth. The first null has appeared at theta equal to 8 degrees, and the sidelobe levels (SLL) are below -10 dB.

5.5.2. Offset Feed

The center feed configuration is analyzed in the previous section. Although this configuration has yielded reasonably good aperture efficiency and radiation pattern but has a severe drawback due to feed blockage, which degrades the performance of reflectarray in terms of sidelobe levels. To overcome the feed blockage, an offset configuration is presented here. In offset configuration, the feed antenna is not located precisely above the geometric center of reflectarray, but in fact, it is situated some distance away from the geometric center and imaging the incident wave on center with some angle. The offset configuration is shown in Figure 5.43. The feed incident angle is set to 30°; the wave is reflected in the broadside direction ($\theta_0=0^o$, $\varphi_0=0^o$). The reflectarray consists of 17×17 elements and has a 290.7×290.7 mm aperture size.
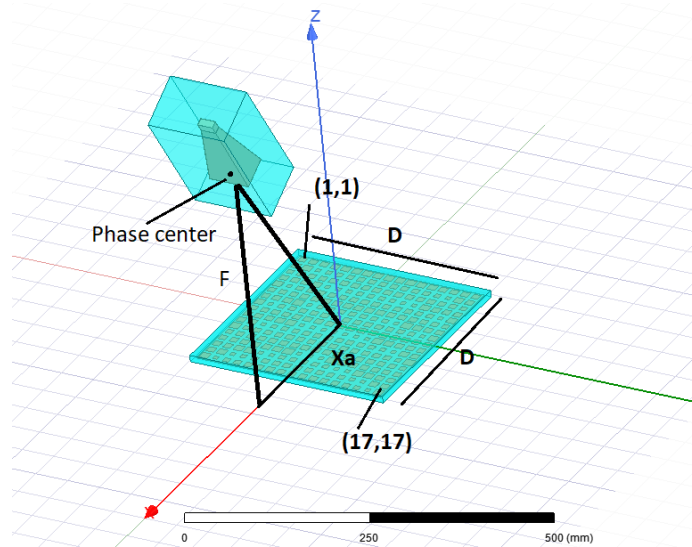
Figure 5.43. Offset feed configuration.

From Figure 5.32(b), it can be seen that the footprint of the offset feed is elliptical. As in offset case, the feed location depends upon both horizontal and vertical coordinates. Finding optimum feed location is more critical compared to the center feed configuration. To determine the feed location for the offset configuration, first, the incident angles received by each reflectarray element are calculated using equation 5.16. The obtained incident angles are enlisted in Table 5.4 and its colored map is given in Figure 5.44.

The maximum incident angle for offset configuration under investigation is $\theta_{max}=46^o$ degrees, received by the elements (1,1) and (1, 17) situated at the upper corners of the reflectarray. While the minimum incident angle received by elements (17,1) and (17,17) located at the corner near to the feed is $\theta_{min}=23^o$.

Table 5.4. Incident angles theta $\theta_{inc}(i, j)$ for offset feed configuration.

X / Y	1	2	3	4	5	6	7	8	9	10	11	12	13	14	15	16	17
1	46	45	45	45	44	44	44	44	44	44	44	44	44	45	45	45	46
2	44	44	44	43	43	43	43	42	42	42	43	43	43	43	44	44	44
3	43	43	42	42	42	41	41	41	41	41	41	41	42	42	42	43	43
4	42	41	41	41	40	40	40	40	40	40	40	40	40	41	41	41	42
5	41	40	40	39	39	38	38	38	38	38	38	38	39	39	40	40	41
6	39	39	38	38	37	37	37	36	36	36	37	37	37	38	38	39	39

102

7	38	37	37	36	36	35	35	35	35	35	35	35	36	36	37	37	38
8	36	36	35	34	34	34	33	33	33	33	33	34	34	34	35	36	36
9	35	34	33	33	32	32	31	31	31	31	31	32	32	33	33	34	35
10	34	33	32	31	30	30	30	29	29	29	30	30	30	31	32	33	34
11	32	31	30	29	29	28	28	27	27	27	28	28	29	29	30	31	32
12	31	29	28	28	27	26	26	25	25	25	26	26	27	28	28	29	31
13	29	28	27	26	25	24	24	23	23	23	24	24	25	26	27	28	29
14	28	26	25	24	23	22	22	21	21	21	22	22	23	24	25	26	28
15	26	25	23	22	21	20	19	19	19	19	19	20	21	22	23	25	26
16	25	23	22	20	19	18	17	17	16	17	17	18	19	20	22	23	25
17	23	22	20	19	17	16	15	14	14	14	15	16	17	19	20	22	23
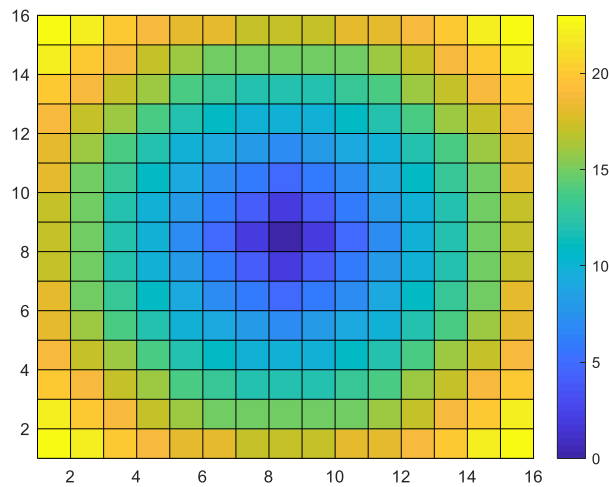
Figure 5.44. Incident angle impeging on reflectarray element in offset feed configuration.

Efficiency Calculation for Offset Configuration

The offset feed configuration's illumination, spillover, and aperture efficiency are calculated using equations 5.10, 5.13, and 5.15. The essential parameters required for efficiency calculation are listed in the table below.

Table 5.5. Parameters for offset configuration.

Parameter	Value
X_a	230 mm
F	380 mm
Distance between phase center of feed and geometric center of reflectarray	$\vec{r_o} = \overrightarrow{FP_0} = (-X_a)\hat{x} + y_o\hat{y} + (-F)\hat{z}$
Distance between phase center of feed and elements	$\overrightarrow{R_{\iota,j}} = \overrightarrow{FP} = (x - X_a)\hat{x} + y\hat{y} + (-F)\hat{z}$
Distance between geometric center and elements	$s_{\iota,j} = \sqrt{x_i{}^2 - y_j{}^2}$
Size of unit cell	0.56λ
Offset angle	θ_0
Radiation pattern of Horn	$cos^q(\theta)$
Radiation pattern of patch element	$cos^{q_e}(\theta).$

The radiation pattern of the unit cell also plays a vital role in efficiency calculation. Similar to the Horn antenna, the radiation pattern of the unit cell can be modeled by using $cos^{q_e}(\theta)$. The q_e for the unit cell used to be small. The normalized simulated unit cell gain is compared with estimated gain for different values of q_e. The results are shown in Figure 5.45. given below:
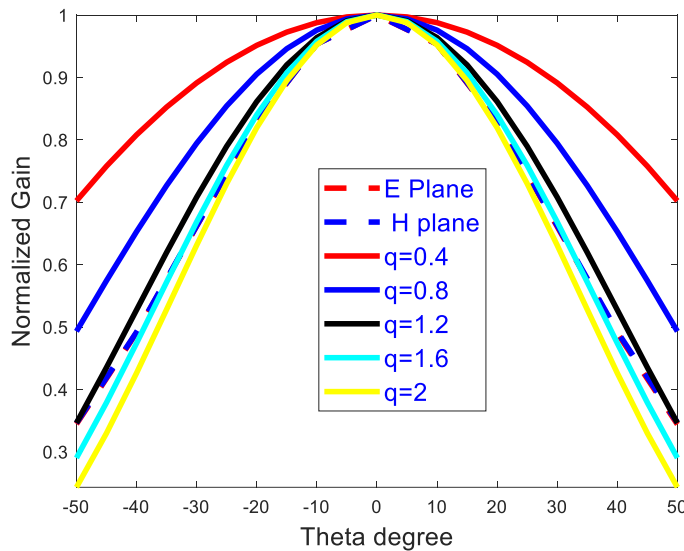
Figure 5.45. The radiation pattern of the unit cell concerning different values of q.

From the Figure, it can be seen that the E and H-plane radiation pattern is corresponding ratio pattern estimated through $q_e=1.6$.

The calculated efficiencies for different values of q for offset feed configuration with F=380 mm, X_a=380 mm and D=290.7 mm is shown below.
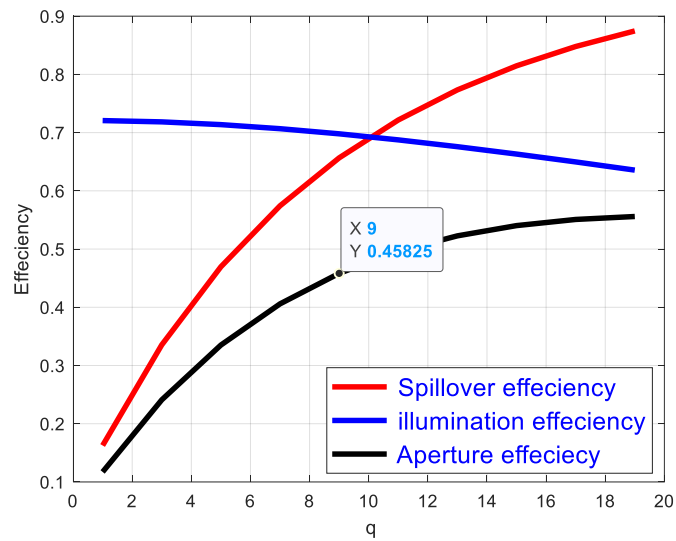
Figure 5.46. Calculated efficiencies of offset feed configuration concerning *q*.

It is observed from the figure that for offset configuration for *q*=9, the illumination efficiency is around 70%, Spillover efficiency is 65%, whereas the aperture efficiency is about 45%. The effect of the F/D ratio on efficiency is shown in Figure 5.47.
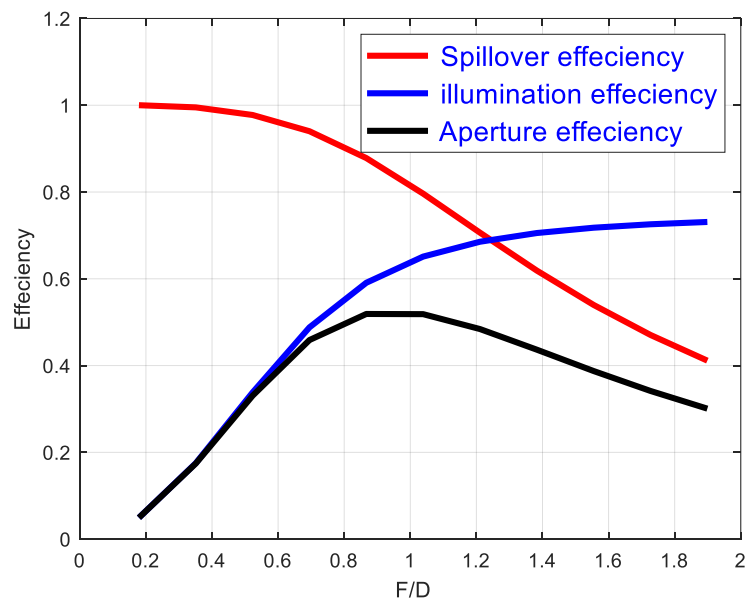
Figure 5.47. Efficiencies for F/D ratio.

The illumination efficiency concerning the 1.3 ratios of the focal length of feed and reflectarray aperture is around 69%, the spillover efficiency is about 65%, and the aperture efficiency is around 45%. It is observed that for given feed and reflectarray

parameters, the reflectarray with offset configuration has medium efficiency. Moreover, its efficiency is slightly lesser than that of the center feed configuration but does not have any feed blockage issue.

Phase Distribution and Radiation Pattern for Offset Feed Configuration

The phase distribution of offset configuration is shown in Figure 5.48, whereas the normalized radiation patterns are shown in Figure 5.49.
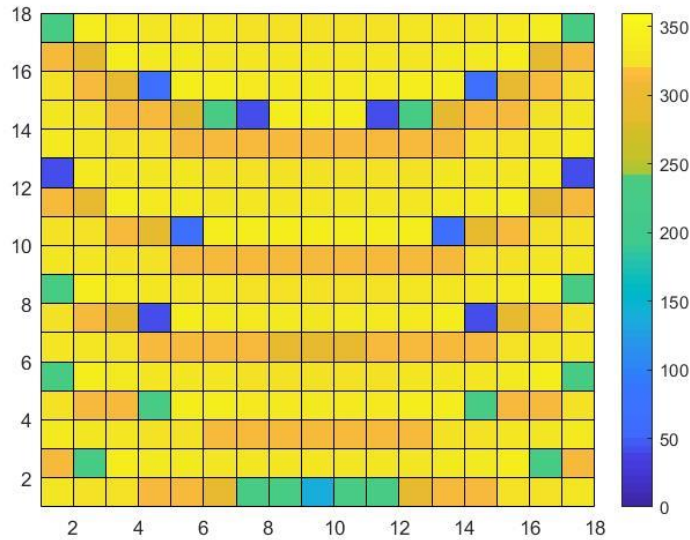
Figure 5.48. Phase distribution on reflectarray aperture for offset configuration.
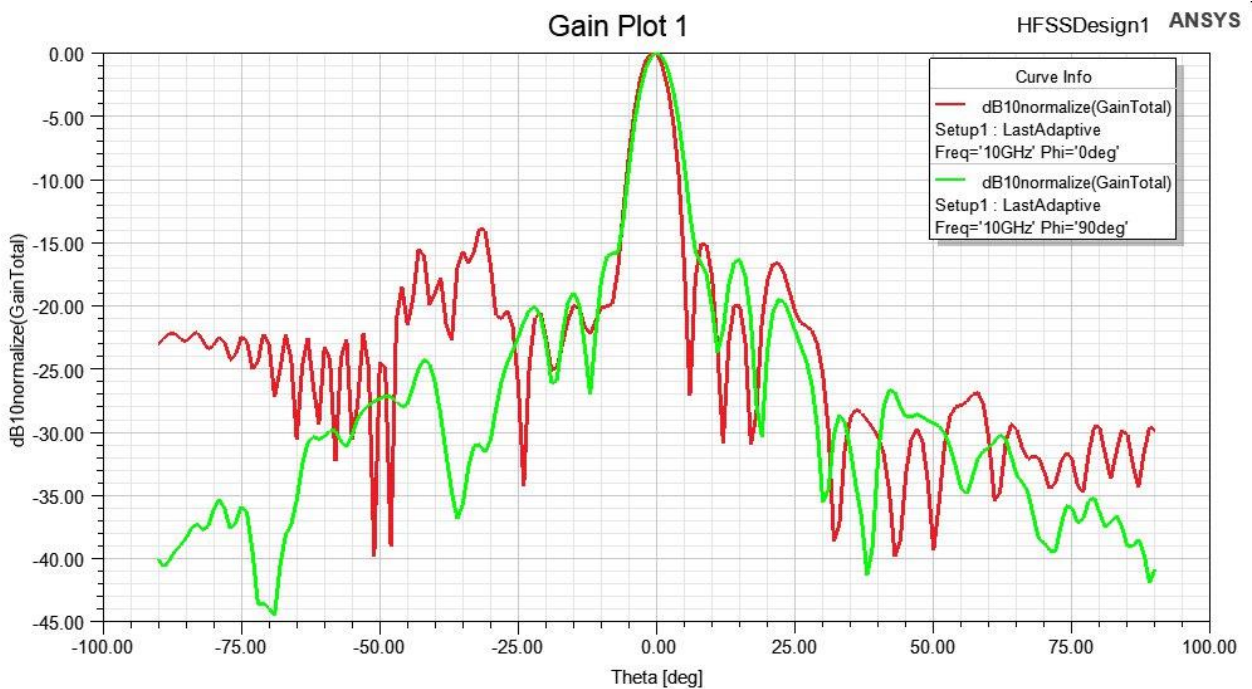
Figure 5.49. Radiation pattern of offset feed configuration.

The E- and H-plane radiation patterns represented with red and green lines are shown in Figure 5.49. It can be seen that the beam is directed toward the broadside. The first null to null beamwidth is around 14° degrees. The sidelobe levels are below -15 dB. In offset feed configuration, the sidelobe levels are improved 5 dB as compared to the center feed configuration.

6. Design Fabrications and Measurements

6.1. Fabrication and Test measurements

Both center and offset feed designs are fabricated on denim jeans by using silver-coated conducted thread. The computerized embroidery machine is used for the fabrication process. The jeans substrate, conductive thread, and embroidery machine are shown in Figure 6.1 while fabricated central and offset feeds are shown in Figure 6.2.-6.3 respectively.
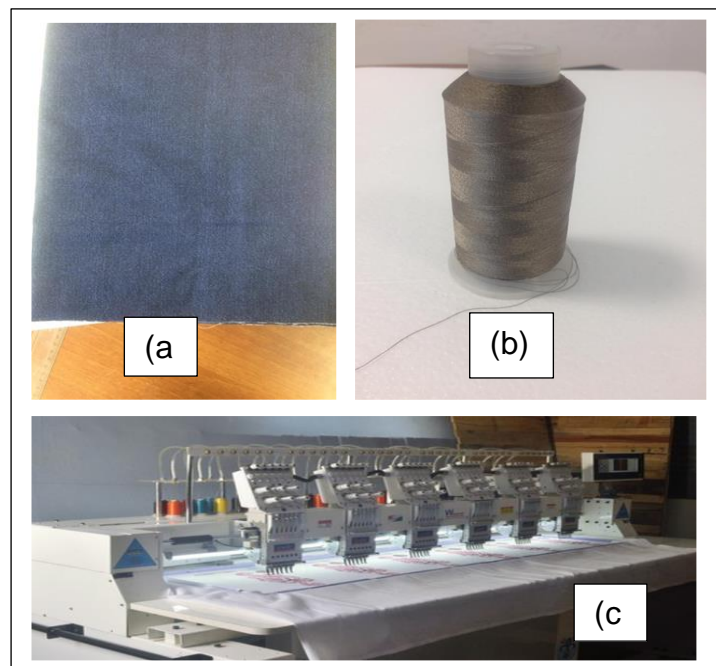
Figure 6.1. (a) Jeans substrate. (b) Conductive thread. (c) computerized embroidery machine.
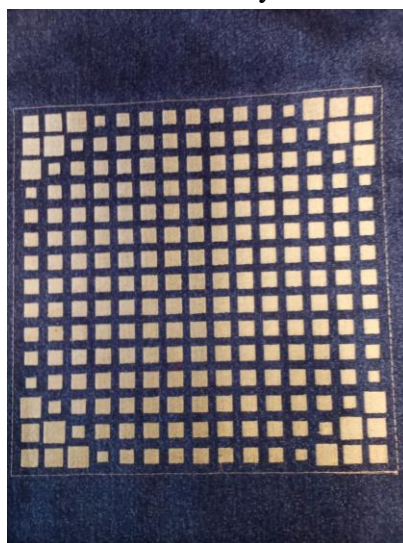
Figure 6.2. Fabricated central feed reflectarray.

Figure 6.3. Fabricated offset feed reflectarray.

Due to the unavailability of an anechoic chamber and measurement facility, a wooden setup is built to test the reflectarray. The measurement setup is shown in Figure 6.4.
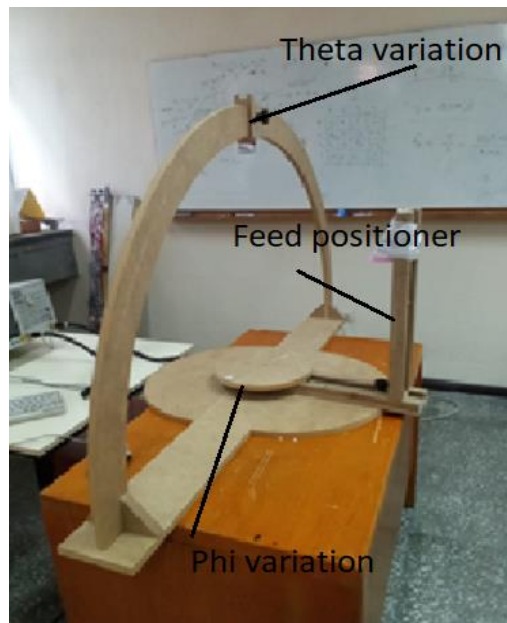
Figure 6.4. Test setup.

A moveable receiving antenna is attached with a wooden arc to measure radiation patterns along the theta axis. The arc is marked with angles ranging from -90° to 90° degrees, and measurements are taken at the difference of 10° degrees. For center feed configuration, a wooden structure is built to hold the transmitter antenna exactly above the reflectarray center. A horizontally and vertically moveable feed holder is used for offset feed configuration to adjust the feed antenna location. Bothe center feed and offset feed configuration and measured results are shown in forthcoming figures.

Figure 6.5. Measurement setup for center feed configuration.

Figure 6.5 shows the reflectarray feed antenna holder. The feed holder is made of foam material and is supported by wooden sticks. The ground plane of the antenna is made of conductive textile while a 1 mm thick foam sheet is used as a second layer instead of air. During the fabrication process, an extra 3 mm thick cotton layer is also added. The designs are re-simulated by adding an extra cotton layer and also instead of a perfect conducting layer, a low conductive layer is used. The re-simulated and measured E and H plane radiation patterns for center feed configuration are depicted in Figures 6.6-6.7.
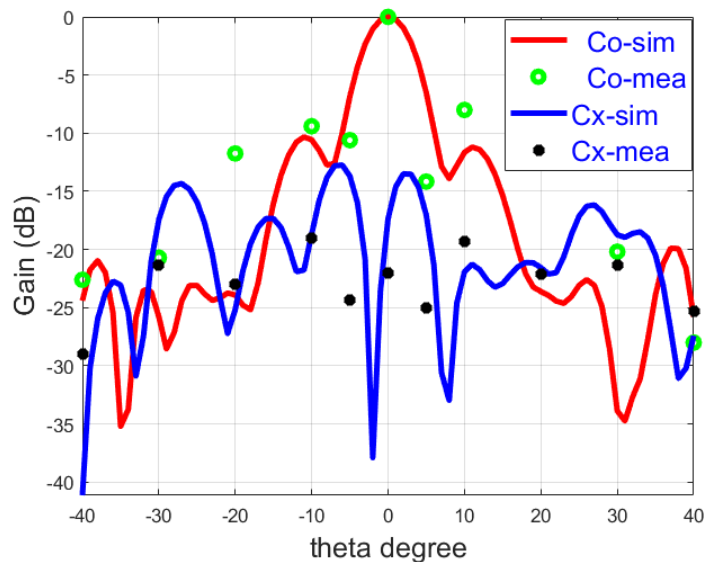
Figure 6.6. Measured E-plane radiation pattern for center feed configuration.

The solid red and blue lines represent simulated result for co and cross-polarization, while blue and black marks represent measured co and cross-polarization respectively.
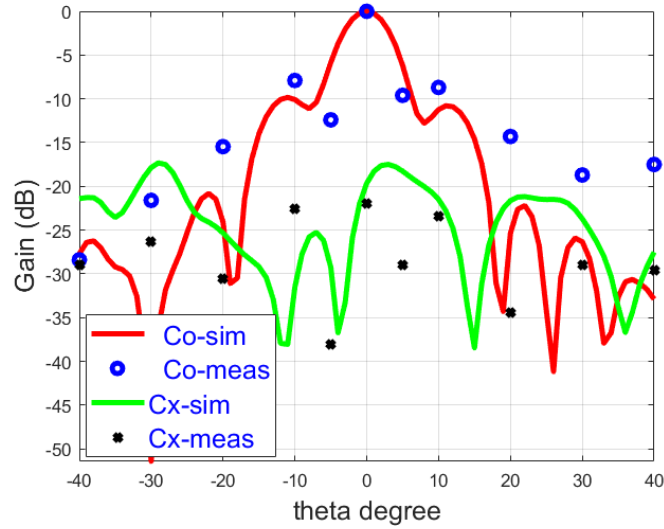
Figure 6.7. Measured H-plane radiation pattern for center feed configuration.

The solid red line represents simulated results while round blue dots are used for measured results of co-polarization similarly the green lines is used simulated while black dots are used to indicate measured cross-polarization. The cross-polarization levels for both E and H- planes are below -15 dB.

The test setup and simulated and measured results for offset feed configurations are given below.

Figure 6.8. Measurement setup for offset feed configuration.
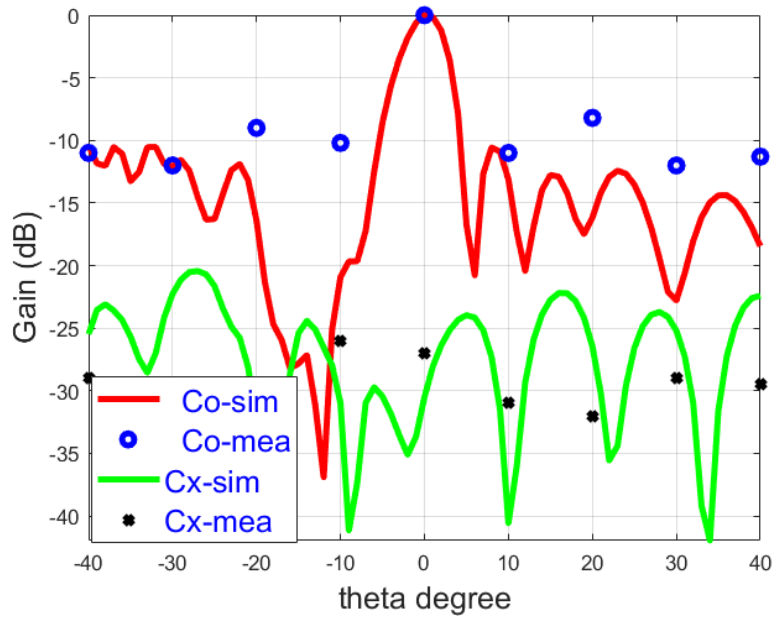
Figure 6.9. Measured E-plane radiation pattern offset feed configuration.
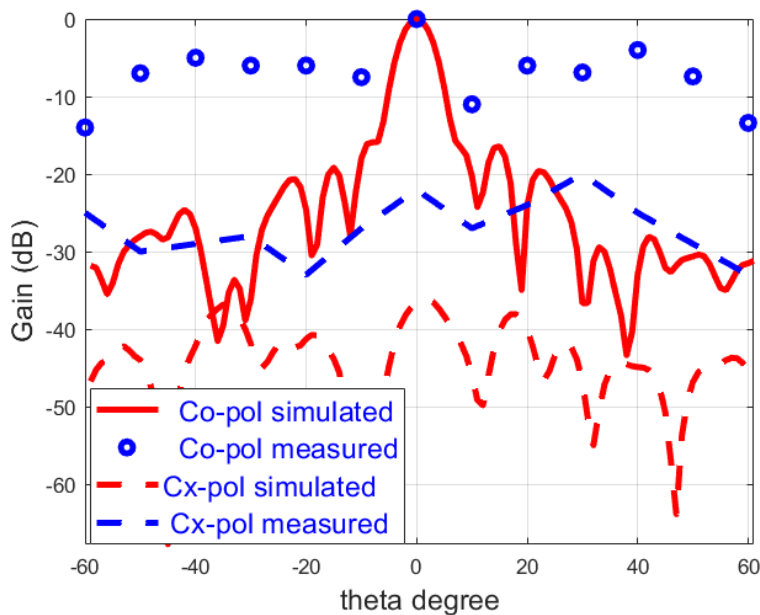
Figure 6.10. Measured H-plane radiation pattern for offset feed configuration.

Figures 6.9-6.10 show the radiation characteristics of offset feed configuration. The E-plane simulated and measured results resemble significantly but for H-plane sidelobe levels are much higher in the measured result. As it is mentioned earlier in section 3.5.1 the orientation of the thread with respect to the incident electric field is also an important factor affecting the performance of the design. During H-plane measurement E-field is not parallel to thread orientation which produced higher sidelobe levels. Another

fabrication error that results in inaccurate estimation of aperture phase distribution is the gaps between threads and improper edge finishing. These fabrication errors also contribute to low gain performance due to energy wastage. The thread orientation and effects of imperfect fabrication like the gap between threads and edge truncation are not considered during simulation, this causes some difference in simulated and measured results. By considering effects during the simulation process, improving the test setup and taking measurements in an anechoic chamber will further decrease the simulated and measured result mismatch.

7. Conclusion and Future work

7.1. Conclusion

This dissertation is about designing and analyzing antenna and passive RF circuits on a flexible substrate. The design process is broadly divided into three parts: material selection and characterization, the design simulation, and the last one is fabrication and test measurements. Two types of substrate materials, textile and, silicone-based flexible materials are investigated based on different criteria; textile material is shortlisted for design realization. Due to the merely explored area, the reflectarray topology is analyzed.

The first part is about material selection and characterization. The choice of substrate for flexible electronics is based on many factors, including weight, ease, and cost of fabrication, electric and mechanical properties. One major design challenge of these unconventional materials is determining their exact dielectric properties. Several methods have been proposed in the literature; in this work, resonant and non-resonant-based methods are used to determine the dielectric properties of cotton, jeans, PDMS, and Mold silicone Ak Sil T1310. The results of both methods are verified by measuring the dielectric properties of conventional FR4 material. The non-resonant technique is based on the transmission and reflection of electromagnetic waves from the boundary of the test material. This method is based on two different measurement techniques; the transmission line technique and the free space technique. In the resonant technique, dielectric properties are determined from the material's resonant frequency. It includes cavity resonator, dielectric resonator, stripline, and microstrip line methods. The choice of these methods depends on many factors, including frequency range, sample type, cost, and accuracy of the measuring method. The waveguide-based transmission and modified ring resonator methods are investigated. The X-band waveguide is used in the experimental setup. To minimize errors and improve measurement accuracy, the network analyzer is calibrated with Open Short Load and Through (OSLT).

In contrast, the waveguide is calibrated with Through Reflect and Line (TRL) standards. In the waveguide method, the dielectric properties of test materials are estimated from measured S-parameters by using the NRW algorithm. On the other hand, the modified ring resonator method determines dielectric properties from the 1-10 GHz frequency range. The dielectric properties are obtained from the shift in resonance frequency due to the test material.

The Textile materials do not have any standardized dielectric characterization method; their dielectric properties vary due to different structural configurations. Fabric construction, thread count, solid volume function, relative humidity, and environmental condition are the prime factor affecting the results. The textile samples cotton and jeans are investigated. Both these materials are very thin, porous, and contain a lot of air, which indicates that their dielectric must not be very high. The exact behavior of trapped air in between a textile fabric on its dielectric properties is yet to investigate; however, it is predicted that if the threads in fabric are sparsely packed, the dielectric constant will be near to one. It increases linearly for densely populated threads. The dielectric constant ε_r' of cotton calculated from NRW algorithm for X-band is 1.68, loss factor ε_r'' is 0.038, whereas, for jeans, these are 1.65 and 0.001 respectively. The dielectric properties of cotton and Jeans measured through the modified ring resonator method are $\varepsilon_r' = 1.78$, $\varepsilon_r'' = 0.02$, $\varepsilon_r' = 1.68$, and $\varepsilon_r'' = 0.011$ respectively. The two-mold silicone-based materials PDMS and AK-Sil T1310 are also studied for their dielectric properties. Both these materials have a different oxidized mixture which affects their dielectric properties. The dielectric properties of PDMS and Ak-Sil T1310 calculated through waveguide method are $\varepsilon_r' = 2.84$, $\varepsilon_r'' = 0.07$, $\varepsilon_r' = 2.67$, and $\varepsilon_r'' = 0.04$ and with modified ring resonator method are $\varepsilon_r' = 2.8$, $\varepsilon_r'' = 0.05$, $\varepsilon_r' = 2.7$, and $\varepsilon_r'' = 0.05$ respectively.

The results show good agreement with the data present in the literature. Some ambiguous peaks are observed at some frequencies. There are two prime reasons for these sharp peaks: the system and random errors, which cannot be corrected through calibration, such as the phase instability of coaxial cables due to temperature variation or mechanical bending. Usually, the phase stability of these cables for X- frequency band is around $\pm(2^\text{o} - 3^\text{o})$, which can cause significant errors in measurements. In [147] author investigates $\pm 2^\text{o}$ phase error in S_{11} phase measurement and reported substantial variation in permittivity value. A discontinuity can be observed around 9.5 GHz frequency from the S-parameter of the error box. This discontinuity propagated to estimated S-parameters of test samples and ultimately resulted in ambiguous peaks in determined dielectric parameters. The other reason is the thickness of the test sample. A known drawn back with NRW algorithm is unwanted resonance for the thickness of test sample greater than $\frac{\lambda_g}{2}$. Due to this reason, the thickness test sample should be kept lesser than $\frac{\lambda_g}{2}$. But for the very thin samples ($d<<\frac{\lambda_g}{6}$), transmission and reflection phase ambiguities arise because

there is not enough delay time to obtain proper a phase shift. The relative uncertainty in permittivity measurement against normalized thickness is presented in [148], where it can be observed that uncertainty is high in thinner samples.

After substrate characterization, the next step is to identify and characterize the conductive material. Three different conductive material and metallization methods are investigated. The method includes metallization through stitching, sewing, sticking, and screen printing using bare conductive and PVD techniques using copper nano-particles. The conducting layer must be thick enough to maintain electrical continuity to overcome surface roughness in screen printing. The bending and starching produce cracks conductively; moreover, high conductive ink increases the fabrication cost. The PVD technique requires a special fabrication facility, and normal cotton textile is not compatible with the fabrication process. In addition, the deposited particles start peeling off from the surface over time. The performance of stitching/sewing by using bare copper wire and sticking by using conductive textile and copper tape is also analyzed. The reflection transmission and absorption characteristics of the rectangular unit cell with slot fabricated through stitching and sticking on regular jeans and Tyvek fabric created by DuPont cooperation for personal protection kit are compared. Design with copper tape showed better performance than bare copper and conductive textile. The result in Figure 3.55 shows that bare copper wire and conductive textile have some resonance frequency shift and have higher return loss compared to simulated design and the design fabricated with copper tape. In the simulation, both substrate and conducting patch are planar and continuous, whereas, in reality, substrate and conductive textile are rough, porous, and contain air between gaps. While fabrication with copper wire using stitching also causes air gaps, resulting in resonance frequency shift and increased return loss. These air gapes become more significant for higher frequencies. Besides these degrading air gap effects, conductive textile and bear copper thread showed satisfactory performance. Moreover, it is also observed that bare copper and conductive textile also have absorption behavior. Based on performance analysis and the possibility of utilizing already available market resources for fabrication, the computerized embroidery technique is selected for design fabrication.

The second section of the thesis is about antenna and passive component simulation and design. An X- band reflectarray on the textile substrate is investigated. The reflectarray simulation consists of two stages. One is element-level analysis, and the other is system-

level analysis. In Element level investigation Floquet port analysis method is used to obtain phase characteristics. Two type of element single layer and two-layer unit cells are analyzed. The two-layer unit cell showed better reflection and phase response and is chosen further for system-level analysis. Two array configurations, the center feed, and the offset feed are simulated, and their efficiency and gain performance are observed. The 256.5×256.5 reflectarray consists of 15×15 elements illuminated through a horn antenna situated 385 mm above the reflectarray geometric center. The calculated efficiency for given feed coordinates and array dimensions is 43%. The design has approximately 15 dB gain with 6° degree 3 dB beamwidth. The offset feed configuration array consists of 17×17 elements resulting in the size 290.7×290.7 mm. The feed is placed 230 mm on the horizontal axis and 380 mm on the vertical axis away from the geometric center of the reflectarray. The calculated efficiency is around 45%, the gain is around 21 dB, whereas the 3 dB beamwidth is about 6° degrees.

 Design for both center and offset feed are fabricated using computerized embroidery, and their test results are obtained. Design for both center and offset feed are fabricated using computerized embroidery, and their test results are obtained. The most critical factors that affect the test result are fabrication errors and unavailability of the anechoic chamber. The measurements are taken in an open environment; reflection from the surrounding environment results in high sidelobe levels. The conductivity and size of the thread, stitching density, and direction limit the performance of the fabricated design. The air gap between conductive threads on both patch and ground plane causes discontinuity in material parameters, making the material inhomogeneous. Previous research mentions the incident energy leak through these air gapes during this research as depicted from the figure shows that the absorption is more prominent than the transmission [149]. This absorption and leakage phenomena reduce the reflecting capability of the fabricated design and result in low gain performance. Moreover, the thread alignment with the incident electric field also phenomenally affects the results. These all factors affect the gain characteristic of reflectarray and are needed thorough investigation to overcome them.

7.2. Future Work

The future work for this dissertation can be divided into short term and long term. The short-term goals include investigating convex and concave bending effects on reflectarray performance. The long-term goals include a detailed analysis of computerized

embroidery performance degrading factors, proposing viable solutions to mitigate factors, and designing more complicated patch geometries using automated embroidery techniques. Meanwhile, also exploring other alternative fabrication techniques for the flexible substrate.

8. References

[1]   Flexible Electronics Market Size Worth Around US$ 61 Bn by 2030. Precedence Research published on December 16 2021, Available on: https://www.globenewswire.com/news-release/2021/12/16/2353637/0/en/Flexible-Electronics-Market-Size-Worth-Around-US-61-Bn-by-2030.html.

[2]   P. Salonen, J. Kim, and Y. R. Samii. "Dual-band E-shaped patch wearable textile antenna." *Antennas and Propagation Society International Symposium*, vol. 1. IEEE, 2005.

[3]   A. Rida, L. Yang, R. Vyas, and M. M. Tentzeris, "Conductive inkjet-printed antennas on flexible low-cost paper-based substrates for RFID and WSN applications," *IEEE Antennas and Propagation Magazine*, vol. 51, no. 3, pp. 3-23, 2009.

[4]   D. E. Anagnostou, A. A. Gheethan, A. K. Amert, and K. W. Whites, "A direct-write printed antenna on paper-based organic substrate for flexible displays and WLAN applications," *Journal of Display Technology*, vol. 6, no.11, pp. 558-564, 2010.

[5]   M. Kubo, X. Li, C. Kim, M. Hashimoto, B. J. Wiley, D. Ham, and G. M. Whitesides, "Stretchable microfluidic radiofrequency antennas". *Advanced Materials*, vol. 22, no. 25, pp. 2749-2752, 2010.

[6]   X. Huang, T. Leng, K. H. Chang, J. C. Chen, K. S. Novoselov, and Z. Hu, "Graphene radio frequency and microwave passive components for low cost wearable electronics". *2D Materials*, vol. 3, no. 2, pp. 025021, 2016.

[7]   K. Futera, K. Kielbasinski, A. Młozniak, and M. Jakubowska, "Inkjet printed microwave circuits on flexible substrates using heterophase graphene-based inks." Soldering & Surface Mount Technology, vol. 27, no .3, pp.112-114, 2015.

[8]   H. R. Khaleel, H. M. Al-Rizzo, D. G. Rucker, and Y. Al-Naiemy, "Flexible printed monopole antennas for WLAN applications." *Antennas and Propagation (APSURSI), 2011 IEEE International Symposium*, pp. 1334-1337, 2011.

[9]   X. Huang, T. Leng, M. Zhu, X. Zhang, J. Chen, K. Chang, and Z. Hu "Highly flexible and conductive printed graphene for wireless wearable

communications applications," *Scientific Reports*, vol. 5, no. 1, pp. 1-8, 2015.

[10]   S. Asif, A. Iftikhar, S.Z. Sajal, B. Braaten, and M. S. Khan, "On using graphene-based conductors as transmission lines for feed networks in printed antenna arrays". *2015 IEEE International Conference on Electro/Information Technology (EIT),* pp. 681-683. IEEE 2015.

[11]   Z. Ma, Y. H. Jung, J. H. Seo, J. Lee, S. J. Cho, T. H Chang, and W. Zhou, "Radio-frequency flexible and stretchable electronics (Key note)," in *2016 China Semiconductor Technology International Conference (CSTIC)*, pp. 1-4. IEEE March 2016.

 [12]   W. Zhu, S. Park, M. N. Yogeesh, and D. Akinwande, "Advancements in 2D flexible nanoelectronics: From material perspectives to RF applications". *Flexible and Printed Electronics*, vol. 2, no. 4, pp. 043001, 2017.

[13]   Y. Mahe, A. Chousseaud, M. Brunet, and B. Froppier, "New flexible medical compact antenna: design and analysis". *International Journal of Antennas and Propagation*, 2012.

[14]   S. Shrestha, M. Agarwal, P. Ghane, and K. Varahramyan, "Flexible microstrip antenna for skin contact application*," International Journal of Antennas and Propagation*, 2012.

[15]   K. Short, and D. V. Buren., Printable Spacecraft: Flexible Electronic Platforms for NASA Missions. Phase One. 2012.

[16]   H. R. Khaleel, H. M. Al-Rizzo, and A. I. Abbos, "Design, fabrication, and testing of flexible antennas." in *Advancement in Microstrip Antennas with Recent Applications*, A. Kishk, Ed. InTech, Coratia, pp. 363-383, 2013.

[17]   J. G. Hester, S. Kim, J. Bito, T. Le, J. Kimionis, D. Revier, and M. M. Tentzeris, "Additively manufactured nanotechnology and origami-enabled flexible microwave electronics." *Proceedings of the IEEE*, vol. 103 no. 4, pp. 583-606, 2015.

[18]   D. Lawrence, J. Kohler, B. Brolklier T. Claypole, T. BurginKatz, J. Veinot, "Manufacturing Platforms for Printing Organic Circuits." in Printed Organic and Molecular Electronics, DR Gamota, P. Brazis, K. Kalyansundaram and J. Zhang. ed., Springer, USA pp. 307-318,2004.

[19]   N. J. Kirsch, N. A. Vacirca, E. E. Plowman, T. P. Kurzweg, A. K. Fontecchio, and K. R. Dandekar, "Optically transparent conductive polymer RFID meandering dipole antenna," *2009 IEEE International Conference on RFID.*

IEEE, 2009.

[20]   S. Y. Leung, and D.C Lam, "Performance of printed polymer-based RFID antenna on curvilinear surface." *IEEE Transactions on Electronics Packaging Manufacturing*, vol. 30, no. 3 pp. 200-205, 2007.

[21]   S. H. Eom, and S. Lim, "based pattern switchable antenna using inkjet-printing technology." *Microwave Conference (APMC), 2015 Asia-Pacific*. Vol. 1. IEEE, 2015.

[22]   H. Subbaraman, D.T. Pham, X. Xu, M.Y. Chen, A. Hosseini, X. Lu, R.T. Chen, "Inkjet-printed two-dimensional phased-array antenna on a flexible substrate." *IEEE Antennas and Wireless Propagation Letters*, vol. 12, pp. 170-173, 2013.

[23]   Y. Li, Z. Zhang, Z. Feng, and H. R. Khaleel, "Fabrication and Measurement Techniques of Wearable and Flexible Antennas." WIT Transactions on State-of-the-art in Science and Engineering, vol. 82, pp. 7-23, 2014.

[24]   L. F. Chen, C. K. Ong, C. P. Neo, V. V. Varadan, and V. K. Varadan, Microwave electronics: measurement and materials characterization. John Wiley & Sons, USA 2004.

[25]   D. M. Pozar. "Microwave engineering." Wiley, USA. 2012.

[26]   M. S. Venkatesh, and G. S. V. Raghavan. "An overview of dielectric properties measuring techniques." *Canadian biosystems engineering*, vol. 47 no. 7 pp. 15-30, 2005.

[27]   M. T. Khan, and S.M. Ali. "A brief review of measuring techniques for characterization of dielectric materials." International Journal of Information Technology and Electrical Engineering, vol. 1, no .1, 2012.

[28]   U. Kaatze. "Measuring the dielectric properties of materials. Ninety-year development from low frequency techniques to broadband spectroscopy and high-frequency imaging." *Measurement Science and Technology*, vol. 24, no .1, pp. 012005, 2012.

[29]   J. W. Stewart, and M. J. Havrilla. "Electromagnetic characterization of a magnetic material using an open-ended waveguide probe and a rigorous full-wave multimode model." *Journal of Electromagnetic Waves and Applications*, vol. 20, no. 14, pp. 2037-2052, 2006.

[30]   R. A. Fenner, E. J. Rothwell, and L. L. Frasch. "A comprehensive analysis

of free-space and guided-wave techniques for extracting the permeability and permittivity of materials using reflection-only measurements." *Radio Science*, vol. 47, no. 01, pp. 1-13, 2012.

[31]   A. A. Barba, and M. d'Amore. "Relevance of dielectric properties in microwave assisted processes." *in Microwave materials characterization*, S. Constanzo, Ed. InTech, Croatia, pp. 91-118, 2012.

[32]   F. Costa, M. Borgese, M. Degiorgi, and A. Monorchio, "Electromagnetic Characterization of Materials by Using Transmission/Reflection (T/R) Devices." *Electronics*, vol. 6, no. 4, pp. 95, 2017.

[33]   F. J. F. Gonçalves, A. G. Pinto, R. C. Mesquita, E. J. Silva, and A. Brancaccio, "Free-Space Materials Characterization by Reflection and Transmission Measurements using Frequency-by-Frequency and Multi-Frequency Algorithms." *Electronics*, vol. 7, no.10, pp. 260, 2018.

[34]   C. P. L Rubinger, and L. C. Costa, "Building a resonant cavity for the measurement of microwave dielectric permittivity of high loss materials." *Microwave and Optical Technology Letters*, vol. 49, no. 7, pp. 1687-1690, 2007.

[35]   H. C. García, "New methods for determining the complex permittivity of different glucose concentrations by waveguide and antenna measurements at v-band." Master thesis, King's College London, 2013.

[36]   Y. H. Chou, M. J. Jeng, Y. H. Lee, and Y. G. Jan, "Measurement of RF PCB dielectric properties and losses." *Progress in Electromagnetics Research*, vol. 4, pp. 139-148, 2008.

[37]   K. P. Ray, K. Nirmala, and S. Hosabettu. "Simple accurate method to determine dielectric constant of the substrate." *2009 Applied Electromagnetics Conference (AEMC)*, IEEE, 2009.

[38]   S. B. Cohn, and K. C. Kelly, "Microwave measurement of high-dielectric-constant materials". *IEEE Transactions on Microwave Theory and Techniques*, vol. 14, no. 9, pp. 406-410, 1966.

[39]   J. Krupka, R. G. Geyer, Krupka, M. Kuhn, and J. Hinken, "Dielectric Properties of Single Crystals of Al2O3, LaAlO3, NdGaO3, SrTiO3, and MgO at Cryogenic Temperatures." *IEEE Transactions on Microwave Theory and Techniques,* vol. 4, no. 10, pp. 1886-1890, 1994.

[40]   R. G. Geyer, and J. Krupka, "Microwave dielectric properties of anisotropic materials at cryogenic temperatures." *IEEE Transactions on*

Instrumentation and Measurement. vol. 44, no. 2, 329-331,1995.

[41]   M. N. Afsar, X. Li, and H. Chi, "An automated 60 GHz open resonator system for precision dielectric measurements". *IEEE Transactions on Microwave Theory and Techniques*, vol. 38, no. 12, pp. 1845-1853, 1990.

[42]   Note, Agilent Application. "Agilent basics of measuring the dielectric properties of materials." Agilent literature number, 2006.

[43]   K. W. Allen, M. M. Scott, D. R. Reid, J. A. Bean, J. D. Ellis, A. P. Morris, and J. M. Marsh, "An X-band waveguide measurement technique for the accurate characterization of materials with low dielectric loss permittivity." *Review of Scientific Instruments*, vol. 87, no. 5, pp. 054703, 2016.

[44]   D. Ballo. Network Analyzer Basic, Hewlett Packard Company, Santa Rosa, CA.

[45]   K. Y. You, K.Y., and K. Goudos Sotirios. "Materials characterization using microwave waveguide system." Microwave Systems and Applications. InTech, Coratia, pp. 341-358, 2017.

[46]   A. M. Nicolson, and G. F. Ross, "Measurement of the intrinsic properties of materials by time-domain techniques." *IEEE Transactions on instrumentation and measurement*, vol. 19, no. 4, pp. 377-382, 1970.

[47]   W. B Weir. "Automatic measurement of complex dielectric constant and permeability at microwave frequencies." Proceedings of the IEEE, vol. 62, no.1, pp. 33-36, 1974.

[48]   C. Tsipogiannis. "Microwave materials characterization using waveguides and coaxial probe," Master dissertation, Lund University, Sweden, 2012.

[49]   V. S. Yadav, D. K. Sahu, Y. Singh, M. Kumar, and D. C. Dhubkarya, "Frequency and temperature dependence of dielectric properties of pure poly vinylidene fluoride (PVDF) thin films." *AIP Conference Proceedings*. vol. 1285. no. 1, 2010.

[50]   A. Elrashidi, K. Elleithy, and H. Bajwa, "Resonance Frequency, Gain, Efficiency and Quality Factor of a Microstrip Printed Antenna as a Function of Curvature for TM01 mode Using Different Substrates." *Journal of Wireless Networking and Communications*, vol. 1, pp. 1-8, 2011.

[51]   B. Ravelo, A. Thakur, A. Saini, and P. Thakur, "Microstrip Dielectric Substrate Material Characterization with Temperature Effect." *Applied Computational Electromagnetics Society Journal*, vol. 30, no.12, 2015.

[52]   R. Gonçalves, R. Magueta, P. Pinho, and N. B. Carvalho, "Dissipation Factor and Permittivity Estimation of Dielectric Substrates Using a Single Microstrip Line Measurement." *Applied Computational Electromagnetics Society Journal*, vol. 31, no. 2, 2016.

[53]   J. Paleček, M. Vestenický, P. Vestenický, and J. Spalek, "Frequency Dependence Examination of PCB Material FR4 Relative Permittivity." *IFAC Proceedings*, vol. 46, no. 28, pp. 90-94, 2013.

[54]   T. Rovensky, A. Pietrikova, I. Vehec, and M. Kmec, "Measuring of dielectric properties by microstrip resonators in the GHz frequency." *2015 38th International Spring Seminar on Electronics Technology (ISSE)*, IEEE, 2015.

[55]   H. I. Azeez, W. S. Chen, C. K. Wu, C. M. Cheng, and H. C. Yang, "A Simple Resonance Method to Investigate Dielectric Constant of Low Loss Substrates for Smart Clothing." *Sensors and Materials*, vol. 30, no. 3, pp. 595-608, 2018.

[56]   P. Troughton, "Measurement techniques in microstrip." *Electronics letters*, vol. 5, no. 2, pp. 25-26, 1969.

[57]   B. Jackson, and T. Jayanthy. "Measurement of complex permittivity using planar resonator sensor." *IOSR J. Electron. Commun. Eng version I.* vol. 9, no.1, pp. 2278-8735, 2014.

[58]   A. K. Verma, and A. S. Omar. "Microstrip resonator sensors for determination of complex permittivity of materials in sheet, liquid and paste forms." *IEE Proceedings-Microwaves, Antennas and Propagation*, vol. 152, no. 1, pp. 47-54, 2005.

[59]   J. M. Heinola, P. Silventoinen, K. Latti, M. Kettunen, and J. P. Strom, "Determination of dielectric constant and dissipation factor of a printed circuit board material using a microstrip ring resonator structure." *15th International Conference on Microwaves, Radar and Wireless Communications (IEEE Cat. No. 04EX824)*, vol. 1, 2004.

[60]   A. Rashidian, M. T. Aligodarz and D. M. Klymyshyn, "Dielectric characterization of materials using a modified microstrip ring resonator technique," *IEEE Transactions on Dielectrics and Electrical Insulation*, vol. 19, no. 4, pp. 1392-1399, 2012.

[61]   J. Svacina, "Analysis of multilayer microstrip lines by a conformal mapping method." *IEEE Transactions on Microwave Theory and Techniques*, vol.

40, no. 4, pp. 769-772, 1992.

[62]   S. Sankaralingam, and B. Gupta. "Determination of dielectric constant of fabric materials and their use as substrates for design and development of antennas for wearable applications." *IEEE Transactions on Instrumentation and Measurement*, vol. 59, no.12, pp. 3122-3130, 2010.

[63]   Material Property Database PDMS,
 Available: http://www.mit.edu/~6.777/matprops/pdms.htm.

[64]   Silicone Rubber, Available:
 https://www.azom.com/properties.aspx?ArticleID=920.

[65]   A Definition of FR-4, Available:
 http://www.ieee802.org/3/ap/public/may04/2

[66]   D. Numakura, "Advanced Screen Printing "Practical Approaches for Printable & Flexible Electronics," *3rd Intl Microsystem, Packaging Assembly and Circuits Technology Conference*, pp. 205 – 208, 2008

[67]   H. Berg, M. Schubert, S. Friedrich and K. Bock, "Screen printed conductive pastes for biomedical electronics," *39th Intl Spring Seminar on Electronics Technology (ISSE)*, pp. 1-6, 2016.

[68]   D. Mercier, J. P. Michel, J. Chautagnat, C. Baret, C. Bonnard, H. Sibuet, C. Billard, M. Benwadih, O. Haon, R. Coppard and J. Y. Laurent, "Screen printed lumped element filters based on silver nanoparticle ink." *47th European Microwave Conference (EuMC)*, pp. 176-179, 2017.

[69]   M. Dressler, T. Studnitzky and B. Kieback, "Additive manufacturing using 3D screen printing." *International Conference on Electromagnetics in Advanced Applications (ICEAA)*, pp. 476 – 478, 2017.

[70]   M. Jakubowska, S. Achmatowicza, V. Baltrusaitisa, A. Moizniaka, I. Wyzkiewicza and E. Zwierkowskaa, "Investigation on a new silver photoimageeable conductor," *Microelectronic Realibility*, vol. 48, no. 6, pp. 860-865, 2008.

[71]   S. Muckett and J. Minalgene, "Hibridas photoimageable think film process and materials for microwave and sensor component applications*, 2nd IEMT.IMC Symp*, pp. 154-160, 1998.

[72]   S. D. Park, M. J. Yoo, N. K. Kanf, J. C. Park, L. K. Lim and D. K. Kim, "Fabrication of photoimageable silver paste for low temperature cofiring using acrylic binder polymers and photosensitive materials," *Macromolecular*

Research, vol. 12, no. 4, pp. 391-398, 2004.

[73]   W. Su, B. S. Cook, M. M. Tentzeris, "Low-Cost Microfluidics-Enabled Tunable Loop Antenna Using Inkjet-Printing Technologies," *9th European Conference. on Antenna and Propagation*, 2015.

[74]   H. Ibili and Ö. Ergül, "Very low-cost inkjet-printed metamaterials: Progress and challenges," IEEE MTT-S International Microwave Workshop Series on Advanced Materials and Processes for RF and THz Applications (IMWS-AMP), 2017.

[75]   M. Tursunniyaz and R. Baktur, "Inkjet printing of antennas on glass or solar cells," *IEEE International Symposium on Antennas and Propagation & USNC/URSI National Radio Science Meeting*, pp. 865 – 866, 2017.

[76]   D. Lawrence, J. Kohler, B. Brolklier T. Claypole, T. BurginKatz, J. Veinot, "Manufacturing Platforms for Printing Organic Circuits." in Printed Organic and Molecular Electronics, DR Gamota, P. Brazis, K. Kalyansundaram and J. Zhang. ed., Springer, USA, pp. 320-321, 2004.

[77]   Berry, D., R. Malech, and W. Kennedy. "The reflectarray antenna." *IEEE Transactions on Antennas and Propagation*, vol. 11, no. 6, pp. 645-651, 1963.

[78]   Phelan, H. Richard. "Spiraphase reflectarray for multitarget radar." Microwave Journal vol. 20, pp. 67, 1977.

[79]   C. S. Malagisi, "Microstrip disc element reflect array." *EASCON'78; Electronics and Aerospace Systems Convention*, 1978.

[80]   J. P. Montgomery, "A microstrip reflectarray antenna element." in *Antenna Applications Symposium,* 1978.

[81]   E. Öztürk, and B. Saka, "Double orthogonal phase stubs technique for Minkowski fractal reflectarray antenna. *Journal of Electromagnetic Waves and Applications*, vol.33, no. 5, pp. 601-611, 2019.

[82]   Huang, John. "Microstrip reflectarray." *Antennas and Propagation Society Symposium 1991 Digest*, IEEE, 1991.

[83]   T. A. Metzler. Design and analysis of a microstrip reflectarray. PhD Thesis, University of Massachusetts Amherst, 1993.

[84]   Y. Zhuang, K. L. Wu, C. Wu, and J. Litva. "Microstrip reflectarrays: Full-wave analysis and design scheme." *In Proceedings of IEEE Antennas and Propagation Society International Symposium*, IEEE, pp. 1386-1389, 1993.

[85]   R. D. Javor, X-D. Wu, and K. Chang. "Beam steering of a microstrip flat

reflectarray antenna." *Proceedings of IEEE Antennas and Propagation Society International Symposium and URSI National Radio Science Meeting*. vol. 2. IEEE, 1994.

[86]   D-C. Chang, and M.-C. Huang. "Multiple-polarization microstrip reflectarray antenna with high efficiency and low cross-polarization." *IEEE Transactions on Antennas and Propagation*, vol. 43 no.8, pp. 829-834, 1995.

[87]   A. Kelkar, "FLAPS: conformal phased reflecting surfaces." *Proceedings of the 1991 IEEE National Radar Conference*. IEEE, 1991.

[88]   D. M. Pozar, and T. A. Metzler. "Analysis of a reflectarray antenna using microstrip patches of variable size." *Electronics Letters*, vol. 29, no.8 pp. 657-658, 1993.

[89]   David M. Pozar, Stephen D. Targonski, and H. D. Syrigos. "Design of millimeter wave microstrip reflectarrays." *IEEE Transactions on Antennas and Propagation*, vol. 45 no. 2, pp. 287-29, 1997.

[90]   K. Y. Sze, and L. Shafal. "Analysis of phase variation due to varying patch length in a microstrip reflectarray." *IEEE Antennas and Propagation Society International Symposium. 1998 Digest. Antennas: Gateways to the Global Network. Held in conjunction with: USNC/URSI National Radio Science Meeting (Cat. No. 98CH36)*. vol. 2. IEEE, 1998.

[91]   J. Huang, "Bandwidth study of microstrip reflectarray and a novel phased reflectarray concept." *IEEE Antennas and Propagation Society International Symposium. 1995 Digest*. vol. 1. IEEE, 1995.

[92]   J. Huang, and R. J. Pogorzelski. "Microstrip reflectarray with elements having variable rotation angles." *IEEE Antennas and Propagation Society International Symposium 1997. Digest*. vol. 2. IEEE, 1997.

[93]   A. W. Rudge, and A. A. Nurdin, "Offset-parabolic-reflector antennas: A review." *Proceedings of the IEEE*, vol. 66 no.12, pp.1592-1618, 1978.

[94]   Johansson, F. Stefan. "A new planar grating-reflector antenna.*" IEEE transactions on antennas and propagation*, vol. 38, no.9, pp. 1491-1495, 1990.

[95]   E. Ozturk, "X-Bantta minkowski yansıtıcs dizi anten analiz ve tasarımı." Ph.D. Thesis, Hacettepe University, Ankara, Turkey 2018.

[96]   A. A. Tolkachev, V. V. Denisenko, A. V. Shishlov, and A. G. Shubov, "High gain antenna systems for millimeter wave radars with combined electronical and mechanical beam steering." *Proceedings of International*

Symposium on Phased Array Systems and Technology, IEEE, 1996.

[97] Colin, J-M. "Phased array radars in France: Present and future." *Proceedings of International Symposium on Phased Array Systems and Technology*. IEEE, 1996.

[98] E. Carrasco, B. Mariano and J. A. Encinar. "Reflectarray element based on aperture-coupled patches with slots and lines of variable length.*" IEEE Transactions on Antennas and Propagation*, vol. 55, no.3, pp. 820-825, 2007.

[99] R. Mathieu, and J-J. Laurin. "Design of an electronically beam scanning reflectarray using aperture-coupled elements." *IEEE Transactions on Antennas and Propagation*, vol. 55, no.5, pp. 1260-1266, 2007.

[100] M. E. Bialkowski, and J. A. Encinar. "Reflectarrays: Potentials and challenges." *2007 International Conference on Electromagnetics in Advanced Applications*. IEEE, 2007.

[101] T-N. Chang, and C-S. Chu. "Cross-polarisation level of reflectarray with gapped ring elements." *Electronics Letters*, vol. 43, no.5, pp. 1-2, 2007.

[102] M. Ramli, A. N. Selamat, N. Misran, M. F. Mansor, and M. T. Islam, "Superposition of reflectarray elements for beam scanning with phase range enhancement and loss improvement." *ARPN Journal of Engineering and Applied Sciences*, vol. 11, no. 3, pp. 1755-1758, 2016.

[103] M. Y. Ismail, W. Hu, R. Cahill, V. F. Fusco, H. S. Gamble, D. Linton, and N. Grant, "Phase agile reflectarray cells based on liquid crystals." *IET Microwaves, Antennas & Propagation*, vol. 1, no.4, pp. 809-814, 2007.

[104] Malik, H. I., Ismail, M. Y., Adnan, S., Masrol, S. R., & Nafarizal, N. "A wideband reflectarray antenna based on organic substrate materials." *Telkomnika*, vol. 17, no.1, 2019.

[105] P. Nayeri, M. Liang, R. A. Sabory-Garcı, M. Tuo, F. Yang, M. Gehm, and A. Z. Elsherbeni, "3D printed dielectric reflectarrays: Low-cost high-gain antennas at sub-millimeter waves." *IEEE Transactions on Antennas and Propagation*, vol. 62, no. 4, pp. 2000-2008, 2014.

[106] H. B. Van, P. Pirinoli, M. Orefice, and F. Yang, "Wideband conformal reflectarrays: preliminary analysis." *2014 International Conference on Electromagnetics in Advanced Applications (ICEAA)*. IEEE, pp. 842-843, 2014.

[107] H. Fang, U. Quijano, K. Knarr, J. Huang, and R. Lovick, "Experimental and analytical studies of a large in-space deployable dual-band membrane

reflectarray antenna." *The Interplanetary Network Progress Report*, vol. 42, pp. 169, 2007.

[108]   C. Han, J. Huang, and K. Chang. "A high efficiency offset-fed X/Ka-dual-band reflectarray using thin membranes." *IEEE Transactions on Antennas and Propagation*, vol. 53, no.9, pp. 2792-2798, 2005.

[109]   X. Yang, H. Li, J. Zhao, and G. Yan, "A Single-Layer High-Efficiency Broadband Reflectarray Antenna Using Thin Membrane." *2018 International Applied Computational Electromagnetics Society Symposium-China (ACES).* IEEE, 2018.

[110]   "DARPA prototype reflectarray antenna offers high performance in small package", Available at:

https://www.intelligent-aerospace.com/satcom/article/16543450/darpa-prototype-reflectarray-antenna-offers-high-performance-in-small-package

[111]   M. M., Tahseen, and A. A. Kishk, "Practical investigation of different possible textile unit cell for a c-band portable textile reflectarray using conductive thread." *Progress in Electromagnetics Research*, vol. 66, pp. 15-29, 2016.

[112]   M. M., Tahseen, and A. A. Kishk, "Flexible and portable textile-reflectarray backed by frequency selective surface." *IEEE Antennas and Wireless Propagation Letters*, vol. 17, no.1, pp. 46-49, 2017.

[113]   M. M. Tahseen, and A. A. Kishk, "C-band linearly polarised textile-reflectarray (TRA) using conductive thread." *IET Microwaves, Antennas & Propagation*, vol. 11, no.7, pp. 982-989. 2017.

[114]   H. Mosallaei, and K. Sarabandi, "Antenna miniaturization and bandwidth enhancement using a reactive impedance substrate." *IEEE Transactions on Antennas and Propagation*, vol. 52, no.9, pp. 2403-2414, 2004.

[115]   H. Rajagopalan, and Y. Rahmat-Samii. "On the reflection characteristics of a reflectarray element with low-loss and high-loss substrates." *IEEE Antennas and Propagation Magazine*, vol. 52, no. 4, pp. 73-89, 2010.

[116]   A. K. Bhattacharyya. "Phased array antennas." Floquet analysis, synthesis, BFNs, and active array systems. A John Wiley &Sons, Inc., Publication, 2006.

[117]   S. D. Targonski, and D. M. Pozar, "Analysis and design of a microstrip reflectarray using patches of variable size." *Proceedings of IEEE Antennas and Propagation Society International Symposium and URSI National Radio Science*

Meeting, vol. 3. IEEE, 1994.

[118]   D. M. Pozar, "Microstrip reflectarrays myths and realities," *JINA 2004, International Symposium on Antennas, Nice, France*, pp. 175–179, November 2004.

[119]   T. Metzler, and D. Schaubert. "Scattering from a stub loaded microstrip antenna." *Digest on Antennas and Propagation Society International Symposium*, IEEE, 1989.

[120]   Y. Zhuang, K. L. Wu, C. Wu, and J. Litva, "Microstrip reflectarrays: Full-wave analysis and design scheme." *Proceedings of IEEE Antennas and Propagation Society International Symposium*. IEEE, 1993.

[121]   Y. Zhuang, J. Litva, C. Wu, and K. L. Wu, "Modelling studies of microstrip reflectarrays." *IEE Proceedings-Microwaves, Antennas and Propagation.* vol. 142, no.1, pp. 78-80, 1995.

[122]   D. Cadoret, A. Laisne, M. Milon, R. Gillard, and H. Legay, "FDTD analysis of reflectarray radiating cells." *IEEE/ACES International Conference on Wireless Communications and Applied Computational Electromagnetics*, 2005 IEEE, pp. 853-856. 2005.

[123]   D. M. Pozar and D. H. Schaubert. "Analysis of an infinite array of rectangular microstrip patches with idealized probe feeds." *IEEE Transactions on Antennas and Propagation,* vol. 32, pp. 1101-1107, 1984.

[124]   D. M. Pozar. "Analysis of an infinite phased array of aperture coupled microstrip patches." *IEEE Transactions on Antennas and Propagation*, vol. 37 no.4, pp. 418-425, 1989.

[125]   R. Mittra, H. C. Chan, and T. Cwik. "Techniques for analyzing frequency selective surfaces-a review." *Proceedings of the IEEE*, vol. 76 no.12, pp. 1593-1615, 1988.

[126]   C. Wan, and J. A. Encinar, "Efficient computation of generalized scattering matrix for analyzing multilayered periodic structures.*" IEEE Transactions on Antennas and Propagation*, vol. 43 no. 11, pp. 1233-1242.

[126]   I. Bardi, R. Remski, D. Perry, and Z. Cendes, "Plane wave scattering from frequency-selective surfaces by the finite-element method." *IEEE Transactions on Magnetics*, vol. 38 no. 2, pp. 641-644, 2002.

[127]   P. Harms, R. Mittra, and K. Wai. "Implementation of the periodic boundary condition in the finite-difference time-domain algorithm for FSS

structures." *IEEE Transactions on Antennas and Propagation*, vol. 42 no.9, pp. 1317-1324, 1994.

[128]   M. Lambea, M. A. Gonzalez, J. A. Encinar, and J. Zapata, "Analysis of frequency selective surfaces with arbitrarily shaped apertures by finite element method and generalized scattering matrix*." IEEE Antennas and Propagation Society International Symposium. 1995 Digest,* vol. 3, IEEE, 1995.

[129]   P. Hannan, and M. Balfour. "Simulation of a phased-array antenna in waveguide." *IEEE transactions on Antennas and Propagation*, vol. 13 no.3 pp. 342-353, 1965.

[130]   H. Mosallaei, and K. Sarabandi. "Antenna miniaturization and bandwidth enhancement using a reactive impedance substrate." *IEEE Transactions on Antennas and Propagation*, vol. 52, no. 9, pp. 2403-2414, 2004.

 [131]   E. Carrasco, J. A. Encinar, and M. Barba. "Wideband reflectarray antenna using true-time delay lines." *2nd European Conference on Antennas and Propagation (EuCAP 2007)*, pp. 8-8, 2007.

[132]   P. Nayeri, Y. Fan, and A. Z. Elsherbeni. Reflectarray Antennas: Theory, Designs, and Applications. John Wiley & Sons, 2018, pp.74.

[133]   J. A. Encinar, "Design of two-layer printed reflectarrays using patches of variable size." *IEEE Transactions on Antennas and Propagation*, vol. 49, no.10 pp. 1403-1410, 2001.

 [134] M. E. Bialkowski and K. H. Sayidmarie, "Investigations into phase characteristics of a single layer reflectarray employing patch or ring elements of variable size." *IEEE Trans. Antennas and Propagation*, vol. 56, no. 11, pp. 3366–3372, 2008.

[135]   K-C. Chen, C. K. Tzuang and J. Huang, "A higher-order microstrip reflectarray at Ka-band," *IEEE Antennas and Propagation Society International Symposium. 2001 Digest. Held in conjunction with: USNC/URSI National Radio Science Meeting (Cat. No.01CH37229)*, vol.3, pp. 566-569, 2001,
doi: 10.1109/APS.2001.960160.

[136]   Shaker, Jafar, Mohammad Reza Chaharmir, and Jonathan Ethier. Reflectarray antennas: analysis, design, fabrication, and measurement. Artech House, 2013.

[137]   J. Huang, and R. J. Pogorzelski. "A Ka-band microstrip reflectarray with elements having variable rotation angles." *IEEE Transactions on Antennas and*

Propagation, vol. 46 no. 5, pp. 650-656, 1998.

[138]   E. Ozturk and B. Saka, "Multilayer Minkowski Reflectarray Antenna with Improved Phase Performance, "*IEEE Transactions on Antennas and Propagation*, vol. 69, no. 12, pp. 8961-8966, 2021.

[139]   J. A. Encinar, and J. A. Zornoza. "Broadband design of three-layer printed reflectarrays." *IEEE Transactions on Antennas and Propagation*, vol. 51, no. 7, pp. 1662-1664, 2003.

[140]   R. F. E'qab, and D. A. McNamara, "Angle of Incidence Effects in Reflectarray Antenna Design: Making gain increases possible by including incidence angle effects." *IEEE Antennas and Propagation Magazine*, vol. 58, no. 5 pp. 52-64, 2016.

[141]   Mailloux, Robert J. Phased Array Antenna Handbook. Artech House, UK. 2018.

[142]   Skolnik, Merrill I. Introduction to Radar. Radar handbook, Ed. 2, Mc Graw-Hill, New York, 1962, pp. 21.

[143]   Lo, Yuen T. Antenna handbook: Antenna Fundamentals and Aathematical Techniques. Springer Science & Business Media, USA,1993.

[144]   M. H. Dahri, M. H. Jamaluddin, F. C. Seman, M. I. Abbasi, N. F. Sallehuddin, A. Y. I. Ashyap, and M. R. Kamarudin, "Aspects of Efficiency Enhancement in Reflectarrays with Analytical Investigation and Accurate Measurement." *Electronics*, vol. 9, no. 11, pp. 1887. 2020.

[145]   A. Yu, F. Yang, A. Z. Elsherbeni, J. Huang, & Y. Rahmat-Samii, "Aperture efficiency analysis of reflectarray antennas." *Microwave and Optical Technology Letters*, vol. 52, no. 2, pp. 364-372, 2010.

[146]   J. Silvestro. "Hybrid Finite Element Boundary Integral Method". White paper,   ANSYS,   INC.   Available: https://support.ansys.com/staticassets/ANSYS/staticassets/resourcelibrary/white paper/wp-HFSS-Hybrid-Finite-Element-Integral-Equation-Method.pdf

[147]   P. Galvin, "Investigation of Magnitude and Phase Errors in Waveguide Samples for the Nicolson-Ross-Weir Permittivity Technique," Master Thesis, University of New Hampshire, Durham USA. 2016.

[148]   J. Baker-Jarvis, E. J. Vanzura, and W. A. Kissick. "Improved technique for determining complex permittivity with the transmission/reflection method." *IEEE Trans. Microw. Theory Tech.,* vol. 38, no. 8, pp. 1096-1103, 1990.

[149] N. Naseer, D. Gokcen, and B. Saka, "Analysis and Design of Stopband FSS Unit Cell on Textile Substrates." *IEEE Letters on Electromagnetic Compatibility Practice and Applications*, vol. 3, no.1 15-18, 2020.